

# **Numerical prediction of Flow-Induced Vibrations in Nuclear Reactors**

A thesis submitted to the University of Manchester for the degree of  
Doctor of Philosophy  
in the Faculty of Science and Engineering

2022

Justyna Salachna  
Department of Mechanical, Aerospace and Civil Engineering

# Contents

<b>Contents</b>	<b>2</b>
<b>List of figures</b>	<b>6</b>
<b>List of tables</b>	<b>10</b>
<b>Abstract</b>	<b>11</b>
<b>Declaration of originality</b>	<b>12</b>
<b>Copyright statement</b>	<b>13</b>
<b>Acknowledgements</b>	<b>14</b>
<b>1 Introduction</b>	<b>18</b>
1.1 Background . . . . .	18
1.2 PWR main components . . . . .	19
1.3 Flow-induced vibrations in the Nuclear Reactors . . . . .	20
1.4 Examples nuclear components failures due to FIV . . . . .	24
1.4.1 FIV failures in the Steam Generator . . . . .	25
1.4.2 Fretting-wear damage in the nuclear fuel rod . . . . .	28
1.5 Conclusions . . . . .	31
1.6 Aims of the current study . . . . .	32
1.7 Outline of thesis . . . . .	32
<b>2 Literature review</b>	<b>34</b>
2.1 Analytical models . . . . .	34
2.1.1 Summary . . . . .	38
2.2 Experiments . . . . .	38
2.2.1 Effect of the free-end shape of a cantilever . . . . .	39
2.2.2 Effect of far-field disturbances . . . . .	41
2.2.3 PIV measurements . . . . .	42
2.2.4 Summary . . . . .	44
2.3 Fluid Structure interaction simulations . . . . .	45
2.3.1 Summary . . . . .	47
2.4 Conclusions . . . . .	47
<b>3 Governing equations of solid elastic displacement</b>	<b>50</b>
3.1 The Navier-Displacement Equations . . . . .	50

3.2	Mathematical Model of Solid Deformation . . . . .	50
3.3	The Linear-Elastic Constitutive Relations . . . . .	53
3.3.1	Strain-displacement relations . . . . .	53
3.3.2	Stress-strain relation . . . . .	54
3.4	The Navier-Displacement Equations . . . . .	55
3.5	Large strains . . . . .	55
3.6	Constitutive Relations: Hyperelastic materials . . . . .	57
3.7	Summary . . . . .	59
<b>4</b>	<b>Turbulence modelling</b>	<b>60</b>
4.1	Fundamental Concepts . . . . .	60
4.1.1	Eddy scales . . . . .	60
4.2	Navier-Stokes Equations . . . . .	62
4.2.1	Continuity Equation . . . . .	62
4.2.2	Momentum . . . . .	63
4.3	RANS Modelling . . . . .	63
4.4	Eddy Viscosity Models . . . . .	65
4.5	The $k$ - $\varepsilon$ Two-Equation Model . . . . .	66
4.6	The $k$ - $\omega$ Two-Equation Model . . . . .	67
4.6.1	Menter $k$ - $\omega$ SST model . . . . .	68
4.7	Reynolds Stress Models . . . . .	69
4.8	Reynolds stress models vs. eddy viscosity models . . . . .	72
4.9	Law of the wall . . . . .	73
4.10	Summary . . . . .	76
<b>5</b>	<b>Fluid Structure Interaction</b>	<b>77</b>
5.1	Coupling schemes . . . . .	77
5.1.1	One-way coupling . . . . .	78
5.1.2	Two-way coupling . . . . .	78
5.2	Gauss-Seidel scheme . . . . .	79
5.3	Under-relaxation . . . . .	80
5.4	ALE formulation . . . . .	81
5.5	Mesh Deformation . . . . .	82
5.6	Interpolation at the fluid-structure interface . . . . .	85
5.7	Summary . . . . .	86
<b>6</b>	<b>Discretization of the fluid equations</b>	<b>88</b>
6.1	Finite Volume method . . . . .	88
6.2	Diffusion terms . . . . .	89
6.3	Convection schemes . . . . .	91
6.3.1	Central differencing . . . . .	91
6.3.2	Upwind scheme . . . . .	92
6.3.3	Second order upwind scheme . . . . .	92

6.3.4	QUICK scheme . . . . .	93
6.3.5	TVD schemes . . . . .	93
6.4	Temporal discretization . . . . .	94
6.4.1	First Order Implicit Euler Scheme . . . . .	94
6.4.2	Second Order Implicit Euler Scheme . . . . .	95
6.5	Pressure velocity coupling . . . . .	95
6.6	Rhie-Chow Interpolation . . . . .	97
6.7	Boundary conditions . . . . .	98
6.7.1	Inlet . . . . .	98
6.7.2	Outlet . . . . .	99
6.7.3	Wall . . . . .	99
6.8	Solution algorithm . . . . .	101
6.8.1	Conjugate Gradient method . . . . .	102
6.8.2	Preconditioning and asymmetry . . . . .	103
6.8.3	The Multigrid approach . . . . .	104
6.9	Under-relaxation . . . . .	105
6.10	Summary . . . . .	105
<b>7</b>	<b>Discretization of the solid equations</b>	<b>106</b>
7.1	Finite Volume discretization . . . . .	106
7.2	Vertex interpolation . . . . .	108
7.3	Temporal discretisation . . . . .	109
7.4	Boundary conditions . . . . .	109
7.5	Solution procedure . . . . .	110
7.6	Summary . . . . .	111
<b>8</b>	<b>Simulation results</b>	<b>112</b>
8.1	Methodology . . . . .	112
8.2	Laminar FSI Analysis: Validation of the FSI methodology . . . . .	113
8.2.1	Conclusions . . . . .	116
8.3	Rigid body: Analysis of the turbulence models . . . . .	117
8.3.1	Conclusions . . . . .	125
8.4	Two-way FSI Simulations of Cantilever Cylinder . . . . .	125
8.5	Solid Mechanics Part - cantilever beam in vacuum . . . . .	126
8.5.1	Conclusions . . . . .	128
8.6	Two-way FSI simulations . . . . .	129
8.6.1	Simulation with the rigid rod . . . . .	129
8.6.2	Simulation with the moving rod . . . . .	130
8.6.3	Conclusions . . . . .	135
<b>9</b>	<b>Conclusions and further work</b>	<b>137</b>
9.1	Recommendations for further research work . . . . .	138
	<b>References</b>	<b>140</b>



<b>Appendices</b>	<b>152</b>
<b>A Discretization of the Upwind Scheme</b>	<b>152</b>
<b>B Discretization of the SOU Scheme</b>	<b>153</b>
<b>C Discretization of the QUICK Scheme</b>	<b>154</b>
<b>D Probability Density Function</b>	<b>155</b>
<b>E List of Publications</b>	<b>156</b>

# List of figures

1.1	Pictorial explanation of the Power Generation in the Pressurized Water Re-actor [112] . . . . .	18
1.2	Scheme of principal components of a nuclear reactor inside the radiation shield and containment. [79] . . . . .	19
1.3	Principal coolant system components of the PWR [79] . . . . .	20
1.4	PWR Fuel Assembly and the Spacer Grid set [53] . . . . .	20
1.5	A group pf circular cylinders subjected to cross-flow [22] . . . . .	21
1.6	Example of the axial flow conditions in the Fuel Assembly [25] . . . . .	21
1.7	Example of Vibration mechanisms in the design of feed water heater [73] .	22
1.8	Examples of FIV mechanisms [73] . . . . .	22
1.9	Turbulence excitation for the first two mode shapes of a simply supported flexible cylinder in axial turbulent flow [90] . . . . .	23
1.10	Fluid dynamic coupling effects for a widely spaced cluster of four parallel tubes in quiescent fluid[90] . . . . .	24
1.11	Characteristic heat exchanger damage cases due to fluid-elastic instability .	26
1.12	Typical Steam generator tube and Flow Conditions [110] . . . . .	26
1.13	Anti-vibration bar supports in the SG U-bend region and one of the low frequency modes of vibration [89] . . . . .	27
1.14	Fluid-elastic instability mechanism of a SG tube [89] . . . . .	27
1.15	Simplified contact mechanism causing GTRF [8] . . . . .	28
1.16	GTRF induced failed fuel rod locations in the core and in the FA [75] . . . .	29
1.17	Example of fretting wear in fuel rod EDF PWR 1300 [63] . . . . .	29
1.18	Example of the GTRF due to the cross-flow impingement [89] . . . . .	30
1.19	Fretting damage on Gentilly-1 Fuel Bundle [89] . . . . .	30
2.1	Mode shapes and natural frequencies for the first three modes for a can-tilever beam [90] . . . . .	36
2.2	Rod with external axial Flow [90] . . . . .	36
2.3	Example of a beam in flowing fluid showing applied forces and moments [115] . . . . .	37
2.4	Schematic view of the experimental apparatus in 1966 (a) and in 2002 (b) .	39
2.5	The effect of the shape of tapered end on the stability of cantilevered cylin-ders in 1966 (a) and in 2002 (b) . . . . .	40
2.6	Schematic view of the experimental apparatus in 2012 [117] . . . . .	40
2.7	Flow visualisation of two end pieces at the low flow velocity ( $u = 35.4$ ) [26]	41

2.8	Rods flow-induced vibration, arrows indicate that data points that were further analysed with the PIV. [26] . . . . .	41
2.9	Influence of pumps on the amplitude of vibration . . . . .	42
2.10	Instantaneous vorticity and velocity field over the blunt cylinder, $Re = 10^5$ [58] . . . . .	43
2.11	Results of the PIV measurements and simultaneous pressure measurements [15] . . . . .	43
3.1	Element subject to stress and body forces [133] . . . . .	51
3.2	Total deformation of an element. [133] . . . . .	53
3.3	One-dimensional rod loaded at the right end in initial configuration (bottom) and deformed (current) configuration (top) [6] . . . . .	56
3.4	The stress-strain relationship for elastic (1) and hyperelastic material (2,3) [91] . . . . .	57
4.1	Side view of a turbulent boundary layer visualized by smoke traces [135] . .	61
4.2	The <i>energy spectrum</i> of a turbulence behind a grid [135] . . . . .	61
4.3	Example of a flow pattern when the flow approaches an obstacle [31] . . . .	73
4.4	Non-dimensional velocity profile for an incompressible turbulent flow over a flat plate [59]. In Figure: Eq. 6.8(2): $u^+ = y^+$ , Eq. 6.8(1): $u^+ = \frac{1}{\kappa} \ln(Ey^+)$	75
5.1	Transfer of coupling data in OpenFOAM [129] . . . . .	77
5.2	Solution algorithm for one way coupling [7] . . . . .	78
5.3	Strong, two-way coupling algorithm [7] . . . . .	80
5.4	Examples of moving grid approaches [124] . . . . .	82
5.5	Mesh velocity field $w$ [85] . . . . .	83
5.6	Velocity field vs. 1D mesh distortion $x$ [85] . . . . .	84
5.7	Examples of deformed mesh fields with Laplace mesh motion equation [68]	85
5.8	Interpolation for the vertex field in two-dimensional FV mesh [130] . . . .	86
6.1	One dimensional grid used for discretization [135] . . . . .	89
6.2	A schematic showing the $EE$ and $WW$ nodes locations used for describing the SOU scheme profile [48] . . . . .	92
6.3	Grid resolution with different approaches to near-wall turbulence modelling [62] . . . . .	100
6.4	Different error modes in one-dimensional grid [87] . . . . .	104
7.1	Two dimensional, Cartesian control volume [42] . . . . .	107
7.2	Vertex $V$ surrounded by cell centres $P_i$ [19] . . . . .	108
7.3	Cartesian CV next to a boundary [43] . . . . .	110
8.1	Computational domain of the FSI laminar flow test. All dimensions are in meters [131]. . . . .	114
8.2	Example of the 'fine2' fluid mesh (grey) and solid mesh (green) used for the validation study . . . . .	115

8.3	Displacement history of a control point A . . . . .	116
8.4	Lift and drag force on the cylinder+flag . . . . .	117
8.5	Schematic diagram of a 2D forward-facing step Orange arrows indicate the separation point downstream the step (at $x/h \sim 2.1$ ) and upstream the step (at $y/h \sim 0.5$ ) . . . . .	118
8.6	Mesh grid used for the validation of turbulence models. Red arrows indicate the location of the pressure probes for the wall pressure measurements. . . . .	118
8.7	Pressure fluctuations sampled at $x=1.95h$ , $k - \omega$ model. Top: first order Upwind and the second order upwind. Bottom: QUICK scheme . . . . .	119
8.8	Pressure fluctuations sampled at $x=1.95h$ , Top: RSM- LRR and $k - \omega$ model. Bottom: $k - \omega$ SST and $k - \varepsilon$ . . . . .	120
8.9	Evolution of the $C_{p_{rms}}$ in terms of non-dimensional distance from the step . . . . .	120
8.10	Flow patterns for different URANS models at time $t = 9.9s$ . The black arrow indicates the reattachment length $x_L$ from the simulation. The grey arrow indicates the reattachment length from the experiment $x_{Lexp} = 2.1h$ . . . . .	121
8.11	PSD for the LRR Reynolds Stress Model, $k - \omega$ and $k - \omega$ SST at $x=1.95h$ compared to experimental results. The red line indicates the limit for high energy pressure oscillations (15Hz). Arrows indicate dominating frequency peaks . . . . .	122
8.12	PSD for the LRR Reynolds Stress Model, $k - \omega$ and $k - \omega$ SST at $x=0.45h$ compared to experimental results. An indication is the same as in the Figure 8.11 . . . . .	122
8.13	PSD for the LRR Reynolds Stress Model, $k - \omega$ and $k - \omega$ SST at $x=2.7h$ compared to experimental results. An indication is the same as in the Figure 8.11 . . . . .	123
8.14	PSD for the LRR Reynolds Stress Model, $k - \omega$ and $k - \omega$ SST at $x=6.45h$ compared to experimental results. An indication is the same as in the Figure 8.11 . . . . .	123
8.15	PDF of the normalised wall pressure fluctuations, LRR scheme. Different colours correspond to different locations of the step. Circles are the results of simulation and crosses from the experiment. Locations upstream of the step are grouped on the left sub-figure, and locations downstream of the step are grouped on the right sub-figure. The solid line is the Gaussian reference curve. . . . .	124
8.16	PDF of the normalised wall pressure fluctuations, $k - \omega$ scheme. Indications are the same as in the Figure 8.15. . . . .	124
8.17	Schematic representation of the test rig [26] . . . . .	126
8.18	Geometry of the domain for a flexible beam in vacuum simulation . . . . .	127
8.19	Free-end displacement time series for a simulation of a cantilever in vacuum . . . . .	128
8.20	Computational domain for a cantilever in turbulent flow simulation . . . . .	130
8.21	Flow fields around the rod tip at low flow velocity, results from the $u^*=36$ and the experimental results $u^*=35.7$ . . . . .	131

8.22	Velocity profiles for velocity $u^*=36$ , vertical elevation locations are provided in the legend . . . . .	132
8.23	Displacement of a free-end vibrating beam in the x direction vs. experimental data . . . . .	133
8.24	Normalized histogram of a number of occurrences observed for a free-end displacement on x-plane. Simulation vs experiment . . . . .	134
8.25	Displacement of a free-end vibrating beam in the y direction vs. experimental data . . . . .	134
8.26	Normalized histogram of the number of occurrences observed for a free-end displacement on y-plane simulation vs experiment . . . . .	135
8.27	Displacement of a free-end vibrating beam vs. experimental data . . . . .	136
D.1	PDF of the normalized wall pressure fluctuations, $k - \omega$ SST scheme. Indications are the same as in the Figure 8.15. . . . .	155
D.2	PDF of the normalized wall pressure fluctuations, $k - \varepsilon$ scheme. Indications are the same as in the Figure 8.15. . . . .	155

# List of tables

2.1	influence of the beam end-shape and direction of the flow on the cantilever beam . . . . .	44
2.2	Experimental studies of FIV from axial turbulent flow . . . . .	45
4.1	Standard RANS turbulence models [135] . . . . .	65
8.1	Fluid and solid properties in the FSI laminar simulation . . . . .	114
8.2	x- and y-displacement of the control point A versus the FSI benchmark. Data are denoted as: mean $\bar{d}$ , amplitude A and frequency $f_N$ . . . . .	116
8.3	Lift and drag force on the cylinder and flag versus the FSI benchmark. Data are denoted as: mean lift force $\bar{F}_L$ , mean drag force $\bar{F}_D$ amplitude A and frequency $f_N$ . . . . .	116
8.4	Solid properties used in the flexible beam in vacuum simulation . . . . .	127
8.5	Effect of the time step on the calculated natural frequency . . . . .	128
8.6	Fluid properties and simulation parameters . . . . .	129
8.7	Frequency and Amplitude of flow-induced vibration x-plane, LRR scheme .	133
8.8	Frequency and Amplitude of flow-induced vibration y-plane, LRR scheme .	135
8.9	Frequency and Amplitude of flow-induced vibration, $k - \omega$ scheme . . . . .	135

# Abstract

This study was set out to perform a fluid-structure interaction benchmark simulation of the cylindrical cantilever beam subjected to the axial turbulent flow. The application has practical importance in the fuel rods in Pressurized Water Reactors (PWR). The modelling approach was chosen to be optimal for industrial applications.

A recent experimental study from the authors' group on flow-induced vibrations generated by axial turbulent flow over a cantilever rod provides data on the rod displacement and local flow data, making this case highly attractive for CFD validation. The motivation for this research is thus provided by the availability of these data from reference [26].

This thesis investigates the computational modelling of flow-induced vibrations of cantilever rods subjected to turbulent axial flow at operating conditions relevant to those of fuel rods of PWR nuclear reactors. The aim is to assemble all the modelling elements needed for a cost-effective and thus URANS-based (Unsteady Reynolds Averaged Navier Stokes) modelling strategy, employing high-Reynolds-number turbulence models. This objective is pursued through three stages. It was first necessary to investigate the numerical FSI (Fluid-Structure Interaction) strategy adopted through the computation of flow-induced vibration of an elastic plate subjected to axial laminar flow. Then the suitability of URANS models was assessed through computations of turbulent flow over a forward-facing step, for which measurements of the fluctuating wall pressure are available. On the numerical side, these explorations led to adopting a two-way FSI strategy, using a single finite-volume solver, with the Arbitrary Lagrangian-Eulerian (ALE) approach, high-order convective discretization schemes and Laplacian smoothing for the displacement of the mesh in the fluid domain. On the physical modelling side, they resulted in the use of high-Reynolds-number Reynolds stress transport models.

The resulting modelling strategy is subsequently validated against the experimentally investigated case of a steel cantilever rod caused to vibrate through exposure to turbulent axial flow. This is the first study that has successfully reproduced both the frequency and the amplitude of the flow-induced vibrations relevant to PWR applications, based on the use of URANS.

# **Declaration of originality**

I hereby confirm that no portion of the work referred to in the thesis has been submitted in support of an application for another degree or qualification of this or any other university or other institute of learning.



# Copyright statement

- i The author of this thesis (including any appendices and/or schedules to this thesis) owns certain copyright or related rights in it (the “Copyright”) and s/he has given The University of Manchester certain rights to use such Copyright, including for administrative purposes.
- ii Copies of this thesis, either in full or in extracts and whether in hard or electronic copy, may be made *only* in accordance with the Copyright, Designs and Patents Act 1988 (as amended) and regulations issued under it or, where appropriate, in accordance with licensing agreements which the University has from time to time. This page must form part of any such copies made.
- iii The ownership of certain Copyright, patents, designs, trademarks and other intellectual property (the “Intellectual Property”) and any reproductions of copyright works in the thesis, for example graphs and tables (“Reproductions”), which may be described in this thesis, may not be owned by the author and may be owned by third parties. Such Intellectual Property and Reproductions cannot and must not be made available for use without the prior written permission of the owner(s) of the relevant Intellectual Property and/or Reproductions.
- iv Further information on the conditions under which disclosure, publication and commercialisation of this thesis, the Copyright and any Intellectual Property and/or Reproductions described in it may take place is available in the University IP Policy (see <http://documents.manchester.ac.uk/DocuInfo.aspx?DocID=24420>), in any relevant Thesis restriction declarations deposited in the University Library, The University Library’s regulations (see <http://www.library.manchester.ac.uk/about/regulations/>) and in The University’s policy on Presentation of Theses.

# Acknowledgements

Firstly, I wish to thank my supervisors, Dr Andrea Cioncolini and Prof. Hector Iacovides, for their constant advice, support and patience. I am incredibly grateful for their critical reviews and constructive feedback throughout this PhD study. I want to extend my thanks to Prof. Alistair Revell for his research assessment and advice during the PhD progress reviews.

Secondly, I would like to express my gratitude to EDF Energy and the MACE Beacon Scholarship at the University of Manchester for providing financial support for this study. I also owe a great deal to my friends and fellow colleagues in the Department of Mechanical, Aerospace and Civil Engineering, who provided practical suggestions and were a source of optimism throughout.

Finally, my acknowledgements would not be complete without thanking my family, my husband Mateusz, my brother Piotr and my parents, Krystyna and Kazimierz, for their tremendous understanding and encouragement in the past few years.

# Nomenclature

## Symbols

$\epsilon_{ij}$	strain tensor
$\gamma$	diffusion coefficient
$\lambda$	Lamé's constant, $Pa$
$\mu$	shear modulus, $Pa$
$\mu_F$	fluid dynamic viscosity, $kg/ms$
$\mu_t$	turbulent eddy viscosity $kg/ms$
$\omega$	specific turbulence dissipation rate, $1/s$
$\overline{u_i u_j}$	turbulent shear stress tensor
$\rho_F$	fluid density, $kg/m^3$
$\rho_S$	solid density, $kg/m^3$
$\sigma_{ij}$	stress tensor
$\varepsilon$	dissipation rate of the turbulent kinetic energy, $m^2/s^3$
$A^*$	root-mean square amplitude
$A_{RMS}$	root-mean square vibration amplitude
$c_N$	natural frequency parameter
$C_{prms}$	root mean square pressure coefficient
$E$	Young's modulus, $Pa$
$F, T$	Fluid force, $N$
$F_A$	Fluid added acceleration force, $N$
$F_D$	Drag force, $N$
$F_L$	Lift force, $N$
$f_N$	natural frequency $Hz$
$F_S, T_S$	Solid force, $N$
$F_y^d$	Fluid damping force, $N$

$F_y^e$	Fluid exciting force, $N$
$I$	second moment of area of the beam's cross-section, $mm^4$
$k$	turbulent kinetic energy, $m^2/s^2$
$m_{add}$	added mass per unit length $g/m$
$m_{rod}$	mass of the beam per unit length $g/m$
$P, p$	fluid pressure, $Pa$
$Re$	Reynolds number
$St$	Strouhal number
$U, u_F$	fluid velocity, $m/s$
$u, x_S$	solid displacement
$u^+$	non-dimensional velocity
$w$	interface grid velocity $m/s$
$y^+$	dimensionless distance normal to the surface

### **Acronyms**

<i>AEF</i>	Advanced European Fuel
<i>ALE</i>	Arbitrary Lagrangian-Eulerian
<i>BWR</i>	Boiling water Reactor
<i>CANDU</i>	Canada Deuterium Uranium reactor
<i>CFD</i>	Computational Fluid Dynamics
<i>CSM</i>	Computational Structural Mechanics
<i>DES</i>	Detached eddy simulation
<i>ECT</i>	Equivalent Computational Time
<i>EDF</i>	Électricité de France
<i>EFG</i>	European Fuel Group
<i>EIE</i>	Extraneously-Induced Excitation
<i>EVM</i>	Eddy-Viscosity Models
<i>FA</i>	Fuel Assembly
<i>FE</i>	Finite Element Method
<i>FIV</i>	Flow-Induced Vibration
<i>FSI</i>	Fluid-Structure Interaction

*FV* Finite Volume Method  
*GTRF* Grid-to-rod fretting  
*IIE* Instability-Induced Excitation  
*LES* Large eddy simulation  
*LRR* Launder, Reece and Rodi model  
*LWR* Light-water Reactor  
*MACE* Department of Mechanical, Aerospace and Civil Engineering  
*MIE* Movement-Induced Excitation  
*PDF* Probability Density Functions  
*PHWR* Pressurized heavy-water reactor  
*PISO* Pressure-Implicit with Splitting of Operators algorithm  
*PIV* Particle image velocimetry  
*PSD* Power Spectral Density  
*PWR* Pressurized Water Reactor  
*RANS* Reynolds Averaged Navier-Stokes  
*RMS* Root-mean-square  
*SG* Steam Generator  
*SIMPLE* Semi-Implicit Method for Pressure Linked Equations algorithm  
*SOUE* Second Order Euler Scheme  
*SSG* Speziale, Sarkar and Gatski model  
*URANS* Unsteady Reynolds-averaged Navier-Stokes  
*WWER* Water-water energetic reactor

# Chapter 1

## Introduction

This section presents the background information about the Pressurized Water Reactor, the nuclear power generation process and the major nuclear components. The Chapter introduces the flow conditions in the reactor and explains the flow-induced vibration phenomena (FIV). Then, examples of the fluid-elastic instability and fretting wear damages caused by FIV in the nuclear industry are presented. Finally, the conclusions from this initial investigation helped to understand the importance of the topic and led to deriving the objectives of this PhD project.

### 1.1 Background

The Pressurized-Water Reactor (PWR) is a type of thermal reactor which is moderated, partially-reflected and cooled by light water. The power generation process is presented in Figure 1.1. The Nuclear Power Plant of the PWR type consists of the primary circuit and the secondary circuit. In the primary nuclear loop, water is heated via nuclear reaction in the reactor vessel, and then high-pressure steam is generated in the Steam Generator (SG). A Steam Generator serves a function of a heat exchanger between the primary and a secondary circuit. Because of that, the secondary side of the plant is not contaminated by radiation from the primary side.

Nuclear reactors are designed using the concept of multiple barriers, and it is loosely depicted in Figure 1.2. Each barrier is a physical obstacle to block the passage of radioactive release from the fuel. Nuclear fuel and its cladding tubes are classified as the first physical barrier against radioactive release. Then the Reactor vessel is the second physical barrier. Finally, the reactor building (containment) is the last physical barrier against the release.

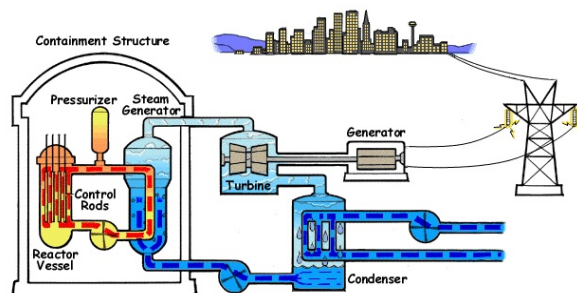


Figure 1.1. Pictorial explanation of the Power Generation in the Pressurized Water Reactor [112]

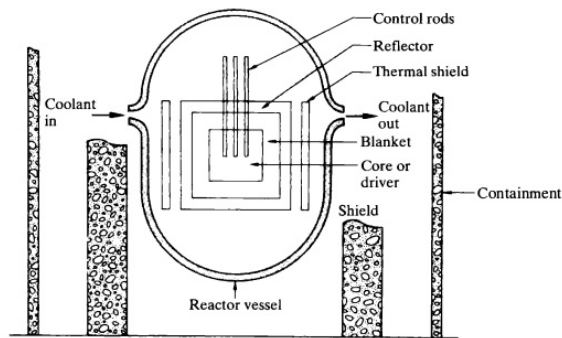


Figure 1.2. Scheme of principal components of a nuclear reactor inside the radiation shield and containment. [79]

## 1.2 PWR main components

Figure 1.3a shows a cross-sectional view of the PWR reactor vessel. The core is located in the central region inside the reactor vessel. In the PWR reactor, the core contains nuclear fuel and water, which is coolant and also acts as a moderator. Water coolant enters the Reactor Vessel via an inlet nozzle at a temperature of about  $290^{\circ}\text{C}$ , flows down around the outside of the core, then passes upwards through the core where it is heated, and finally exits from the vessel with a temperature of about  $325^{\circ}\text{C}$ . Water in the primary circuit of a PWR is maintained at high pressure (around  $15\text{MPa}$ ) in order to prevent from boiling flows mainly under single-phase. Two-phase flow conditions can occur only during the accidental conditions [29]. Steam for plant turbines is produced in the steam generators with the pressurized, heated water from the outlet nozzle. The process is depicted in Figure 1.3b. Coolant water from the reactor enters at the bottom of the SG and passes upward and then downward through several thousands of U shape tubes. At the same time, colder and lower pressure feed water from the turbine condenser enters the SG through the Feed water inlet. Hot outer surfaces of the SG tubes are in contact with the feed water, causing it to boil and produce steam. The steam is dried in the set of moisture separators and exited on the turbines.

In a western type PWR nuclear fuel rods are called Fuel assembly (FA), as depicted in Figure 1.4 (left). Fuel rods consist of fuel pellets assembled in metal tubes made of zirconium alloy. Rod bundles are placed between the top and bottom nozzles with several spacing grids in between to assure exact guiding of the fuel rods. Spacer grids are to support the fuel rod - Figure 1.4 (right). Springs and dimples are attached to the unit spacer grid in order to prevent structural instability [123]. The second function of the spacer grid is to enhance the coolant mixing, which improves heat transfer between the fuel rods' surface cladding and the coolant. Mixing vanes are designed to induce a strong swirl in the cooling flow around the fuel pellet, enhancing the coolant flow turbulence [41]. The fuel assembly is loaded once per approximately 3-4 years, depending on the operating cycle. The fuel rod component is the first and most important physical barrier against the release of radioactive material from the plant.

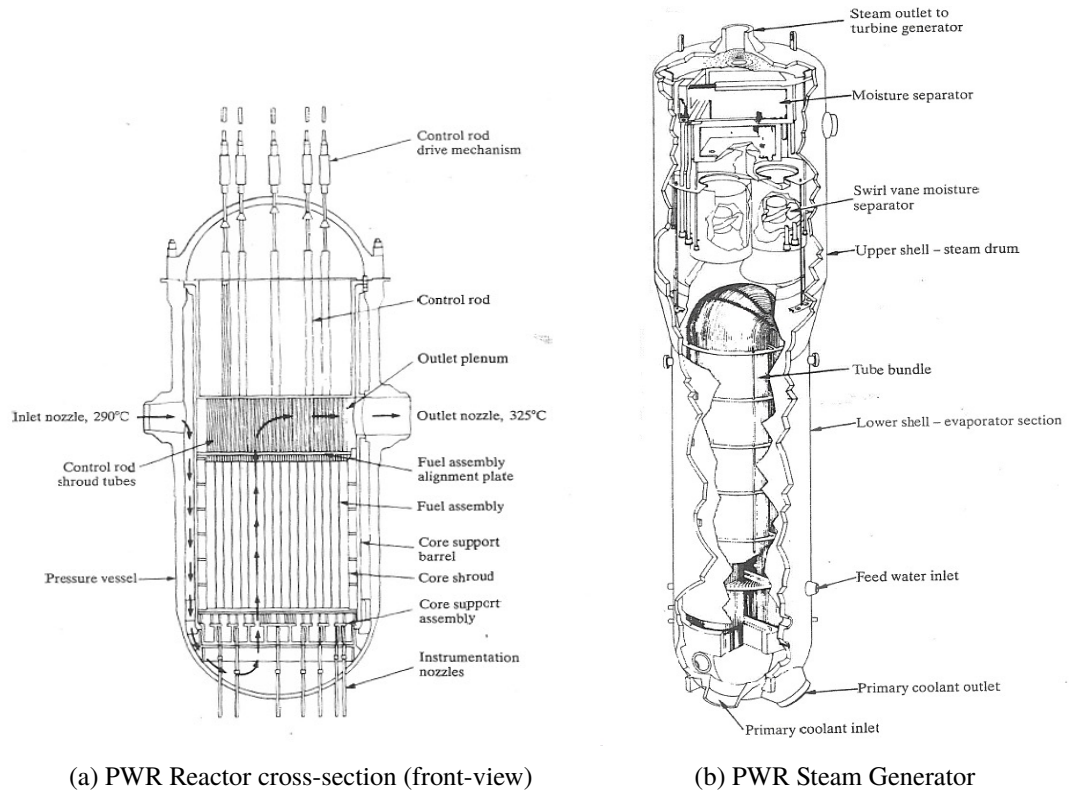


Figure 1.3. Principal coolant system components of the PWR [79]

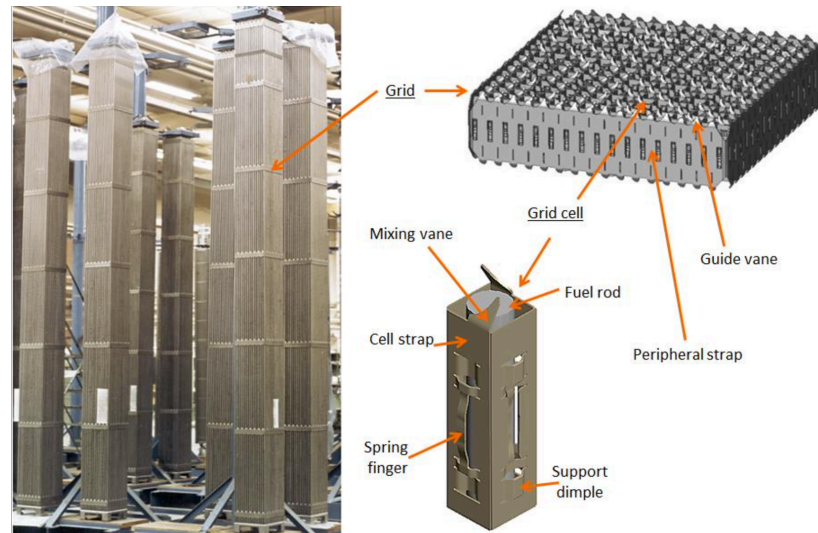


Figure 1.4. PWR Fuel Assembly and the Spacer Grid set [53]

### 1.3 Flow-induced vibrations in the Nuclear Reactors

The dynamic forces produced by highly turbulent coolant flow can cause excessive mechanical vibration of the PWR components. This flow-related vibration phenomenon is generally known as *flow-induced vibration* (FIV). In nuclear reactors, flow-induced vibration usually occurs in the primary loop, where components are subjected to relatively high flow velocities. Typical of such components are pipes, nuclear fuel rods in the Fuel Assembly (FA), tube bundles in the Steam Generators and the in-core instrumentation [12, 110].

According to Païdoussis, axial- and cross-flow induced vibration of cylindrical structures



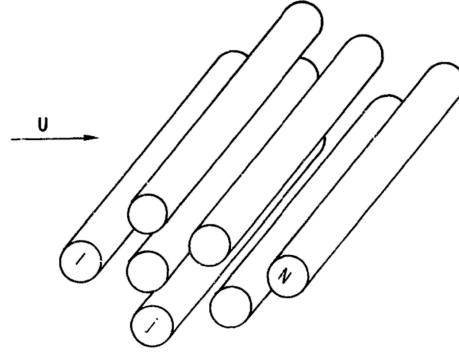


Figure 1.5. A group pf circular cylinders subjected to cross-flow [22]

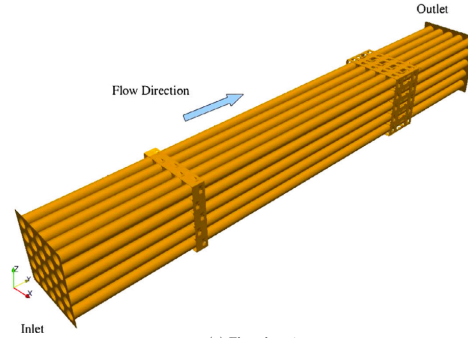
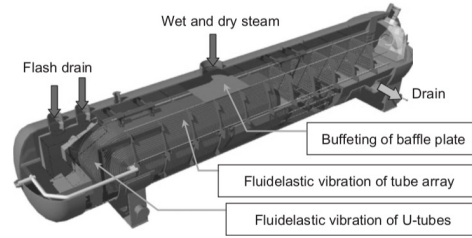


Figure 1.6. Example of the axial flow conditions in the Fuel Assembly [25]

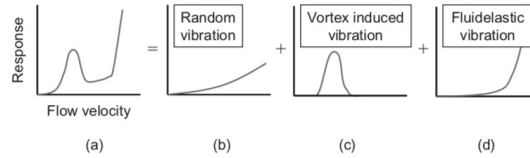
are two major vibration problems occurring in nuclear reactors [98]. Axial flow-induced vibrations usually result in the dynamic interaction between a component and its supports, generating long-term damage such as fretting wear and high-cycle fatigue. In contrast, cross-flow induced vibrations led to more serious problems such as fluid-elastic instability, buffeting and vortex-induced vibrations of cylinder arrays [99, 110]. Cross-flow condition refers to flow normal to the long axis of the slender structure. It can be illustrated briefly by the sketch in Figure 1.5. In this example, even moderate flow velocities can cause a large amplitude vibration. A classic example of the external axial flow conditions is depicted in Figure 1.6, where coolant flows through the fuel assembly mainly in the axial direction. In this type of flow conditions the reduced vibration amplitude  $\frac{A_{RMS}}{D}$  varies in the range of  $10^{-2}$  to  $10^{-3}$ , where  $A_{RMS}$  is the RMS vibration amplitude and  $D$  is the cylinder diameter [100].

The limitation of this classification approach is that in practice, the nuclear flow is complex, and FIV results from a combination of vibration phenomena: flow acting on one component can have both cross- and axial components and is unsteady too. For example, Figure 1.7 shows the vibrations mechanism in the feed water heater and an analysis of the vibration response. A sharp increase in the vibration amplitude in Figure 1.7b is a result of the sum of vibration mechanisms induced by the cross-flow in the component: turbulence excitation and the vortex-induced vibration which is proportional to the flow velocity, the fluid-elastic instability, which can occur when the critical velocity is reached.

Naudascher and Rockwell [90] classified flow-induced vibrations phenomena by sources of excitation. These can be subdivided into extraneously-induced excitation (EIE), instability-induced excitation (IIE) and movement-induced excitation (MIE). Examples of models for



(a) Feed water heater design



(b) Vibration response of the feed water heater

Figure 1.7. Example of Vibration mechanisms in the design of feed water heater [73]

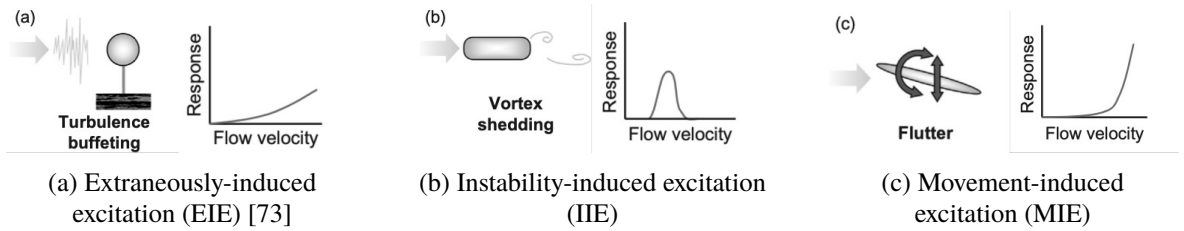


Figure 1.8. Examples of FIV mechanisms [73]

each vibration mechanism and the corresponding vibration response in relation to the flow velocity are schematically depicted in Figure 1.8. The following classification helps in identifying the root causes of vibration failures. In the case of extraneously-induced excitation (EIE) the flow unsteadiness is caused by fluctuations- random changes in the flow velocities in the flow. Fluctuations generate fluctuating external force acting on a body. This type of excitation is independent of body movement. Only the external forcing from the fluid keeps the structure vibrating. An example is a cylindrical structure being "buffeted" by the turbulence of the incoming flow as depicted in Figure 1.8a. Other important identified sources of EIE are cavitation, machines in a system i.e. pumps, waves and earthquakes. In the case of turbulence buffeting being the source of EIE, the structural load is caused by pressure fluctuations generated by turbulent eddies passing near or impinging on the structure. In this case, the structural vibration depends on two major parameters: turbulence intensity and the size of eddies containing most of the turbulent energy. According to Naudascher (following experimental research of Chen & Wambsganss [23]) large-scale eddies, which generate low-frequency velocity and pressure fluctuations, have the highest potential to excite the structure in the first mode of vibration ( $N=1$ ). The second mode of vibration ( $N=2$ ) is excited more effectively with intermediate scale eddies. Figure 1.9 shows the collective experimental data of the wall pressure spectra in an axial turbulent flow. Diagram illustrates the 'effectiveness' of pressure ( $J_N$ ) in exciting the simply supported beam. On the left-hand side, the large-scale eddies excite the first mode shape of the beam but do not affect the second mode. The peak for the second mode of vibration results from intermediate scale eddies. The smallest scale eddies have practically no effect on the structure. It is worth adding

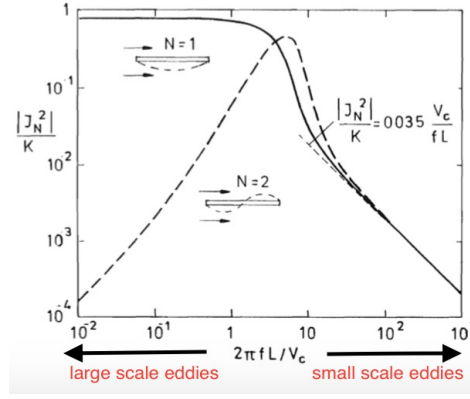


Figure 1.9. Turbulence excitation for the first two mode shapes of a simply supported flexible cylinder in axial turbulent flow [90]

that, according to Blevins [11], long-term wear of heat exchanger tubes and fuel rods is mainly caused by turbulent buffeting. Another important source of EIE is so-called far-field flow noise: flow pulsations and turbulence generated by pumps and bends cavitation transmitted through the flow. The far-field noise effect depends mainly on the system design.

Instability-induced excitation (IIE) is associated with flow instability above a certain velocity threshold value. Also, as a rule this instability type is intrinsic to the flow created by the structure. An alternating vortex shedding formation past a cylindrical structure depicted in Figure 1.8b is a classic example of IIE. The periodic shedding of the von Kármán vortices causes periodic pressure variations on the structure. Vibrations in the transverse direction to the flow have a dominant frequency called von Kármán vortex shedding frequency  $f_w$ . In literature, the shedding frequency is often scaled in dimensionless form by the Strouhal number  $St$ ,  $St = \frac{f_w D}{U}$ . Where  $U$  is the flow velocity and  $D$  is the characteristic length (diameter). The phenomenon called *lock-in*, can occur if a vortex shedding frequency is near the natural frequency of the structure. The most dramatic illustration of this was the failure of the Tacoma Narrows suspension bridge in 1940 when wind-excited vortex shedding oscillations resonated with natural torsional oscillations of the bridge [139]. Another prominent example of the IIE can be the fluid-elastic instability of the PWR steam generator tubes induced by the cross-flow, examples of which will be presented in Section 1.4.

Movement-induced excitation (MIE) mechanism is inherently related to the movement of the structure. When the model undergoes transverse movements, the accompanying flow changes will induce forces that tend to enhance these initial movements. The induced vibrations are thus self-excited. Wing flutter and galloping encountered with aircraft wings depicted in Figure 1.8c is an important example of MIE. The abrupt vibration amplitude increases at high flow velocities when the critical flow velocity is reached. In the nuclear industry, the MIE mechanism is further sub-classified into *MIE involving coupling*. The mechanism is related to coupling effects occurring in multiple bodies immersed in the fluid. A cylinder array consisting of 4 circular cylinders with the same mechanical properties is presented in Figure 1.10a. In the study, the motion of cylinder *a* excites the surrounding cylinders at the same dominant frequency. Furthermore, the response magnitude is strongly related to the distance between the tubes. For a widely spaced cluster, Figure 1.10b charac-

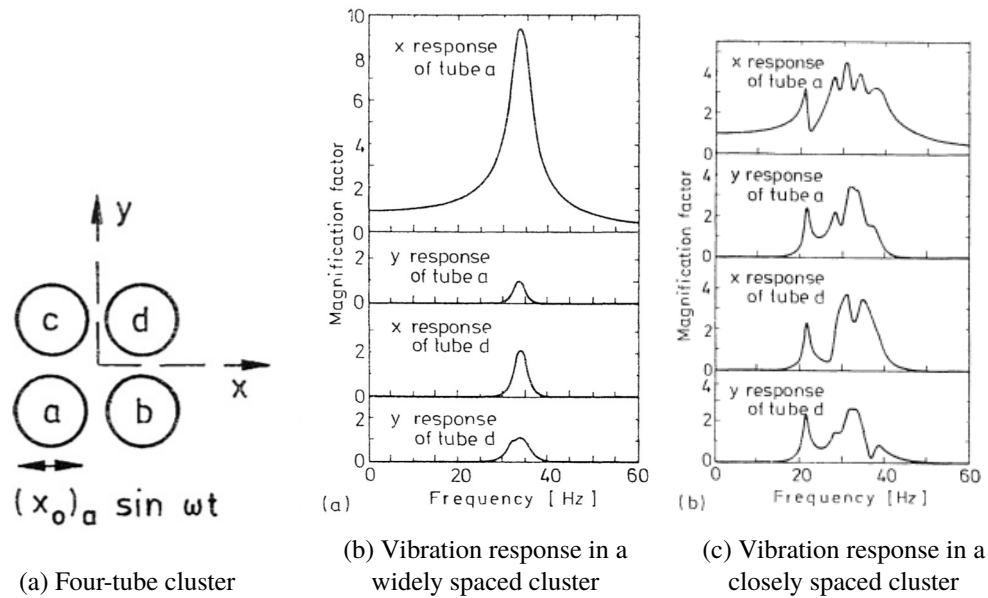


Figure 1.10. Fluid dynamic coupling effects for a widely spaced cluster of four parallel tubes in quiescent fluid[90]

teristic excitation frequency of the cylinder  $a$  is present in all surrounding cylinders. For a closely-spaced cluster in the Graph 1.10c, all tubes vibrate over a broader frequency range. The coupling effect is important in closely spaced tube arrays in the design of nuclear fuel assembly and steam generators.

Other classifications tend to be more general. In 2001, Blevins [11] performed an extensive analysis of structures exposed to fluid flow. He distinguished excitation from steady flow and unsteady flow. Steady flow-induced vibrations are subdivided into instabilities (e.g. galloping and flutter) and vortex-induced vibrations. Unsteady flow is divided into random (e.g. turbulence-induced), sinusoidal (e.g. pump pulsation) and transient (e.g. pipe whip).

## 1.4 Examples nuclear components failures due to FIV

As explained earlier, FIV problems are inevitable in nuclear plants. In the case of SG tubes and fuel rods in the fuel assembly it is desirable to minimize the structural support to reduce the pressure drop and improve heat transfer [86]. Although extensive research on natural frequencies and mode shapes of a typical fuel assembly has been carried out [22, 24, 97, 136], there were many instances wherein a component was susceptible to flow-induced vibration despite the adequate margins in the calculations.

IAEA TECTOC [64] provides technical exchanges on PWR operational experience in the field mechanical behaviour of the fuel assembly. In the case of SG-tube leakage in PWRs the radioactive contamination escapes the second physical barrier and contaminates the secondary side of the plant. Other possible consequences of the fuel rods perforation or SG tube failure are:

- Changes in the fuel loading pattern

- Anticipated plant shutdown when the fission gas in the primary coolant exceeds impermissible level
- Extended reactor outage for the failed SG tube replacement
- Appropriate operating personnel training in higher radiation levels (during extended outage and normal operation)

International Atomic Energy Agency (IAEA) [63] provided a report with an overview of fuel failures in the water cooled reactors and presents in detail their mechanisms and mitigation measures. Interest in fuel failures result from the caused inconvenience during plant operation, it is generally expected to reach a zero-failure rate. Fuel failure statistics and operation experience comes from different water-cooled reactor types, including LWR, PWR, BWR, WWER and heavy water CANDU/PHWR types. Proceedings from symposium held in Karlsruhe (1979) [89], reported fifty-two case studies related to cross-flow, internal and external axial-flow induced vibration in nuclear power plants. Collection of observations and root-causes of events for preparation of a symposium took 3 years. Each problem is described by a separate chart, flow conditions, vibration mechanism and treatment after the failure. Pettigrew [110] analysed problems of flow-induced vibrations in Canadian type reactors- CANDU. He identified possible flow conditions in nuclear components and analysed vibration excitation mechanism in axial and cross flow. Real examples of fretting wear, fatigue, acoustic noise and operational difficulties in Canadian nuclear industry were presented in 2017. Pettigrew et al.[111] discussed the fretting wear damage from flow induced vibration for sensitive nuclear components. Relation of vibration energy to work rate and fretting wear damage was formulated.

The analyzed case studies from the references above have shown that any replacement of leaky tube or component generates not only the cost of replacement of the part itself, but also a high outage cost. Hence, there is pressure for an immediate repair, without complete understanding of the mechanism of failure involved. Also, assessments of failures in nuclear plants are described insufficiently and usually are not widely accessible [10]. In accordance with these reports, French nuclear industry expresses need to deeply understand the physical mechanism that controls fluid-structure interaction for basic configurations, such as slender structure in axial confined flow [12]. Primarily, numerical simulation will have to be benchmarked by experiments especially for specific configurations and turbulence. In addition, a systematic understanding of the relation of excitation forces to vibration excreted on the fuel rods is still lacking.

The section below presents a number of incidents caused by flow-induced vibrations in the in nuclear power plants components.

#### **1.4.1 FIV failures in the Steam Generator**

Figures 1.11a 1.11b show the example of fatal SG tube failure due to fluid-elastic instability in the sodium-water heat exchanger (around 1970). In this case, the  $Na - H_2O$  reactions

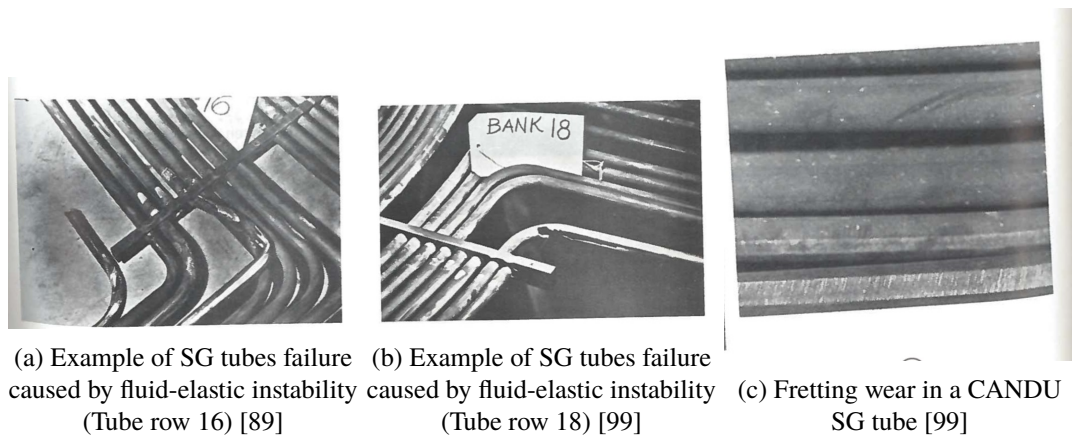


Figure 1.11. Characteristic heat exchanger damage cases due to fluid-elastic instability

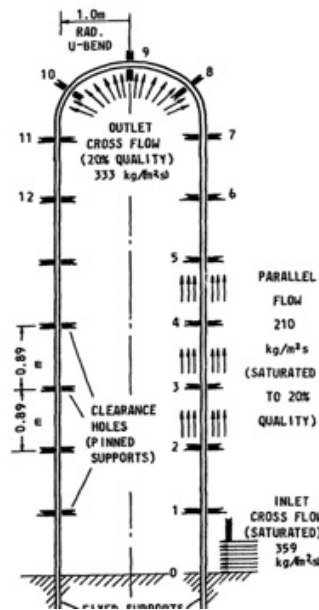


Figure 1.12. Typical Steam generator tube and Flow Conditions [110]

had an additional impact on the structure resulting in such harmful devastation [99]. Figure 1.11c presents the fretting wear damage at the top of the U-bend in the CANDU steam generator. This is a classic example of an extensive vibration response resulted from cross-flow. The vibration amplitude was high enough that tubes were touching each-other and the anti-vibration bars, with consequent fretting wear.

Typical flow conditions prevailing over SG tubes are shown in the Figure 1.12. Normally both axial and cross flow occur in the heat exchangers, however SG tube failures result from cross-flow induced vibration [99]. Moreover, the U-bend region in steam generators is subjected to the two-phase bubbly flow [47]. It is almost impossible to predict the frequency response analytically due to the time-varying air-water mixture [20]. Three mechanism of excitation in the context of heat exchangers are mentioned in the literature: vortex shedding, buffeting [98] and fluid-elastic instability [110].

Vibration-induced fretting wear is a relatively common mode of failure of steam generator U-tubes. According to statistics provided by Païdoussis [98] almost 10% of all shut-downs and power reductions, during 5 year period from 1974 in United States, were related

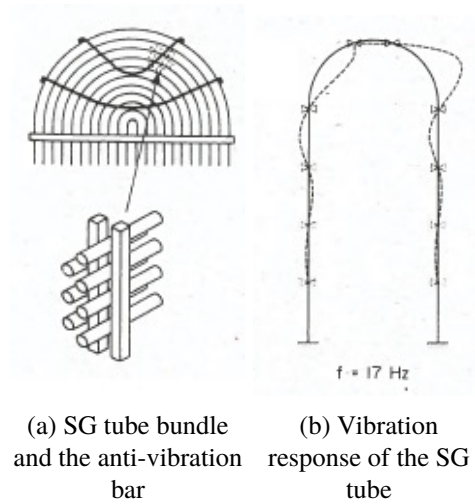


Figure 1.13. Anti-vibration bar supports in the SG U-bend region and one of the low frequency modes of vibration [89]

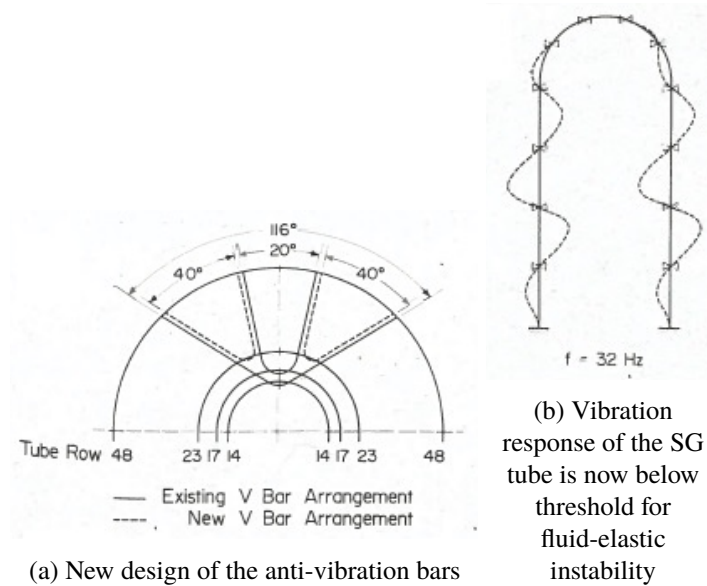


Figure 1.14. Fluid-elastic instability mechanism of a SG tube [89]

to flow-induced vibration problems. With regards to steam generator tube failures world-wide, before 1980, 10% were caused by flow-induced vibration fretting and fatigue [89]. Many incidents reported in the 1970s [89, 99] and in Douglas Point power station [110] showed that the the SG tube failures resulted from an inadequate support in the U-region as illustrated in Figures 1.13a, 1.13b. Because of the insufficient support SG tube get unstable at the low frequency mode ( $f=17\text{Hz}$ ) from a relatively low flow velocity. At that time, tubes were made from carbon steel. In order to prevent the flow induced instability and fretting, additional support bars from the wear-resistant material (Inconel-600) were introduced. Additionally, the cross-section of the support bars was changed from round to rectangular. These enhancements allowed continuous operation below the threshold for fluid-elastic instability as reported in the Figure 1.14a, 1.14b.

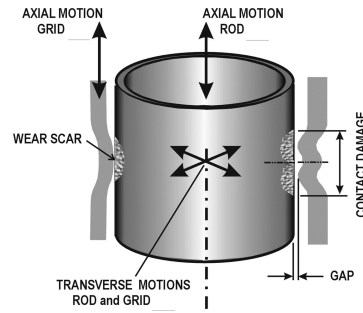


Figure 1.15. Simplified contact mechanism causing GTRF [8]

#### 1.4.2 Fretting-wear damage in the nuclear fuel rod

According to Pettigrew et al. [111] nuclear fuel rod is the most vulnerable structure for fretting wear damage, among all components of concern, because it is exposed to contact with adjacent fuel rods and the support grids at several locations. The wear of fuel rod against supporting structures is known as a *grid-to-rod fretting* (GTRF). Mechanism of grid-to-rod fretting wear-induced fuel failure is schematically shown in the Figure 1.15. The simplified geometry shows a hollow tube representing the fuel cladding and dimple/spring couple which hold the rod in place. Flow-induced oscillations cause transverse motions of the rod, which causes the continuous or intermittent contact with the dimple. Fretting wear can eventually lead to reducing the fuel cladding thickness and consequent perforation of the tube.

Several factors are known to increase the risk of GTRF. Fretting wear increases strongly with a larger FIV because of higher amplitude of tube vibration and exciting forces [10]. It is clear however, that GTRF phenomenon is very complex and depends on many variables, not only the flow-induced excitation, but also high temperatures of a coolant, corrosion process in aqueous conditions and material embrittlement from neutron irradiation [8]. Furthermore, nuclear fuel pellets are swelling during operation, due to the fission gas formation in the fuel which has an influence on the flexural rigidity of the fuel element [134]. Based on operating experiences [10, 75] GTRF fuel failures rates depends also on the design of the Fuel Assembly. It was estimated that relatively large grid-to-rod contact area, small grid-to-rod gap, and harder surfaces contribute to lower probability of GTRF fuel failures for the same excitation forces.

Finally, the important aspect for modeling purposes is to estimate where in the core, the conditions are dominant for the severe fretting wear. Examination of several fuel rods carried out by Kyu-Tae Kim [75], shows that grid-to-rod fretting wear related failures can occur at any axial location of the grid, and the first leak signals from failed rods were observed over the whole operating cycle. Additionally, the majority of the failed fuel rods were found at the periphery of the reactor core, Figure 1.16a, and the outer edges of the fuel assembly, Figure 1.16b. This result can be explained by the fact the FA's in the outer regions of the core is subjected to stronger external vibrations, caused by highly turbulent reactor coolant flow in this part. Interestingly the same FA will be resistant for the GTRF induced failures in one reactor core design, but it would be susceptible for fretting wear in different reac-



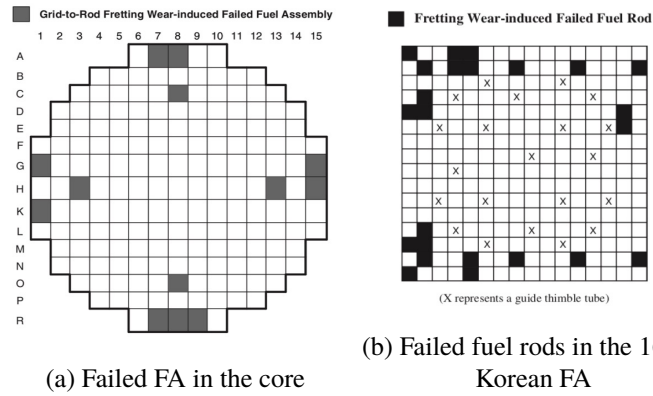


Figure 1.16. GTRF induced failed fuel rod locations in the core and in the FA [75]

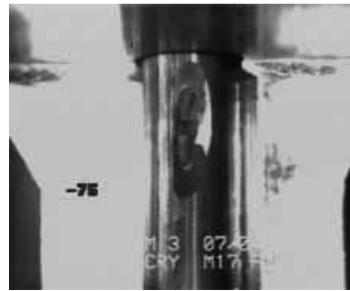


Figure 1.17. Example of fretting wear in fuel rod EDF PWR 1300 [63]

tor core designs. This example shows that external flow-induced vibrations are dominant contributors for GTRF fuel failures. The findings are supported by Korean experience presented for the public in 2005 [74].

An important example of FIV failures is presented in the Figure 1.17, where various fuel rod failures were discovered in the year 2000 at some of EDF's four loop 1300 MW(e) reactors. Most of the fuel assemblies experienced a fretting wear damage at the bottom grid, while the wear marks at the upper part of the FA's were not significant [63]. All the leaking FA's were located at an intermediate ring inside the core. It was expected however, to find damaged rods at the peripheral part of the core. After extensive investigation, it was concluded that GTRF was developed from significant cross-flows in the lower part of the fuel assemblies. Additionally to that, spring support at the bottom of the fuel assembly relaxed over extended operation time, which resulted in decreased holding force. It is worth noting that a risk of fretting wear failures was found only for 1300 MW(e) reactors. In the case of 900 MW(e) plants, lower cross-flows have never induced fretting wear failures.

Another important example of an extensive fuel rod vibration in peripheral fuel assemblies in PWRs is shown in the Figure 1.18. In 1971-1975 in some PWR reactors, fuel assemblies suffered a severe damage at different operation times at the corner location of the reactor [89]. Despite the fact that flow was nominally axial in the fuel assembly, the induced damage was significant and caused loss of the fuel integrity and fuel fragment detachment. The root-cause mechanism was a cross-flow hitting on the corner rods. High cross-flow from a gap between the corners joins of the baffle plates was streaming on corner rods and inducing buffeting which then led to fretting. Blocking the cross-flow path as illustrated in the

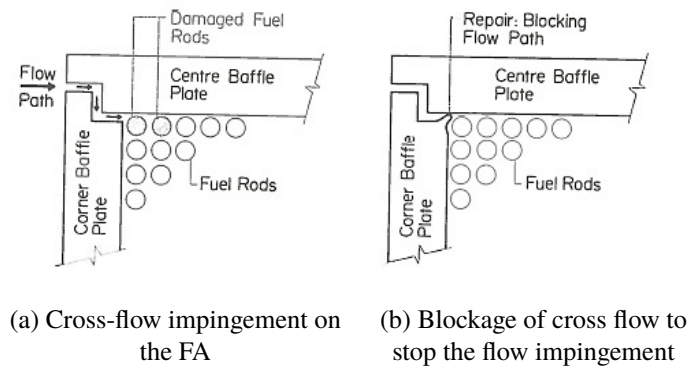


Figure 1.18. Example of the GTRF due to the cross-flow impingement [89]

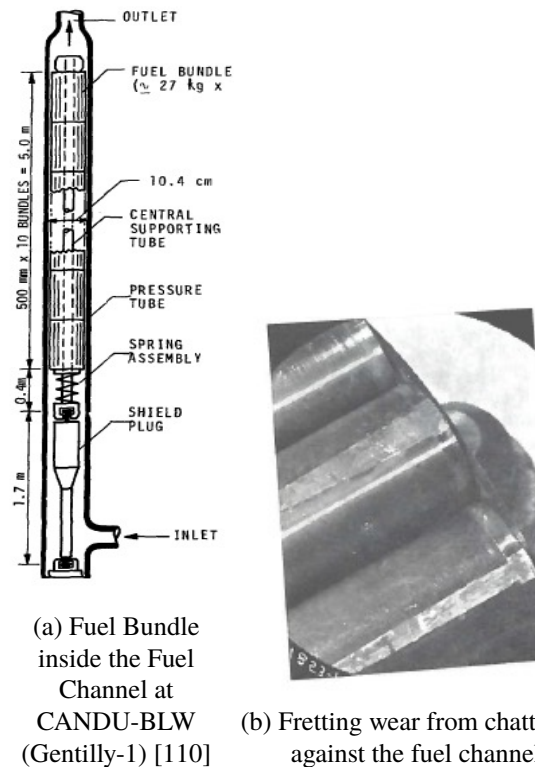


Figure 1.19. Fretting damage on Gentilly-1 Fuel Bundle [89]

Figure 1.18b and returning to axial-flow conditions resolved the occurring problem.

The final example presents the FIV induced fretting in CANDU type of reactor, Figure 1.19b. This is a classic example related to the manufacturing error in the design of the FAs. In this type of reactor fuel bundles were assembled in the confining tube and hold in place by the two support springs at top and the bottom as depicted in Figure 1.19a. The design was dedicated to ensure safety against axial flow-induced instabilities. During use, the upper part of the fuel bundle was touching the confining tube and chattering against it, which inevitably led to fretting wear. It was found that a spring at the top was assembled eccentrically due to manufacturing error, thus a string bent at one side forced by flow and chattered against the confining tube [89].

Overall, the grid-to-rod fretting (GTRF) is identified as the most common cause of fuel rod leaking mechanism, with 55% of all PWR fuel leaks in years 1994-2006 worldwide caused by GTRF [63]. Another reported problem was no tendency for PWR fuel reliability

improvement in the period from 2011-2006 [63]. Additionally, the European Fuel Group (EFG) experience shows that 83% of Advanced European Fuel (AEF) were leaking because of grid to rod fretting, while two-thirds of these occurred at the bottom grid [64]. This study found that perforation at the bottom grid occurred only for certain reactors with high cross-flow at the bottom part of the fuel assembly.

These results confirm the association between flow-induced vibrations and grid-to-rod fretting failure occurrences.

## 1.5 Conclusions

It has been shown that the turbulence-induced vibrations in the axial flow direction are of practical importance in fuel assemblies. These vibrations can induce fretting wear at the rod supports, known as grid-to-rod fretting and eventually lead to fuel perforation and consequently extended shut-downs of the reactor. Nowadays, the importance of assessing the FIV in the design stage of any nuclear component is indisputable.

Firstly, all of the presented cases has safety and radiation protection impact, and more importantly it is a nuclear safety hazard during the nuclear power plant operation. These findings clearly indicate that the major contributor to fretting is the flow-induced vibration phenomena. The improved design of the support in Steam Generators resolved the problem of the extensive vibration from the cross-flow. In contrast, the improvements in the design of the fuel assembly, subjected mainly to flow in axial direction, seem to be unsuccessful.

Secondly, the study has examined sources of FIV and their classification. The general approach in the research is to use distinction to axial- and cross- flow- induced vibrations. As shown, axial, single-phase flow is acting on the fuel rod in the PWR. Then the Nau-dasher's [90] classification of sources of excitation was used in explaining the underlying physical phenomenon causing the fretting in FA's. Turbulent buffeting (EIE) and fluid coupling effects in a closely spaced cluster of fuel rods (MIE) were identified as the major contributors to fretting.

Lastly, the axial-flow-induced vibrations are normally characterized by relatively small amplitude vibrations [100] and have so far received comparatively little research attention as opposed to other types of flow-induced vibrations. This mode of flow-induced vibration has, however, been identified as a common cause failure of 55% PWR fuel leaks worldwide [63]. Fretting wear occurred along any axial location of the fuel rod with deeper fretting marks found at the bottom of the fuel rods [64].

In conclusion, improving the methods of prediction of FIV is crucial in extending the lifespan of nuclear fuel rods. Chapter 2 will present the result on the literature survey on the axial flow induced vibrations.

## 1.6 Aims of the current study

As shown, understanding the physical mechanism that controls fluid-structure interaction for the basic configuration, such as slender structures in axial confined flow, is crucial for increasing the lifespan of nuclear components and, consequently, will positively impact financial and safety performance. The nuclear industry has identified the need for a more comprehensive and quantitative understanding of the physical mechanism that controls fluid-structure interaction for this configuration [12]. The fundamental understanding of the relation of excitation forces to vibration exerted on the fuel rods is still limited [105]. Primarily, the numerical simulation will have to be benchmarked by experiments, especially for specific configurations and flow conditions. Therefore the project will concentrate solely on the fuel rod in the fuel assembly configuration.

A recent experimental study from the authors' group on flow-induced vibrations generated by axial turbulent flow over a cantilever rod provides data on the rod displacement and local flow data, making this case highly attractive for CFD validation. The motivation for this research is thus provided by the availability of these data from reference [26].

The primary aim of this PhD project is to present a fully validated benchmark simulation of the flow-induced vibration of a free-clamped cylinder exposed to axial turbulent flow, which can inform future studies on PWR fuel bundles.

The study involves:

- Validation of the chosen FSI (Fluid-Structure Interaction) methodology against a well-known FSI benchmark case [132]. As shown, the fuel rod in the Fuel Assembly will be subjected to fluid coupling effects; therefore, the strongly coupled approach has been adopted.
- Assessment and evaluation of the URANS (Unsteady Reynolds-averaged Navier-Stokes) effective viscosity ( $k - \omega$ ,  $k - \varepsilon$ ,  $k - \omega$  SST) and Reynolds Stress models on a suitable representative 2D test case with rigid walls [15].
- Two-way FSI simulations validated against the experimental data obtained in the Department of Mechanical, Aerospace and Civil Engineering (MACE) [26]. The test rig dedicated to investigating the FIV in nuclear fuel rods was first installed in MACE in 2018 under the financial support of the EDF. The obtained data are particularly suited for FSI simulation benchmarking. The experiment will be referenced as the 'MACE' experiment.

## 1.7 Outline of thesis

This Thesis is divided into nine chapters. Chapter 1 presented the topic's importance and stated the current research's purpose. Chapter 2 begins with a literature review on axial

Flow-induced Vibration. Chapter 3 details the equations which govern the solid linear-elastic displacements. Chapter 4 focuses on the implementation details of the turbulence models used in the engineering practice. Chapter 5 is concerned with the fluid-structure interaction coupling methodology employed for this study. Chapter 6 and Chapter 7 summarize the numerical methods applied to this project, along with details on implementation in the numerical code which was used. Chapter 8 is concerned with the simulations methodology employed for this study. Every test case is validated against numerical and experimental data found in the literature. The final Chapter 9 summarizes the main findings of this project and provides suggestions for future work on the subject.

# Chapter 2

## Literature review

The section below reviews fundamental literature publications on axial flow-induced vibrations. The section has been divided into three parts. The first part presents the analytical solution of the response of the cylinder due to axial fluid loading. The second part is dedicated to experiments analysing the motion of a slender beam subjected to the axial flow. Finally, the third part presents the results of numerical investigations in the same area.

### 2.1 Analytical models

A study of the linear equation of motion for slender flexible cylinders with different boundary conditions (e.g. clamped-clamped, clamped-free) in confined axial flow was first developed by Païdoussis [101, 103] using the Newtonian approach. The proposed expression for fluid forces acting on the slender body was further developed by many researchers eg. Rinaldi [115], Ricciardi et al. [114], Chen [23], Basile [3], Pettigrew [110]). His theory splits the fluid forces acting on the cylinder into inviscid forces and viscous forces. The inviscid force is normal to the surface and is based on the motion-induced inviscid forces theory by Lighthill in 1960 [82]. The viscous forces in the normal and longitudinal direction are based on the formulation of Taylor in 1952 [126].

The equations of motion obtained via non-linear dynamics will not be particularly interesting in further studies. The reason is that the non-linear theory is used to determine the amplitudes of vibration above the critical velocity, e.g. flutter. In practice, fuel rods never experience high amplitude and fluid-elastic instability from external axial flow; therefore, there is no need to apply non-linear dynamics equations for this particular application.

The relationship between the beam's deflection  $y(x)$  and the applied load  $q$  is given by Euler-Bernoulli static beam theory, Equation 2.1c:

$$M = EI \frac{d^2 y}{dx^2} \quad (2.1a)$$

$$q = \frac{d^2 M}{dx^2} \quad (2.1b)$$

leads to:

$$q = \frac{d^2}{dx^2}(EI \frac{d^2 y}{dx^2}) \quad (2.1c)$$

Where  $M$  is the bending moment,  $q$  load per unit length,  $y$  deflection in a transverse deflection at a position  $x$  along the beam.  $E$  is the elastic modulus, and  $I$  is the second moment of area of the beam's cross-section. The cross-section of the beam is constant along its length. When the load  $q$ , is removed from a displaced beam, the beam will return to its original shape. The inertia of the beam will cause the beam to vibrate around that initial location. Downward inertia force on the beam is:

$$q = -m_{rod} \frac{d^2 y}{dt^2} \quad (2.2)$$

Where  $m_{rod} = \rho A$  is the mass of the beam per unit length.

Finally, the differential equation for a freely vibrating slender beam with a uniform cross-section is [44]:

$$EI \frac{d^4 y}{dx^4} + m_{rod} \frac{d^2 y}{dt^2} = 0 \quad (2.3)$$

Where,  $y = y(x, t)$  is deflection at given time  $t$  and location  $x$ .

The beam vibrates harmonically at some natural frequency  $f_N = \omega_N/2\pi$  and the associated mode shape  $\widetilde{y}_N(x)$ . The general solution will have the form:

$$y(x) = C_1 e^{ax} + C_2 e^{-ax} + C_3 \sin ax + C_4 \cos ax \quad (2.4)$$

With coefficient  $a$  chosen that:  $a = \sqrt[4]{\frac{m_{rod} \omega_N^2}{EI}}$

For a clamped-free beam, bending moment  $M$  and the shear force  $S$  are zero at the free boundary.

$$M = 0 \quad (2.5a)$$

$$S = EI \frac{d^3 y}{dx^3} = 0 \quad (2.5b)$$

Thus, the boundary conditions at the free-end are:

$$\frac{d^2 y}{dx^2} = 0 \quad (2.6a)$$

$$\frac{d^3 y}{dx^3} = 0 \quad (2.6b)$$

Finally, the approximate solution satisfying the conditions is:

$$\widetilde{y}_N\left(\frac{x}{L}\right) = y_0(1 - \cos(\frac{\pi x}{2L})) \quad (2.7a)$$

$$f_N = \frac{c_N^2}{2\pi L^2} \sqrt{\frac{EI}{m_{rod}}} \quad (2.7b)$$

Where  $c_N$  is the natural frequency parameter. Cantilever beam mode shapes and corresponding  $c_N$  parameters are presented in Figure 2.1.

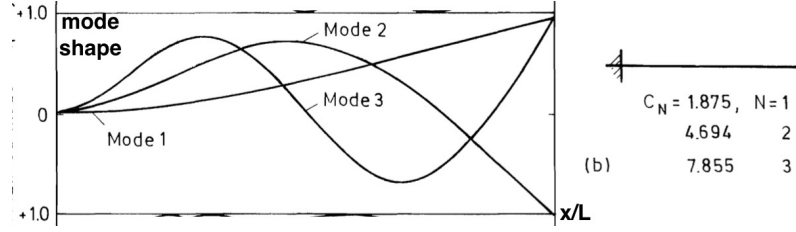


Figure 2.1. Mode shapes and natural frequencies for the first three modes for a cantilever beam [90]

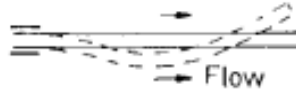


Figure 2.2. Rod with external axial Flow [90]

The schematic of the system body vibrating in a flowing fluid is presented in Figure 2.2. In this case, fluid forces acting upon the structure can be subdivided into the mean and fluctuating part,  $F(t) = \bar{F} + F'$ . The former is treated as the mean hydrodynamic loading and the latter results from the fluid fluctuations. In the analyzed case of fuel rod subjected to the axial flow, fluid fluctuations arise from turbulent eddies impinging on the structure [90]. In the case of multiple bodies submerged in the otherwise stagnant fluid (e.g. flow acting on the fuel assembly), the  $F(t)$  acting on the single beam should be altered when the body starts moving. The general equation of motion describing the forced vibration of a slender, uniform beam is [90]:

$$EI \frac{d^4 y}{dx^4} + m_{rod} \frac{d^2 y}{dt^2} = F = F_y^d + F_y^e \quad (2.8)$$

Where,  $F$  is the sum of damping:  $F_y^d$  and exciting forces:  $F_y^e$ , which are due to the moving fluid. Researchers' main challenge is in determining the expression for the excitation force  $F(t)$  from the fluid acting on the beam.

The dynamical behaviour of a slender body immersed in a fluid and subjected to axial flow was comprehensively studied using linear dynamics by Paidoussis [106]. The derived equation of motion was capable of predicting the critical velocity at which the slender beam loses stability. In order to briefly present the theoretical concept, the cantilever beam subjected to the axial flow is presented in Figure 2.3a. Point  $P$  is the point on the cylinder where the small element  $\delta x$  is located (depicted in Figure 2.3b). Motion is assumed to be two-dimensional in the x-y plane, and the pressure  $p$  is assumed to be a linear function of location  $x$ . If the cylinder from the Figure 2.3 would be submerged in the stagnant fluid, only the hydrostatic forces  $F_{px}$  and  $F_{py}$  from the mean pressure  $p$  will be acting on the outer sur-



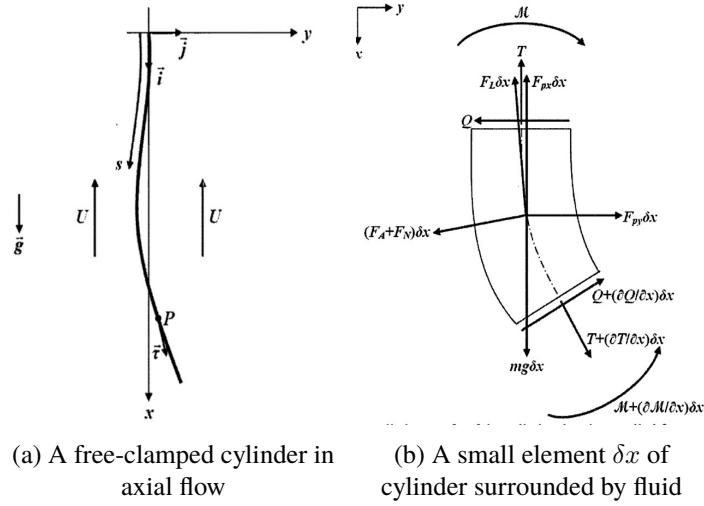


Figure 2.3. Example of a beam in flowing fluid showing applied forces and moments [115]

faces. When the fluid starts to flow, the elastic cylinder deforms and accelerates the neighbouring fluid.  $F_A$  is the added acceleration resulting from the fluid velocity in the y direction.  $F_L$  is lift (force in the normal direction) and  $F_D$  is drag force (force in longitudinal direction). The strength of these forces depends on the trailing end of the body. Force  $T$  is denoted as the axial tension from the fluid acting in the axial direction. The force  $T$  can be decomposed into the mean and fluctuating component  $T(t) = \bar{T} + T'$ . The final equation should account for the linear added mass of the confined water,  $m_{add}$ . In the general Equation of motion 2.8, the external force  $F$  is applied in the y direction to the beam axis. Combining all identified fluid forces gives the linear equation of motion of a flexible free-clamped cylinder in axial flow:

$$EI \frac{\delta^4 y}{\delta x^4} + (m + m_{add}) \frac{\delta^2 y}{\delta t^2} = (F_A + F_N) - F_{py} - \frac{\delta}{\delta x} \left( T \frac{\delta y}{\delta x} \right) \quad (2.9)$$

The main weakness of this model is that it fails to explain the impact of the viscosity of a fluid. The book [106] fails to provide information on the main characteristic of turbulent flows. Only brief information about the necessity of scaling the lift and drag forces by the skin friction coefficients is given. Overall, Paidoussis work on slender structures in axial flow [97, 103, 106] is limited in that it assumes fluid viscous forces do not dominate the dynamics of a structure in highly turbulent flows. The pressure field is assumed to be homogeneous. The forces result from the mean pressure  $p$  acting on the cylinder surface. Consequently, the model will neglect small amplitude rod vibrations, caused by pressure fluctuations in the flow field.

In order to improve the model, Chen [22] extended the equation 2.9 to the viscoelastic materials. The study takes to account the viscosity of a material and its viscous damping effect. The general equation is extended for the coefficients for the cylinder vibration near the wall in a concentric fluid annulus and multiple cylinders. The derived equation of motion is deficient in that it does not take to account the viscosity of a surrounding fluid.

Basile [3] first proposed the approach to find the function of the dimensionless amplitude

of vibration ( $\frac{A_y}{D}$ ) in terms of non-dimensional parameters governing the fluid flow, based on experimental results. His analysis provides an extensive number of experimental results and comparisons with those of other researchers. The importance of random pressure fluctuations generated by the turbulent eddies was also emphasized in the work of Wambsganns [136]. The paper provides an equation for root-mean-square (RMS) displacement for a flexible rod in axial flow, based on the results of in-house experiments. However, the study would have been more useful if it had included the experiments' details and their results. Comparative experimental data of the pressure fluctuations generated by turbulent boundary layers can be found in the further work of Chen [22, 23]. However, the results are found to be not reliable for the low-frequency pressure fluctuations.

Finally, the work of Rinaldi [115] distinguish the dynamics of a structure depending on the direction of the axial flow. The study offers an extensive analysis of the rod motion depending if it was submitted to the aspirating flow or in the opposite direction of flow. The approach is the same as that of the Paidoussis' [106], but the general equation of motion 2.9 is scaled by a factor for the fully turbulent flow. One of the most noticeable differences between the work of Rinaldi [115–117] and her precursors is that numerous experiments were performed to validate the theoretical models.

### 2.1.1 Summary

Overall, these studies show weak evidence of turbulent-induced excitation from the external axial flow. The main weakness of the approach is a large number of parameters in the amplitude relation. Analytical models are quite convenient in predicting high-frequency vibration of structures subjected to the axial flow. However, these could be applied only for simple configurations and linear-elastic material. The turbulent coefficients obtained through empirical functions are not valid for low-frequency oscillations. Also, viscous coefficients dedicated for lift and drag estimations are not valid for small yaw angles [45]. Finally, analytical models which estimated vibrations for a cantilever fixed at the upstream end cannot be applied to the same case with a cantilever fixed at the downstream end.

The next section reviews the literature related to experimental results.

## 2.2 Experiments

An experimental approach is one of the most common procedures for predicting flow-induced vibration frequency. Several studies have investigated the influence of a tapered shape on the trailing end of a cantilever beam subjected to the axial flow [26, 45, 102, 104, 116, 117]. Some authors have considered the effect of far-field disturbances [3, 72, 80, 93]. Much of the current literature on predicting FIV frequencies focuses on the non-invasive velocity measurement method - PIV. Velocity contours are accompanied by simultaneous displacement, or pressure measurement at the wall [14, 15, 26, 57, 58].

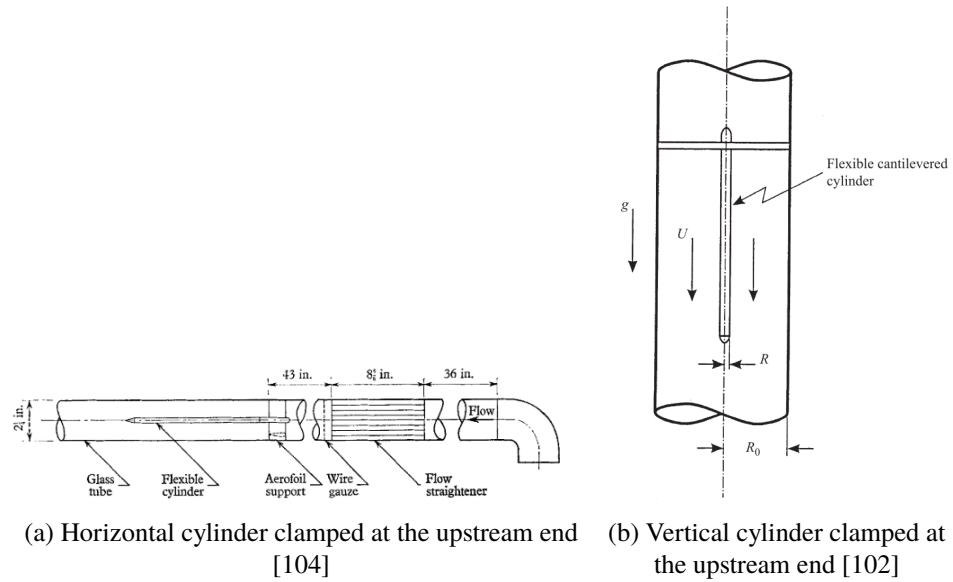


Figure 2.4. Schematic view of the experimental apparatus in 1966 (a) and in 2002 (b)

### 2.2.1 Effect of the free-end shape of a cantilever

Païdoussis [102, 104] was one of the first to examine of influence of the cantilever end-shape on the dynamics of a cylinder. The first detailed study was conducted with a flexible rubber cantilever mounted horizontally with clamped at the upstream end, as presented the Figure 2.4a. In the second test campaign, the flexible cylinder was placed vertically, with the same flow direction, Figure 2.4b. The tested end shapes are depicted in Figure 2.5. Both experiments for almost ideally streamlined-end instability occurred at a significantly lower velocity than for a blunt-end shape. In the case of shape,  $H$  presented in Figure 2.5a, the cantilever remained stable to the maximum available flow velocity. The same was observed in the later experiments with a cantilever mounted vertically, Figure 2.5b. As explained for an ideally streamlined end, viscous force in the normal direction, lift, acting on the trailing end of the body dominate its flexural restoring force. For a blunt-end, the lift force is compensated with the viscous force in the longitudinal direction - drag force.

The influence of an end-shape was further examined by Rinaldi and Païdoussis in 2012 [117], where the flow was directed from the free end towards the clamped end, Figure 2.6. Interestingly, in this case, the variant end shape did not change the dynamic response of the cantilever.

Divaret et al. [45] studied the fluid forces exerted on a yawed cylinder with a streamlined end, with an angle of inclination  $\alpha$  below  $5^\circ$ . The comprehensive experimental study found that the normal force exerted on a cylinder oscillates perpendicularly to the flow. Normal force varies linearly with the angle of inclination, and its dominated by the lift component. The drag component has only 10% contribution. Further, the lift force originates from the pressure surrounding the cylinder, and the skin-friction coefficient related to the surface roughness is negligible. Divaret demonstrated that Taylor's formula for the viscous forces in normal and longitudinal direction [126], used widely in the analytical models (presented

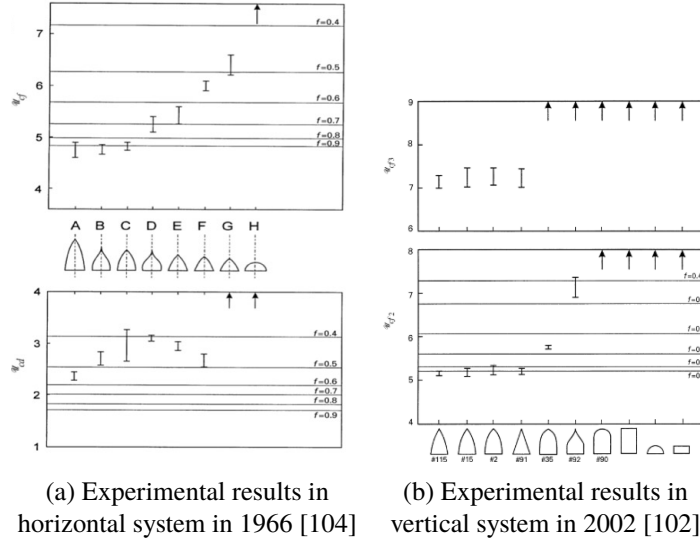


Figure 2.5. The effect of the shape of tapered end on the stability of cantilevered cylinders in 1966 (a) and in 2002 (b)

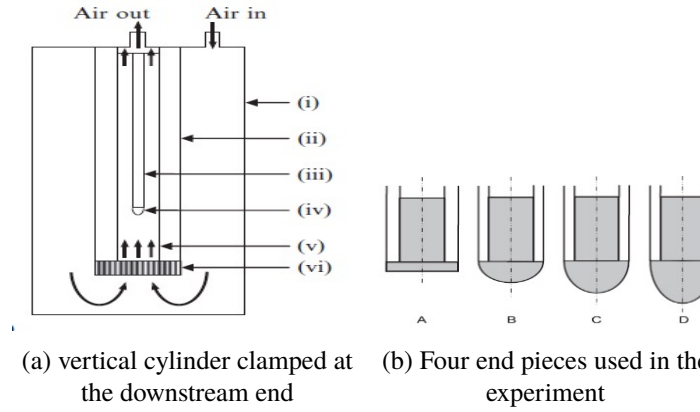


Figure 2.6. Schematic view of the experimental apparatus in 2012 [117]

in Section 2.1), does not hold for small yaw angles.

Lastly, two opposite beam end shapes, blunt-end and the curved end were tested in MACE in 2018 [26]. In the experiment, the flow was directed from the rod-free end to the clamped end. Representative flow visualisation for the two beam ends is depicted in Figure 2.7. The results of the experiment indicate that the beam end shape does not have an influence on the cantilever dynamics below a certain critical velocity, and vibrations are only due to the turbulent buffeting from the external flow. These results are similar to those reported by Rinaldi [117]. However, above the critical velocity, the movement of the rod is large enough to perturb the flow field, which is an additional source of excitation. The graph 2.8a shows that there has been a gradual increase in the amplitude of vibration with the increase of velocity. What stands out in this Figure is the high amplitude of vibration of the blunt-end, as opposed to the amplitude of the streamline-end. This is due to the significant perturbation of the flow field from the blunt end piece. In both cases, the vibration frequency decreases slightly as shown in Figure 2.8b.

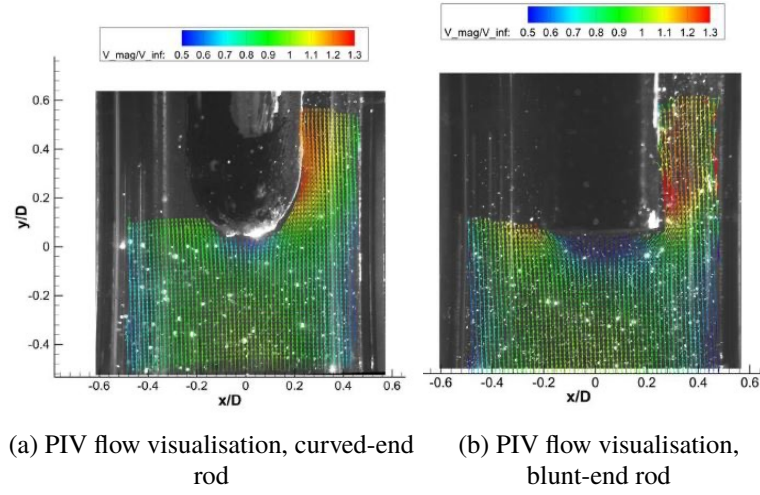


Figure 2.7. Flow visualisation of two end pieces at the low flow velocity ( $u = 35.4$ ) [26]

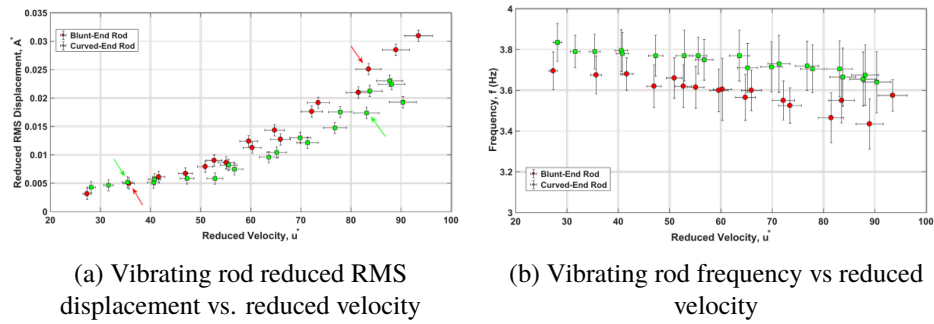


Figure 2.8. Rods flow-induced vibration, arrows indicate that data points that were further analysed with the PIV. [26]

### 2.2.2 Effect of far-field disturbances

It was found that disturbances from the pumps transmitted through flow contributed to the increase in vibration amplitude. To examine the influence of that far-field flow noise in the system, Basile et al. [3] used two different pumps in the closed loop, as shown in Figure 2.9a. Pump  $P2$  was placed directly under the test channel during the test. It was shown that high amplitude vibrations with a frequency of 50Hz are due to the pump  $P2$ , as shown in the graph depicted in Figure 2.9b. To further examine the role of other system parameters such as flow asymmetry and clearance in the attachments, Basile set up the rod in an eccentric position. It was observed that the increase in eccentricities of 50% led to an increase of up to 7 times in the relative amplitude of vibration. In addition, it was found that when the rod is assembled with a small clearance in the support, the amplitude of vibration can increase even up to 4 times.

These experiments are similar to those reported by Ohlmer et al. [72, 93]. In the series experiments, additional perturbations of the flow from a pump were introduced, and the influence of the test loop agreement was tested. It was confirmed that a sharp peak at 50Hz depicted in Figure 2.9c resulted from the flow pulsations generated by the pump.

In contrast to these findings, the experiments by Lane et al. [80] on the prototype of fuel assembly for CANDU reactors showed that far-field noise effects are much less important as

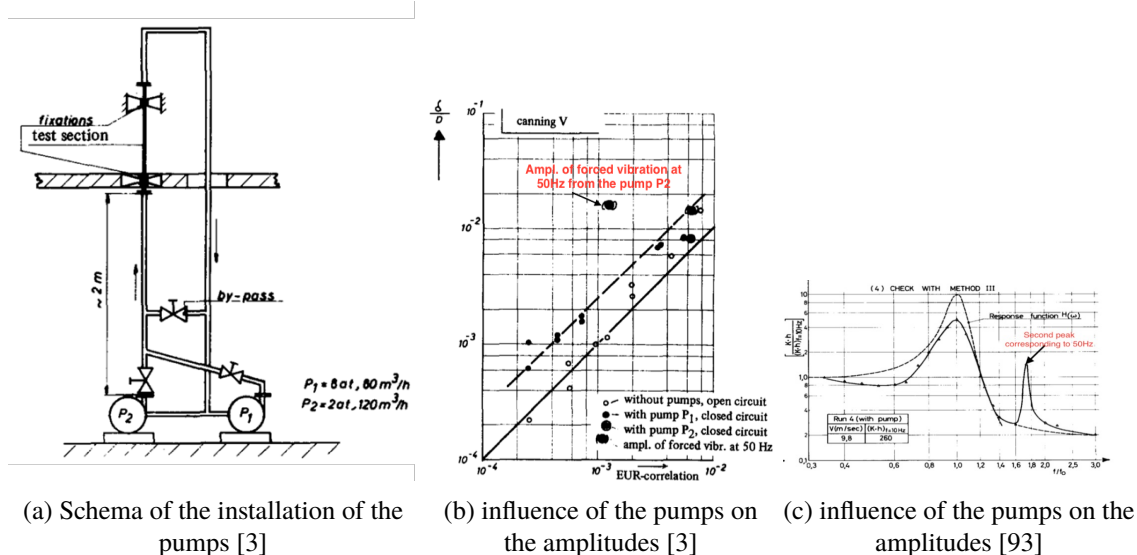


Figure 2.9. Influence of pumps on the amplitude of vibration

compared to the near-field turbulence. The case study explained that pump pressure fluctuations have a higher impact in a small loop system than in large volume reactor systems; hence, results from the prototype test represent the worst-case scenario as opposed to the fuel element in a large power reactor.

### 2.2.3 PIV measurements

A number of studies have begun to examine the influence of turbulent buffeting with particle image velocimetry (PIV) with simultaneous measurement of pressure coefficient or displacement of the body. The approach makes the obtained data particularly suited for benchmarking the Computational Fluid Dynamics (CFD) models and Fluid-Structure Interaction (FSI) models. In experiments presented below, the frequency of pressure fluctuations  $f$  has been scaled with the Strouhal number,  $St = \frac{fL}{U}$  where  $U$  is the flow velocity and  $L$  is the characteristic length.

Higuchi et al. [57, 58] investigated the shear flow separated at the leading edge of blunt cylinder at  $Re = 10^5$ . An example of the flow visualisation of the cylinder subjected to turbulent, axial flow is depicted in Figure 2.10. The experiment was conducted with the use of magnetic suspension of the cylinder. A balance system was used to measure the drag force exerted on the body. The study revealed large-scale vortices impinging on the structure at the leading edge and further downstream helical vortex structures. The wake behind the cylinder was asymmetrical and unsteady. The peak pressure fluctuations, were observed at frequency of around  $St = 0.012$  (1.5Hz) and  $St = 0.081$  (10Hz). It was concluded that the low-frequency oscillation originated from the axisymmetric pulsation of the recirculation bubble. This can also be described as the flapping motion of a recirculating bubble.

Taking the same approach, Camussi [15] demonstrated that the largest pressure fluctuations are due to the reattachment phenomenon on the forward-facing step. The averaged vorticity field with the approximate position of the reattachment point is depicted in Figure

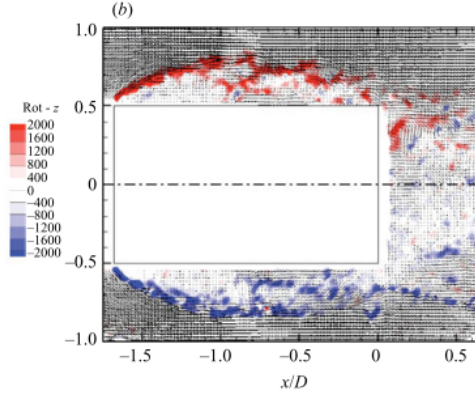


Figure 2.10. Instantaneous vorticity and velocity field over the blunt cylinder,  $Re = 10^5$  [58]

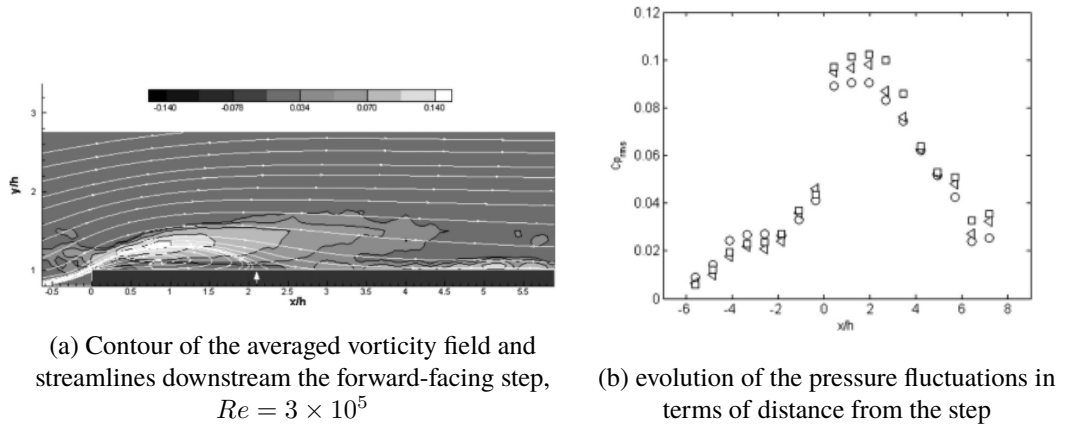


Figure 2.11. Results of the PIV measurements and simultaneous pressure measurements [15]

2.11a. The unsteady recirculation bubble is formed at the reattachment region downstream of the step, in this case, for the location  $x/h < 2.1$ . Again, the flapping motion of the recirculation bubble is causing the low-frequency pressure oscillations, characterised by the Strouhal number of around 0.01. The simultaneous pressure measurement shows that the evolution of pressure fluctuations reaches a maximum in the average location of the reattachment point. It is depicted in Figure 2.11b, where statistics of pressure fluctuations were expressed as root mean square pressure coefficient  $Cp_{rms}$ . It is important to highlight that the forward-facing step geometry induces larger pressure fluctuations near the wall than the backwards-facing step [14].

The test rig dedicated to investigating the FIV in nuclear fuel rods was first installed in MACE in 2018 under the financial support of the EDF [26]. The geometry of the experimental system was designed to correspond to the water-cooled reactor flow conditions. The flowing mass flux range represents the nuclear reactor mass flux range. Additionally, the test section has an embedded flow straightener, and the pump location is relatively far from the inlet. The rod subjected to the axial flow is long, circular, stainless steel tube filled with lead shot to approximate the uranium density. The motion of a free-end is recorded with a fast-imaging camera, and in the same time frame, the second camera tracks the flow field.

Interestingly, the instantaneous velocity visualisation Figure 2.7 did not reveal a flow de-

Table 2.1. influence of the beam end-shape and direction of the flow on the cantilever beam

Cantilever beam - flow direction	Trailing end geometry	Effect on amplitude	References
flow from fixed-end to free-end	blunt end	relatively low amplitude of vibration	[101, 102, 104]
	streamline end	relatively high amplitude of vibration	
flow from free-end to fixed-end	blunt end	high amplitude of vibration above $U_{cr}$	[26, 115–117]
	streamline end	slightly lower amplitude of vibration above $U_{cr}$	

tachment event for the blunt-end. It has been assumed that the time scale of induced movement is much bigger than the time scale of the flow. Therefore fluid has enough time to adapt to the movement of vibrating rods. Their reason could be, however, due to the relatively small resolution of the PIV study. Nevertheless, the detailed study of the rod's free-end displacement makes a valuable contribution to the FSI model benchmarking.

## 2.2.4 Summary

The studies on the experimental approach indicate that in the case of a cantilever subjected to the axial flow, the amplitude of vibration depends strongly on the beam-end shape and direction of flow approaching the beam. In the case where flow is directed from the clamped end towards the free end, the amplitude of vibration is stronger for the streamlined end due to the lift force exerted on the beam. The importance of turbulent-induced excitation was firstly emphasised in the case of the blunt-end rod with the flow directed from the free-end towards the clamped-end. Above a certain velocity threshold, the blunt end vibrates with higher amplitude than the streamlined end. Overall, all these studies show that the amplitude of vibration increase with the increased flow velocity. The beam's natural frequency decreases with the increased flow velocity. For the flow-induced vibrations experienced in the nuclear fuel rods, the configuration of interests is flow directed from the free end toward the fixed end. The results of the literature review are summarised in Table 2.1.

The modern approach to assessing FIV is the PIV flow visualisation with simultaneous pressure/displacement measurement. The studies presented thus far provide evidence that large-scale, low amplitude vortices impinging on a structure are the dominant source of excitation on the beam. The peak of the pressure fluctuations occurred at the reattachment length. Hence pressure fluctuations are stronger in the forward-facing step than in the backwards-facing step [14]. It is important to verify whether the pressure spectra provided in the literature were cleaned from the background flow noise. A summary of experimental studies suitable for the FIV assessment in the nuclear industry is listed in Table 2.2. The presented cases can be successfully adopted as validation cases for the FSI simulations.



Table 2.2. Experimental studies of FIV from axial turbulent flow

Beam support conditions	Reynolds Number	Tube material	Fluid	Measured properties	References
fixed-fixed	$0.5 - 1 \times 10^5$	bras	water	frequency, damping	[22, 23]
fixed-free	$0.5 - 1 \times 10^5$	bras	water	frequency, damping	[22, 23]
hinged-hinged	$< 10^5$	aluminium	air, water	amplitude	[3]
fixed-spring	$10^6$	steel	water	PIV, pressure, displacement	[60, 127]
Rigid structures applicable for FIV					
Forward-facing step	$1 \times 10^5$ & $3 \times 10^5$	-	water	PIV, pressure	[15]
Blunt cylinder	$1 \times 10^5$	-	water	PIV, pressure	[57, 58]

## 2.3 Fluid Structure interaction simulations

The literature on the Fluid-Structure Interaction simulations will highlight several prominent numerical models developed for the flow-induced vibrations in nuclear fuel rods.

De Ridder et al.[35] simulated the instabilities of a flexible, empty tube subjected to the eutectic lead-bismuth fluid. This has practical importance in the design of the MYRRHA reactor. Reynolds number with the lead-bismuth flow is  $5.6 \times 10^4$ . The flow was computed using unsteady Reynolds-averaged Navier-Stokes (URANS) with the  $k - \omega$  SST model of Menter. The approach to solving fluid equations involves the discretisation of the spatial terms with a second-order upwind scheme and second-order time discretisation. The structural computations are performed with the finite element method, with the second-order time discretisation. The coupling involves the IQN-ILS method. No re-meshing method was adopted because the predicted displacements were on the order of  $10\mu m$ . The methodology was validated with the experiments of Chen & Wambsganns [23] for vibrations of a solid clamped-clamped cylinder in water flow where Reynolds number ranged from  $1.27 \times 10^5 - 3.81 \times 10^5$ . Calculated frequencies of vibrations showed good agreement with the experiments. However, the time history of the displacement showed that vibrations were damped. That clearly shows that excitation due to fluctuating pressures is absent. The study on grid refinement showed no difference in displacement when using wall functions or solving the near-wall region. In further work, De Ridder [32, 33] studied solitary rods and tightly packed rods subjected to axial water flow with the same methodology. However, the study involved the influence of increasing the velocity above the critical threshold and further fluttering amplitude of the rod. According to the fuel rod failures review presented in Section 1.4, the flutter of the rod has never occurred, and damage was only due to the small-amplitude vibration imposed by the pressure fluctuations.

In their numerical simulations, De Santis & Kottapalli [36] performed strongly coupled FSI simulations on two tightly packed rods. The approach on the fluid side was again the URANS  $k - \omega$  SST model with the second-order upwind scheme for discretising the spatial terms and second-order implicit temporal terms. On the solid side, the finite element

method with the second order temporal scheme was applied. The Aitken under-relaxation coupling scheme was chosen. Interestingly, due to the relatively small pitch to diameter ratio ( $\frac{P}{D} = 1.27$ ) and high Reynolds number  $Re = 2.4 \times 10^5$ , the appearance of the flow pulsations in the gap between two rods was detected. The movement was triggered by the flow itself, and due to the pulsations of pressure in the gap, vibrations remained self-sustained without being damped out. The study is limited in that it fails to provide validation of the numerical model against experiments or analytical models. The frequency of vibration was estimated at 100-120Hz. The study would have been more relevant if the researchers had provided information on the frequency in the non-dimensional form.

In the later study of De Santis et al. [37] performed simulations of fuel rods subjected to the axial water flow and lead-bismuth flow at  $Re = 9.2 \times 10^4$ . The turbulent flow was numerically solved with the URANS  $k - \omega$  SST turbulence model by Menter. The paper fails to specify the discretisation approach used in the study. The solid displacement was solved with the finite element method as linear-elastic material. The Aitken under-relaxation was chosen for the coupling. It was found that the major problem with this approach of modelling, is its ability to sustain vibrations. The rod was perturbed with an initial force, but vibrations appeared to be gradually damped. A similar study by the authors [38] on a wire-wrapped rod showed the same result. Moreover, vibrations in the lead-bismuth flow appear completely vanish by the time of less than 0.3s. The research is limited by the fact that rod frequency estimation relies on that short time of vibration.

Kottapalli et al. [77] adopted the  $k - \omega$  U-RANS model. In contrast to the previous research, velocity and pressure fluctuations were generated with a stochastic model and applied as additional external excitation on the structure. The validation of the pressure fluctuation model with the DNS simulation revealed an underestimation of the pressure fluctuations near the wall. In general, the study found that pressure fluctuations are still much better represented than solely applying the standard k-omega U-RANS. The validation of the model against the experiments of Chen & Wambsganns [23] shows that the vibrations remained self-sustained, with an error of 7% for the modal frequency. However, the amplitude of vibration was five times less compared to the experimental values. The observed increase in the amplitude of vibration, as opposed to the U-RANS model, can be attributed solely due the artificial random number generator for the turbulent pressure field.

One study by Hofstede [127] examined two U-RANS models to simulate the turbulence-induced vibrations:  $k - \omega$  SST and the Reynolds Shear Stress Models (LRR). Simulations were validated against experimental data dedicated to vibrations induced on a steel tube from a turbulent flow, where one end of the tube was fixed and one end fastened with a spring. The fundamental frequency of the experimental system ranges from 8-9Hz. The initial force was applied to the solid to trigger the vibrations. For the fluid, the second order upwind scheme was used for the spatial discretisation, and the second order backward scheme was used for temporal discretisation. The results of the research demonstrated that both turbulence models are incapable of simulating external excitation on the structure solver. The vibrations resulting from initial perturbation get quickly damped out. Another impor-

tant part is the convergence study of the solid solver. On the solid side the finite volume method (FVM) and finite element (FE) method were compared. It was concluded that FVM needs a much finer mesh and smaller time-step to converge than the FE discretisation method. The author fails to specify the influence of choosing the FE method on the final results of the FSI simulation. The non-conformal meshes could induce much larger errors than anticipated. Also, the report provides little evidence that the pinned boundary condition at one end of a beam is an adequate choice to reproduce the experiment.

The most comprehensive numerical study of FIV in nuclear fuel rods has been undertaken by Christon [25]. The study involves the assessment of three turbulence models: LES, DES and URANS, with a mesh refinement using five mesh grades. It has been shown that the LES model presents adequate force fluctuations to assess the GTRF further. The large-eddy simulation model was further applied on the fluid side with the structure considered rigid. The computed flow-induced forces extracted from the CFD simulation were then transferred to the vibration analysis software dedicated to vibrations in nuclear fuel rods. The article provides valuable insights to LES flow simulation for the full fuel assembly design and offers a detailed analysis of the pressure fluctuations along the fuel rods. The results were validated against PIV experimental results provided by Westinghouse. It was shown that the RMS pressure is highest at the downstream end of the spacer grid, where the level of turbulent kinetic energy is the largest.

### **2.3.1 Summary**

Many researchers have utilised strongly coupled FSI simulations which is the most widely used technique in analysing FIV. While the simulations are quite fast and convenient in predicting the dominant frequency of the fuel rod subjected to the axial flow, the literature review exposed many shortcomings in the previous simulation approaches. Previous studies had based their assessment of dominant frequency on one or two cycles of vibration before the amplitude got damped out, and excitation due to fluctuating pressure was absent, i.e. [35, 37, 38, 128]. These studies have also predominantly focused on determining the natural frequency of vibrating beams in the presence of highly turbulent flow and have failed to consider the flow-induced amplitude of vibrations. In contrast, studies of [39, 77] increased an external excitation on the fuel rod by applying an artificial random number generator for the turbulent pressure field. The validation against experimental data still revealed an underestimation of the amplitude of induced vibrations. So far, only the LES approach [25] was found to give reliable results, but it is computationally expensive, hence an inaccurate choice for the nuclear components.

## **2.4 Conclusions**

To date, various methods have been developed and introduced to measure the flow-induced vibration frequency and amplitude. The literature review identified three main sub-groups

developed for analysing flow-induced vibrations:

- Analytical approach to derive a linear equation of motion for slender flexible cylinders in confined axial flow. Also investigation of the function of the dimensionless amplitude of vibration ( $\frac{A_y}{D}$ ) in terms of fluid flow non-dimensional parameters was presented.
- An experimental approach, the most common procedure for predicting flow-induced vibration frequency. It is used to establish empirical correlations to fit measurements or visualise the flow field around the shape of interest with simultaneous pressure measurement.
- Fluid-Structure Interaction simulations, numerical approaches that have been developed for the flow-induced vibrations in nuclear fuel rods.

This review has demonstrated the shortcomings of the experimental approach to assessing FIV. In order to predict the vibration response of fuel rod in axial flow experimentally, one needs to input a pressure field on the rod surface in a prototypic assembly in the frequency range below 300 Hz, estimate the contribution of far-field flow noise from pumps, and predict the influence of other factors. Most experiments in the literature use flexible rods to validate models for the predicted onset of divergence or flutter. Consequently, experiments on dynamic response in the range of small vibration amplitudes are lacking and there is little published data on experiments on vibrational characteristics: natural frequency, mode shapes and damping of cantilevered cylinders with different end-piece under the axial flow. From the practical perspective, such results will be especially useful for control rods or fuel rods, which were found to be subjected to the FIV wear [12].

There are obvious difficulties in assessing the amplitude of FIV with the use of analytical models. Firstly, the cylinders are generally modelled as simple Euler-Bernoulli beams. Even if the derived new analytical model is successful, it would not be possible to extend it to more complex geometries (i.e. fuel assembly component). Secondly, the pressure field is assumed to be homogenous. That is, the mean-square spectral density of the pressure is the same at any rod point. While the evolution of the pressure fluctuations in relation to step distance was discovered in the PIV experimental cases (Section 2.2.3).

Recent studies using coupled Computational Fluid Dynamic (CFD) and Computational Structural Mechanics (CSM) present an alternative to overcome these deficiencies. Previous studies have demonstrated well-developed methods to determine modal characteristics such as natural frequencies and damping ratios of vibrating beams in the presence of highly turbulent flow. It has been shown that fretting wear increases strongly with a larger amplitude of fuel rod vibration [9]. Since an excessive vibration amplitude is a leading cause of grid-to-rod fretting, it becomes crucial to assess the flow-induced amplitude of vibration with good accuracy. Previous studies have predominantly focused on determining the natural frequency of vibrating beams in the presence of highly turbulent flow and have failed

to consider the flow-induced amplitude of vibrations. Also, the only identified suitable turbulence model, LES, for this purpose is computationally expensive. None of the numerical studies reviewed appears to achieve reliable results with the use of approaches which are practical in industrial applications.

Overall, these studies highlight the complexity of determining the small amplitude, flow-induced vibrations induced by external, axial, turbulent flow. This consequently indicates a need to assess the numerical modelling approaches for the flow-induced vibrations. In the Chapter that follows, the mathematical description of the solid linear-elastic displacements is presented.

# Chapter 3

## Governing equations of solid elastic displacement

### 3.1 The Navier-Displacement Equations

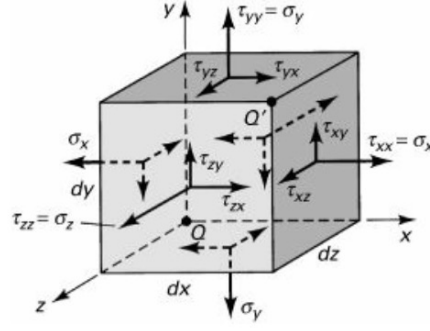
In this Chapter, a full derivation of the governing equations of elasticity is presented with constitutive relations of solid material stress to the material strains. The governing equations of linear elastic deformation in terms of displacement are derived. As shown in Chapter 2 the fuel rod is subjected to small strains; hence the linear elastic model is sufficient to apply during the modelling process. The simplification of the current study is to assume the isothermal elasticity and no influence of thermal expansion is considered.

### 3.2 Mathematical Model of Solid Deformation

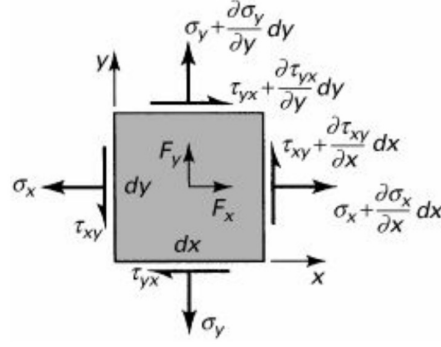
Surface forces and body forces are two types of external forces that act on a body. Body forces are associated with mass and are distributed throughout the volume of a body. Body forces include gravitational, magnetic, and inertial forces. They are specified in terms of force per unit volume. Normal and shear forces are surface forces as they are exerted on the surface of an object. The general case of a three-dimensional state of stress is shown in Figure 3.1a. Stresses are uniformly distributed on each face, where stress is defined as force per unit area. The total of nine scalar stresses components define the state of stress at a point. The stress components are assembled in the matrix form, wherein each row represents the group of stresses acting on a plane passing through point  $Q(x, y, z)$ :

$$[\sigma_{ij}] = \begin{bmatrix} \tau_{xx} & \tau_{xy} & \tau_{xz} \\ \tau_{yx} & \tau_{yy} & \tau_{yz} \\ \tau_{zx} & \tau_{zy} & \tau_{zz} \end{bmatrix} = \begin{bmatrix} \sigma_x & \tau_{xy} & \tau_{xz} \\ \tau_{yx} & \sigma_y & \tau_{yz} \\ \tau_{zx} & \tau_{zy} & \sigma_z \end{bmatrix} \quad (3.1)$$

Normal stresses acting in direction normal to the face are  $\tau_{xx}$ ,  $\tau_{yy}$ , and  $\tau_{zz}$  designated as  $\sigma_x$ ,  $\sigma_y$ , and  $\sigma_z$  respectively. From Newton's Second Law of motion, assuming the equilib-



(a) Three-dimensional element



(b) Two-dimensional element

Figure 3.1. Element subject to stress and body forces [133]

rium of forces, we have

$$\Sigma F_{Sx} = 0, \Sigma F_{Sy} = 0, \Sigma F_{Sz} = 0 \quad (3.2)$$

Taking moments of the x-, y-, and z-directed forces about point Q, for rotational equilibrium, we have:

$$\Sigma M_z = 0 \quad (3.3)$$

which results in:

$$(-\tau_{xy} dy dz) dx + (\tau_{yx} dx dz) dy = 0 \quad (3.4)$$

The above reduces to:

$$\tau_{xy} = \tau_{yx} \quad (3.5)$$

Similarly considering  $\Sigma M_y = 0$  and  $\Sigma M_x = 0$ , it can be shown that

$$\tau_{xz} = \tau_{zx} \quad (3.6a)$$

$$\tau_{yz} = \tau_{zy} \quad (3.6b)$$

For simplicity, the equilibrium equation will be derived in a two-dimensional plane, and the result will be generalized into 3D. A two-dimensional presentation of plane stress is depicted in Figure 3.1b with a thin element of sides  $dx$  and  $dy$ , with stresses  $\sigma_x$ ,  $\sigma_y$ ,  $\tau_{xy}$ , and

$\tau_{yx}$  acting in the x- and y-axis. The rate of change of stress acting on the right-hand side of the element can be expressed by truncated Taylor's expansion; thus for the stress acting upon x plane we have:

$$\sigma_x + \frac{\partial \sigma_x}{\partial x} dx \quad (3.7a)$$

$$\tau_{xy} + \frac{\partial \tau_{xy}}{\partial x} dx \quad (3.7b)$$

From the equilibrium of x forces,  $\Sigma F_x = 0$ , we have

$$\left( \sigma_x + \frac{\partial \sigma_x}{\partial x} dx \right) dy - \sigma_x dy + \left( \tau_{xy} + \frac{\partial \tau_{xy}}{\partial y} dy \right) dx - \tau_{xy} dx + F_x dx dy = 0 \quad (3.8)$$

The equation above can be simplified to:

$$\left( \frac{\partial \sigma_x}{\partial x} + \frac{\partial \tau_{xy}}{\partial y} + F_x \right) dx dy = 0 \quad (3.9)$$

As the  $dx dy$  is nonzero, the quantity in the parentheses has to equate to zero. The x and y equations result in the differential equations of equilibrium for two-dimensional stress as follows:

$$\frac{\partial \sigma_x}{\partial x} + \frac{\partial \tau_{xy}}{\partial y} + F_x = 0 \quad (3.10a)$$

$$\frac{\partial \sigma_y}{\partial y} + \frac{\partial \tau_{xy}}{\partial x} + F_y = 0 \quad (3.10b)$$

The differential equations of equilibrium for the case of three-dimensional stress can be summarized from the preceding expressions as:

$$\frac{\partial \sigma_x}{\partial x} + \frac{\partial \tau_{xy}}{\partial y} + \frac{\partial \tau_{xz}}{\partial z} + F_x = 0 \quad (3.11a)$$

$$\frac{\partial \tau_{xy}}{\partial x} + \frac{\partial \sigma_y}{\partial y} + \frac{\partial \tau_{yz}}{\partial z} + F_y = 0 \quad (3.11b)$$

$$\frac{\partial \tau_{xz}}{\partial x} + \frac{\partial \tau_{yz}}{\partial y} + \frac{\partial \sigma_z}{\partial z} + F_z = 0 \quad (3.11c)$$

The expression can be written more compactly using the Cartesian tensor notation:

$$\frac{\partial \sigma_{ij}}{\partial x_j} + f_i = 0 \quad (3.12)$$

Differential equations of motion for the three-dimensional stress may be derived from the



preceding equations as follows:

$$\rho_S \frac{\partial^2 u}{\partial t^2} + \frac{\partial \sigma_x}{\partial x} + \frac{\partial \tau_{xy}}{\partial y} + \frac{\partial \tau_{xz}}{\partial z} + F_x = 0 \quad (3.13a)$$

$$\rho_S \frac{\partial^2 v}{\partial t^2} + \frac{\partial \tau_{xy}}{\partial x} + \frac{\partial \sigma_y}{\partial y} + \frac{\partial \tau_{yz}}{\partial z} + F_y = 0 \quad (3.13b)$$

$$\rho_S \frac{\partial^2 w}{\partial t^2} + \frac{\partial \tau_{xz}}{\partial x} + \frac{\partial \tau_{yz}}{\partial y} + \frac{\partial \sigma_z}{\partial z} + F_z = 0 \quad (3.13c)$$

Where the second derivative of the displacement in the x-direction  $u$ , with respect to time, multiplied by the material density  $\rho_S$  represents the inertia, force depending on the acceleration of a body. Finally, a succinct representation of these expressions is derived in Equation 3.14:

$$\rho_S \frac{\partial^2 u_i}{\partial t^2} + \frac{\partial \sigma_{ij}}{\partial x_j} + f_i = 0 \quad (3.14)$$

### 3.3 The Linear-Elastic Constitutive Relations

#### 3.3.1 Strain-displacement relations

Considering deformations caused by external forces, one needs to introduce a measure of deformations intensity called strain. The total deformation can be regarded as a change in length and relative rotation without accompanying changes in length. Possible deformations of an element are illustrated in Figure 3.2.

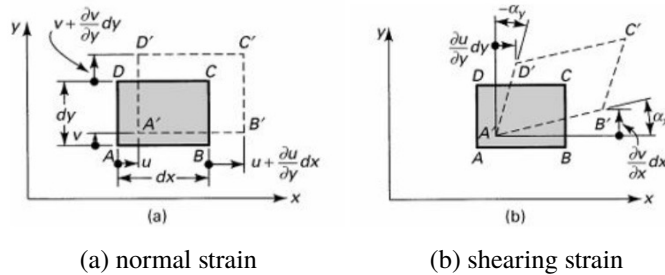


Figure 3.2. Total deformation of an element. [133]

Two normal or longitudinal strains are defined as:

$$\epsilon_x = \frac{\partial u}{\partial x}, \quad \epsilon_y = \frac{\partial v}{\partial y} \quad (3.15)$$

The positive sign is applied to elongation. If the element is subjected to contraction, a negative sign must appear.

Assuming small-angle  $\alpha_x$  between  $AB$  and  $A'B'$ , the shearing strain can be defined as:

$$\gamma_x = \alpha_x - \alpha_y = \frac{\partial u}{\partial y} + \frac{\partial v}{\partial x} \quad (3.16)$$

In the case of the 3D element, normal and shearing strains will be:

$$\epsilon_x = \frac{\partial u}{\partial x}, \quad \epsilon_y = \frac{\partial v}{\partial y}, \quad \epsilon_z = \frac{\partial w}{\partial z} \quad (3.17a)$$

$$\gamma_{xy} = \frac{\partial u}{\partial y} + \frac{\partial v}{\partial x}, \quad \gamma_{yz} = \frac{\partial v}{\partial z} + \frac{\partial w}{\partial y}, \quad \gamma_{zx} = \frac{\partial w}{\partial x} + \frac{\partial u}{\partial z} \quad (3.17b)$$

Then the state of strain at a point is described by a nine-term matrix:

$$[\epsilon_{ij}] = \begin{bmatrix} \epsilon_x & \frac{1}{2}\gamma_{xy} & \frac{1}{2}\gamma_{xz} \\ \frac{1}{2}\gamma_{yx} & \epsilon_y & \frac{1}{2}\gamma_{yz} \\ \frac{1}{2}\gamma_{zx} & \frac{1}{2}\gamma_{zy} & \epsilon_z \end{bmatrix} \quad (3.18)$$

In indicial notation:

$$\epsilon_{ij} = \frac{1}{2}(u_{i,j} + u_{j,i}) \quad (3.19)$$

This summarizes the strain-displacement relations of continuum mechanics.

### 3.3.2 Stress-strain relation

It has been proven experimentally that stress is directly proportional to strain in the linearly elastic range. This relationship is known as Hooke's Law. For an isotropic material, the stress-strain relationship can be written:

$$\begin{bmatrix} \sigma_x \\ \sigma_y \\ \sigma_z \\ \tau_{xy} \\ \tau_{xz} \\ \tau_{yz} \end{bmatrix} = \begin{bmatrix} \lambda + 2\mu & \lambda & \lambda & 0 & 0 & 0 \\ \lambda & \lambda + 2\mu & \lambda & 0 & 0 & 0 \\ \lambda & \lambda & \lambda + 2\mu & 0 & 0 & 0 \\ 0 & 0 & 0 & 2\mu & 0 & 0 \\ 0 & 0 & 0 & 0 & 2\mu & 0 \\ 0 & 0 & 0 & 0 & 0 & 2\mu \end{bmatrix} \begin{bmatrix} \epsilon_x \\ \epsilon_y \\ \epsilon_z \\ \gamma_{xy} \\ \gamma_{xz} \\ \gamma_{yz} \end{bmatrix} \quad (3.20)$$

Where shear modulus  $\mu$  and the quantity  $\lambda$  are called Lamé's constants, which are related to the elastic modulus,  $E$ , and the Poisson ratio,  $\nu$ , according to:

$$\lambda = \frac{\nu E}{(1 + \nu)(1 - 2\nu)} \quad (3.21)$$

$$\mu = \frac{E}{2(1 + \nu)} \quad (3.22)$$

This relation can also be written more conveniently in indicial form as:

$$\sigma_{ij} = 2\mu\epsilon_{ij} + \lambda\delta_{ij}\epsilon_{kk} \quad (3.23)$$

### 3.4 The Navier-Displacement Equations

It is now possible to combine the differential equations of the equilibrium 3.14, kinematic relations 3.19 and stress-strain relation 3.23.

First, consider the x-motion equation:

$$\rho_S \frac{\partial^2 u}{\partial t^2} + \frac{\partial \sigma_{xx}}{\partial x} + \frac{\partial \tau_{xy}}{\partial y} + \frac{\partial \tau_{xz}}{\partial z} + f_x = 0 \quad (3.24)$$

Then from the stress-strain equation (3.23), we can replace the stresses in the equation 3.24 above:

$$\sigma_{xx} = 2\mu\epsilon_{xx} + \lambda\epsilon_{kk} \quad (3.25a)$$

$$\epsilon_{kk} = \epsilon_{xx} + \epsilon_{yy} + \epsilon_{zz} \quad (3.25b)$$

$$\tau_{xy} = 2\mu\epsilon_{xy} \quad (3.25c)$$

$$\tau_{xz} = 2\mu\epsilon_{xz} \quad (3.25d)$$

Introducing strain-displacement equation 3.19 will give:

$$\sigma_{xx} = 2\mu \frac{\partial u}{\partial x} + \lambda \left( \frac{\partial u}{\partial x} + \frac{\partial v}{\partial y} + \frac{\partial w}{\partial z} \right) \quad (3.26a)$$

$$\tau_{xy} = \mu \left( \frac{\partial u}{\partial y} + \frac{\partial v}{\partial x} \right) \quad (3.26b)$$

$$\tau_{xz} = \mu \left( \frac{\partial u}{\partial z} + \frac{\partial w}{\partial x} \right) \quad (3.26c)$$

These can be then substituted back into the equilibrium equation 3.14, and summarized by writing them in Cartesian tensor notation:

$$\rho_S \frac{\partial^2 u_i}{\partial t^2} + (\lambda + \mu) \frac{\partial}{\partial x_i} \left( \frac{\partial u_j}{\partial x_j} \right) + \mu \frac{\partial^2 u_i}{\partial x_j^2} + f_i = 0 \quad (3.27)$$

This summarizes the governing equation for the solid linear-elastic displacements.

### 3.5 Large strains

As discussed in Section 3.1 further numerical approach towards assessing FIV will consider only the small deformations and deflections. However, for the validation of the FSI

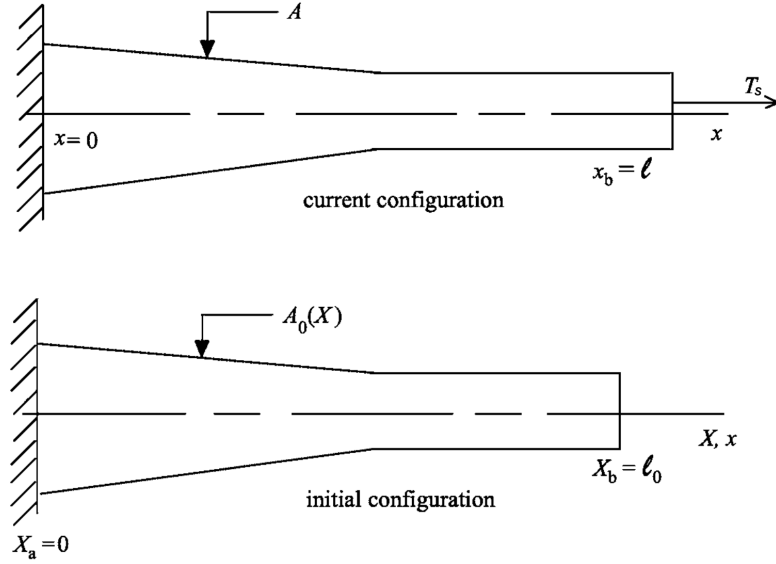


Figure 3.3. One-dimensional rod loaded at the right end in initial configuration (bottom) and deformed (current) configuration (top) [6]

methodology presented in Section 8.2, the assumptions of small strains and small rotations were no longer valid. For non-linear deformation, models adopt a total Lagrangian approach. In the total Lagrangian approach, the discrete equations are formulated with regard to the reference configuration. Figure 3.3 shows the starting (undeformed) configuration and reference configuration of the body during motion. The spatial (Eulerian) coordinate is denoted by  $x$ , and the material (Lagrangian) coordinates are denoted by  $X$ .

Assume that the stress in the cross-section is constant and that the total force across a given section is indicated by  $T_S$ . Cauchy stress is given by:

$$\sigma = \frac{T_S}{A} \quad (3.28)$$

here  $A$  refers to the current area  $A$  of the rod.

The nominal stress will be used in the total Lagrangian formulation. The nominal stress, indicated by  $P_S$ , is given by

$$P_S = \frac{T_S}{A_0} \quad (3.29)$$

Here the force is divided by the initial or undeformed area  $A_0$ . From Equations 3.28 ,3.29, it is apparent that physical and nominal stresses are related by:

$$\sigma = \frac{A_0}{A} P_S \quad (3.30)$$

$$P_S = \frac{A}{A_0} \sigma \quad (3.31)$$

The governing equation for total Lagrangian description of the linear momentum conservation law reads as:

$$\frac{\partial P_{Sij}}{\partial X_j} + \rho_0 b_i = \rho_0 \ddot{u}_j \quad (3.32)$$

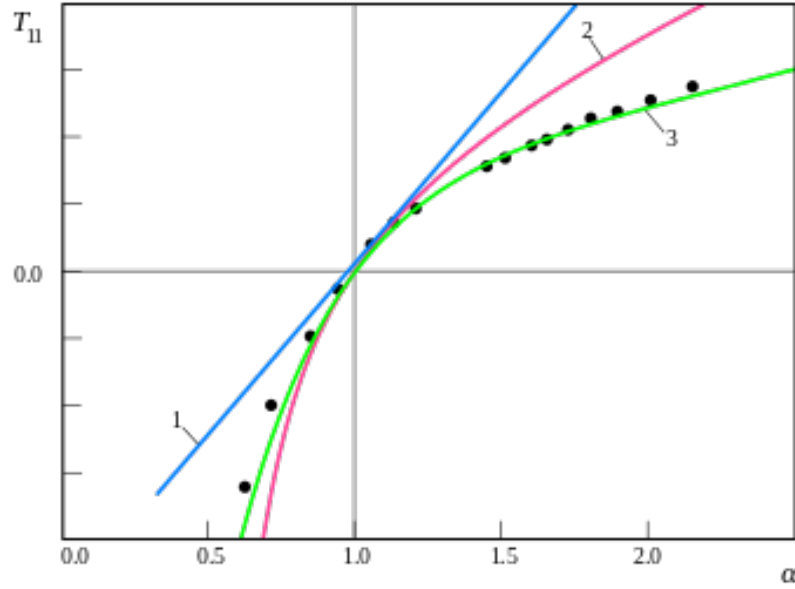


Figure 3.4. The stress-strain relationship for elastic (1) and hyperelastic material (2,3) [91]

Here  $b$  is the body force and  $\ddot{u}_j$  denotes solid displacement time derivative  $\partial^2 u(X, t) / \partial t^2$ ,  $\rho_0$  is the initial density. Constitutive relations defining the Cauchy (true) stress  $\sigma$  for non-linear geometry implemented within the OpenFOAM FSI solver are available in [16]. The next section will provide the constitutive relations for the Neo-Hookean material model used in simulations in Section 8.2).

### 3.6 Constitutive Relations: Hyperelastic materials

A neo-Hookean model is an extension of Hooke's law, applicable for large deformations. The stress-strain curve is depicted in Figure 3.4 where a comparison between linear elastic materials and a hyper-elastic material is presented. For materials such as rubber, the strain-stress relationship is non-linear. The stress-strain curve of a neo-Hookean material is initially linear, but the curve plateaus beyond a certain point, indicating the ability to resist severe elastic deformations that can be recovered.

Hyperelastic material models describe the behaviour of materials subjected to large elastic deformations under loading, returning to their original shape when the load is removed. A material which can undergo changes in volume is said to be compressible. In this section, constitutive equations to characterize the compressible hyperelastic materials are introduced.

As explained in Section 3.5, the applied load displaces the solid structure from the initial configuration to the deformed configuration. Assuming that the position of a material point in the undeformed configuration is  $\mathbf{X}$  and the displacement of this point to the deformed configuration is  $\mathbf{u}(\mathbf{X}, t)$ , the position of the material point in the deformed configuration can be described as:

$$x(\mathbf{X}, t) = \mathbf{X} + \mathbf{u}(\mathbf{X}, t) \quad (3.33)$$

The displacement  $\mathbf{u}$  can be expressed as:

$$\mathbf{u} = \begin{pmatrix} u_x & u_y & u_z \end{pmatrix}^T \quad (3.34)$$

The displacement field of a deformed body is defined by the deformation gradient tensor  $\mathbf{F}$ . It is a measure of how the deformation changes from point to point:

$$\mathbf{F} = \frac{\partial \mathbf{x}}{\partial \mathbf{X}} = \mathbf{I} + \frac{\partial \mathbf{u}}{\partial \mathbf{X}} = \mathbf{I} + \begin{pmatrix} \frac{\partial u_x}{\partial X} & \frac{\partial u_x}{\partial Y} & \frac{\partial u_x}{\partial Z} \\ \frac{\partial u_y}{\partial X} & \frac{\partial u_y}{\partial Y} & \frac{\partial u_y}{\partial Z} \\ \frac{\partial u_z}{\partial X} & \frac{\partial u_z}{\partial Y} & \frac{\partial u_z}{\partial Z} \end{pmatrix} \quad (3.35)$$

where  $\mathbf{I}$  is the identity matrix, the material position vector  $\mathbf{X}$  is defined by  $X$ ,  $Y$ , and  $Z$  coordinates.

It is possible to compute a measure of the deformation, independent of the rotation, without knowing the rotation matrix. The right Cauchy Green strain tensor defines the corresponding strain measure as:

$$\mathbf{C} = \mathbf{F}^T \mathbf{F} \quad (3.36)$$

The strain in undeformed configuration is defined with a Green-Lagrange strain tensor:

$$\mathbf{E} = \frac{1}{2}(\mathbf{F}^T \mathbf{F} - \mathbf{I}) \quad (3.37)$$

Instead of dealing directly with the deformation gradient  $\mathbf{F}$  and the corresponding strain measure  $\mathbf{C}$ , the approach is to decompose the  $\mathbf{F}$  into volume changing part and volume preserving part [61]:

$$\mathbf{F} = (J^{1/3} \mathbf{I}) \bar{\mathbf{F}} = J^{1/3} \bar{\mathbf{F}} \quad (3.38)$$

$$\mathbf{C} = (J^{2/3} \mathbf{I}) \bar{\mathbf{F}} = J^{2/3} \bar{\mathbf{C}} \quad (3.39)$$

Here  $J = \det[\mathbf{F}]$  is the Jacobian of the deformation gradient, and  $\det[\cdot]$  is the determinant operator. Terms  $J^{1/3} \mathbf{I}$  and  $J^{2/3} \mathbf{I}$  are related to volume changing deformations, while  $\bar{\mathbf{F}}$  and  $\bar{\mathbf{C}} = \bar{\mathbf{F}}^T \bar{\mathbf{F}}$  are related to volume-preserving deformations.  $\bar{\mathbf{F}}$  and  $\bar{\mathbf{C}}$  are called the modified deformation gradient and the modified right Cauchy stress tensor, respectively.

For hyperelastic materials, the strain-stress relationship is expressed in terms of a strain energy density function,  $\Psi = \Psi(\mathbf{F})$ . The strain energy function relates the deformation gradient to the amount of stored energy. For example, the stretched rubber band has a certain amount of energy stored. After a translation or rotation of the rubber band in space, the amount of the energy stored remains unchanged. Strain energy function  $\Psi$  can be expressed as a function of symmetric material tensors  $\mathbf{C}$  and  $\mathbf{E}$  as:

$$\Psi(\mathbf{F}) = \Psi(\mathbf{C}) = \Psi(\mathbf{E}) \quad (3.40)$$

The constitutive relation relates the Cauchy stress tensor  $\sigma = \sigma(x, t)$  at each place  $x = (\mathbf{X}, t)$  to the deformation gradient  $\mathbf{F}$ . The constitutive relation has a general form of:

$$\sigma(\mathbf{x}, t) = g(\mathbf{F}(\mathbf{X}, t), \mathbf{X}) = J^{-1} \frac{\partial \Psi(\mathbf{F})}{\partial \mathbf{F}} \mathbf{F}^T = J^{-1} \mathbf{F} \left( \frac{\partial \Psi(\mathbf{F})}{\partial \mathbf{F}} \right)^T \quad (3.41)$$

where  $\mathbf{g}$  represents the material properties and it is a tensor-valued function of one tensor variable  $\mathbf{F}$ . The gradient of the scalar-valued function  $\Psi$  is determined by its derivative with respect to the tensor variable  $\mathbf{F}$ . An alternative form of constitutive relation introduces the Piola transformation relating stress field  $\mathbf{S}$  and Cauchy stress  $\sigma$ . The general strain-stress relationship can be expressed as:

$$\mathbf{S} = 2 \frac{\partial \Psi}{\partial \mathbf{C}} \quad (3.42)$$

where  $\mathbf{S}$  is the second Piola-Kirchhoff stress defined as:

$$\mathbf{S} = J \mathbf{F}^{-1} \sigma \mathbf{F}^{-T} \quad (3.43)$$

where  $\sigma$  is the Cauchy stress.

The stored energy function,  $\Psi$  for a compressible neo-Hookean material is defined as [61]:

$$\Psi(I_1, J) = \frac{c_1}{\beta} (J^{-2\beta} - 1) + c_1 (I_1 - 3) \quad (3.44)$$

$$\beta = \frac{v}{1 - 2v} \quad (3.45)$$

Where the constants  $c_1 = \mu/2$  and  $\beta$  are related to the material parameters, shear modulus  $\mu$  and Poisson's ratio  $v$ .  $I_1$  is the first strain invariant of modified right Cauchy stress tensor  $\bar{\mathbf{C}}$ , defined as:

$$I_1 = \text{tr}[\bar{\mathbf{C}}] \quad (3.46)$$

Here the trace operator is indicated by  $\text{tr}[\cdot]$  and  $\bar{\mathbf{C}} = J^{-2/3} \mathbf{C}$ .

The following summarizes the neo-Hookean material model suitable for compressible or nearly incompressible materials. Several strain-energy formulations are suitable for describing different hyperelastic material systems. Their detailed description is provided in [6, 55, 61]. Further discussion on the solid constitutive laws for non-linear geometry lies outside of the scope of this thesis.

### 3.7 Summary

This chapter summarizes the governing equations of linear elastic deformation in terms of displacement. The mathematical models are discretized using the cell-centred finite volume method. The discretization of the presented mathematical model will be described in Chapter 7. What follows is a description of mathematical models governing the fluid flow.

# Chapter 4

## Turbulence modelling

When the inertial forces dominate the viscous forces, the flow becomes turbulent. In statistically steady turbulent flows, every transported quantity, such as velocity, pressure, temperature, and species concentration, fluctuates around a mean value. Most engineering flows are turbulent. Hence there is a necessity for modelling turbulence. This Chapter focuses on this most widely turbulence modelling approach used for industrial flows. The first part of this Chapter is devoted to a brief introduction of fundamental concepts and definitions related to turbulent flows. The second part of the Chapter provides an overview of two-equation models and more complex Reynolds stress models. Finally, the comparison of effectiveness between the two approaches is presented.

### 4.1 Fundamental Concepts

#### 4.1.1 Eddy scales

Turbulence is an unsteady phenomenon, and it is inherently three-dimensional. The flow consists of a spectrum of different scales: eddy sizes. Figure 4.1 illustrates the cross-sectional image of a turbulent boundary layer on a flat plate. Turbulent flow visualizations exhibit the rotational flow structures with lengths equivalent to the flow boundaries, together with intermediate and small length scales. The structures are known as *turbulent eddies*. The largest eddies are of the size of the flow. The growth of the large-scale eddies is primarily governed by inertia and pressure; therefore, the structure of the largest eddies is anisotropic. Small scale eddies are of 0.1 to 0.01mm and frequencies around 10kHz. They appear to be more organized, have a similar structure in all turbulent flows, and are dominated by viscous effects. The small-scale eddies are isotropic [135].

The kinetic energy contained in the large eddies is extracted from the mean flow kinetic energy through the interaction between the large-scale eddies and the mean shear. It is subsequently transmitted to smaller scale eddies through eddy break-up. The *cascade process* is the transfer of energy from larger eddies to the smaller and smaller eddies. The process continues until the level of the smallest eddies, at which the viscous stresses become large, and the kinetic energy is dissipated into heat. These eddies are of the smallest scales present in the turbulent flow and are called Kolmogorov scales.



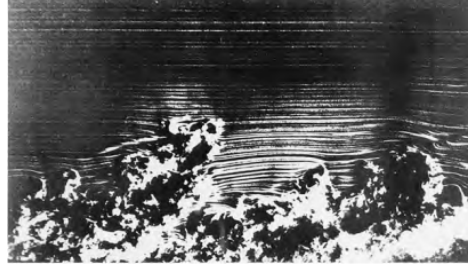


Figure 4.1. Side view of a turbulent boundary layer visualized by smoke traces [135]

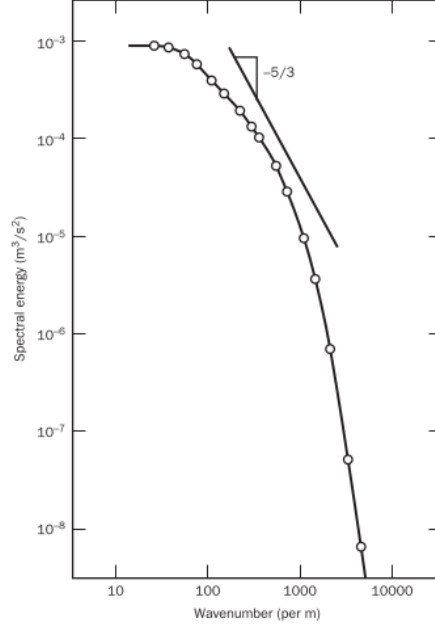


Figure 4.2. The *energy spectrum* of a turbulence behind a grid [135]

Turbulent eddy distribution as a function of eddy size is represented in the Kolmogorov energy spectrum. The spectral energy  $E(\kappa)$  as a function of the wavenumber  $\kappa$  is presented in Figure 4.2. Wave-number  $\kappa$  is defined as  $\kappa = 2\pi/\lambda$ , where  $\lambda$  is the wavelength of the eddies. The diagram shows that the energy peaks at the low wave numbers, hence large eddies concentrate most of the energy fluctuations. The smallest eddies have the lowest energy content.

Small-scale eddy motion is determined by viscosity and dissipation. The amount of dissipated energy per unit time is denoted as  $\varepsilon$ , which is the energy per unit time and unit mass  $\varepsilon = [m^2/s^3]$ . The larger the velocity gradient, the more energy is transferred from large-scale to small-scale eddies. Kinetic energy is converted to thermal energy by the viscous forces, hence larger viscosity,  $\nu$ , implies larger dissipative scales. Using dimensional analysis one can establish the Kolmogorov velocity scale,  $v_n$ , length scale  $l_n$  and time scale  $\tau_n$  :

$$v_n = (\nu\varepsilon)^{1/4} \quad (4.1a)$$

$$l_n = \left( \frac{\nu^3}{\varepsilon} \right)^{1/4} \quad (4.1b)$$

$$\tau_n = \left(\frac{\nu}{\varepsilon}\right)^{1/2} \quad (4.1c)$$

The rate of production of the turbulent energy has to be in balance with the energy dissipation. The large eddy scales are denoted as length  $l$ , velocity  $\vartheta$ , and time  $T = l/\vartheta$ . The energy transfer rate from large-energy-containing eddies is expected to scale as follows:

$$\varepsilon \sim \frac{\vartheta^2}{T} \sim \frac{\vartheta^2}{l/\vartheta} \sim \frac{\vartheta^3}{l} \quad (4.2)$$

The expression can be combined with the Equations 4.1 giving the ratios of the small length scales to the large length scales:

$$\frac{v_n}{\vartheta} = Re^{-1/4} \quad (4.3a)$$

$$\frac{l_n}{l} = Re^{-3/4} \quad (4.3b)$$

$$\frac{\tau_n}{T} = Re^{-1/2} \quad (4.3c)$$

When the flow Reynolds number increases, the ratio of velocity, length and time scales of large eddies to the Kolmogorov eddies increases. This implies that the wavenumber range between large eddies and small-scale eddies is getting wider. Increasing the Reynolds number results in a finer turbulence structure, the size of smaller scales goes down, and their frequency goes up. On the other hand, the scale of the mean flow determines the size of the larger scales.

## 4.2 Navier-Stokes Equations

The purpose of this section is to present set of equations collectively known as the Navier-Stokes equations. In fluid dynamics, fluid motion is described by the conservation of mass and the conservation of momentum.

### 4.2.1 Continuity Equation

The continuity equation can be written in Cartesian tensor notation as:

$$\frac{\partial \rho_F}{\partial t} + \frac{\partial (\rho_F \tilde{U}_i)}{\partial x_i} = 0 \quad (4.4)$$

where  $\rho_F$  is the fluid density and  $\tilde{U}_i$  is the instantaneous fluid velocity in the  $x_i$  direction. In the case of incompressible fluid, the density is constant. In steady-state flows  $\frac{\delta \rho_F}{\delta t} = 0$ , thus:

$$\frac{\partial(\tilde{U}_i)}{\partial x_i} = 0 \quad (4.5)$$

#### 4.2.2 Momentum

The momentum equation is obtained from applying the force-momentum principle:

$$\frac{\partial(\rho_F \tilde{U}_i)}{\partial t} + \frac{\partial(\rho_F \tilde{U}_i \tilde{U}_j)}{\partial x_j} = -\frac{\partial \tilde{P}}{\partial x_j} + \frac{\partial \tau_{ij}}{\partial x_j} + \tilde{F}_i \quad (4.6)$$

Where  $\tau_{ij}$  is the viscous shear stress tensor,  $\tilde{P}$  is the instantaneous pressure and  $\tilde{F}_i$  represent the additional instantaneous body forces. In Newtonian fluids stress-strain relation can be expressed as the viscous stresses being linearly related to the mean strain rates. The constant of proportionality is the fluid property, viscosity  $\mu_F$ :

$$\tau_{ij} = \mu_F \left( \frac{\partial \tilde{U}_i}{\partial x_j} + \frac{\partial \tilde{U}_j}{\partial x_i} \right) \quad (4.7)$$

Substitution of stress-strain relation to the governing equation gives the momentum equation for the incompressible flow:

$$\frac{\partial \rho_F \tilde{U}_i}{\partial t} + \frac{\partial \rho_F \tilde{U}_i \tilde{U}_j}{\partial x_j} = -\frac{\partial P}{\partial x_i} + \frac{\partial}{\partial x_j} \left[ \mu_F \left( \frac{\partial \tilde{U}_i}{\partial x_j} + \frac{\partial \tilde{U}_j}{\partial x_i} \right) \right] + \tilde{F}_i \quad (4.8)$$

This summarizes the equations governing the unsteady flow of an incompressible fluid. In the case of isothermal flow, it is not necessary to solve the energy equation in addition to equations described above.

### 4.3 RANS Modelling

The Reynolds Averaged Navier-Stokes (RANS) method develops transport equations for the mean flow field with models to account for the mixing effects of turbulence. The objective is to develop equations that predict time-averaged velocity, pressure and temperature fields without calculating the complete turbulent flow pattern as a function of time.

As originally proposed by Reynolds (1895), the instantaneous variables (velocity, pressure, temperature etc.) can be decomposed into a mean (or average) and a fluctuating part. The

RANS equations are primarily used to model turbulent flows:

$$\tilde{\Phi}(x_i, t) = \bar{\Phi}(x_i) + \phi(x_i, t) \quad (4.9)$$

Here  $\tilde{\Phi}$  is the instantaneous value of a scalar variable,  $\bar{\Phi}$  is the mean component, and  $\phi$  is the fluctuating component of the variable. For a steady flow field, the mean component can be defined with the time average of a fluctuating quantity over a time interval  $\delta t$ :

$$\bar{\Phi}(x_i) = \frac{1}{\Delta t} \int_{t_0}^{t_0 + \Delta t} \phi(x_i, t) dt \quad (4.10)$$

For steady flow, the time-averaged mean value is constant. For unsteady flow, the mean value is a function of time, and it is defined with the ensemble averaging. Ensemble average is an average of the instantaneous values of the property at a given point in time and space over a large number of repeated identical experiments:

$$\Phi(x_i, t) = \lim_{N \rightarrow \infty} \frac{1}{N} \sum_{n=1}^N \tilde{\Phi}(x_i, t) \quad (4.11)$$

Where  $N$  is the number of samples. The instantaneous values in the Navier-Stokes equations are replaced by time-averaged mean and fluctuating values, and then the entire equation is time-averaged. The resulting equations are the Reynolds Averaged Navier-Stokes equations (RANS). The RANS form of the continuity equation will be:

$$\frac{\partial U_i}{\partial x_i} = 0 \quad (4.12)$$

Where  $U_i$  represents the mean fluid velocity in the  $x_i$  direction. The RANS form of the momentum equation then becomes:

$$\frac{\partial(\rho_F U_i)}{\partial t} + \frac{\partial(\rho_F U_i U_j)}{\partial x_j} = -\frac{\partial P}{\partial x_i} + \frac{\partial}{\partial x_j} \left[ \mu_F \left( \frac{\partial U_i}{\partial x_j} + \frac{\partial U_j}{\partial x_i} \right) - \rho_F \overline{u_i u_j} \right] + F_i \quad (4.13)$$

As a result of the modification of the original Navier-Stokes system, additional unknowns appear to include the effect of turbulence, namely the Reynolds stresses  $\overline{u_i u_j}$ . These are six additional, non-zero stresses, three normal stresses and three shear stresses. In order to solve the system, supplementary turbulence models must be introduced. The most common CFD turbulence models may be divided into four main categories depending on the number of additional transport equations involved along with the RANS flow equations. The classification most common RANS turbulence models are conveniently summarized in Table 4.1.

Table 4.1. Standard RANS turbulence models [135]

N. of extra transport equations	Name
Zero	Mixing length model
One	Spalart-Allmaras model
Two	$k - \varepsilon$ model
Two	$k - \omega$ model
Seven	Reynolds stress model

## 4.4 Eddy Viscosity Models

Within this class of model, the assumption is that the turbulent shear stresses  $\overline{u_i u_j}$  simply act as additional stresses on top of the viscous stresses,  $\nu \left( \frac{\partial U_i}{\partial x_j} + \frac{\partial U_j}{\partial x_i} \right)$ . The viscous stresses are proportional to the rate of deformation of fluid elements, Equation 4.7. In order to express the turbulent shear stress in a similar form, the concept of 'eddy viscosity'.  $\nu_t$  (proposed by Boussinesq -1877) will be introduced. According to the Boussinesq assumption, the turbulent stress tensor is linearly related to the mean strain rate tensor through:

$$\rho_F \overline{u_i u_j} = -\mu_t \left( \frac{\partial U_i}{\partial x_j} + \frac{\partial U_j}{\partial x_i} \right) + 2/3 k \delta_{ij} \quad (4.14)$$

Where  $\mu_t$  is referred to as the turbulent viscosity, and it is a property of the flow and  $\delta_{ij}$  is the Kronecker delta which is defined as:

$$\delta_{ij} = \begin{cases} 1, & \text{if } i=j \\ 0, & \text{if } i \neq j \end{cases}$$

The quantity  $k$  is the turbulent kinetic energy, defined as:

$$k = 1/2(\overline{u_1^2} + \overline{u_2^2} + \overline{u_3^2}) \quad (4.15)$$

If the eddy-viscosity model is adopted, the remaining modelling problem is to choose the method of obtaining the turbulent viscosity.

The zero equation models are models in which the turbulent kinematic viscosity  $\nu_t$  is directly related to the turbulent velocity and length scale, without additional transport equations. The assumption in zero equation models is that the rate of production of turbulence properties equals their dissipation rate, and that is only applicable in simple two-dimensional flows with moderate flow direction changes. These models require small computational resources, but they have very limited applicability. They fall on predicting the flows with separation and recirculation because of the lack of diffusion and convection in turbulence transport equations [135].

The velocity scale in one-equation models is specified in terms of turbulent kinetic energy. One turbulent transport equation is solved in conjunction with auxiliary closure expressions

for the length scale. The model performs well only on simplified geometries because in complex geometries, it is difficult to specify the length scale [118].

Two-equations models use two transport equations: one for turbulent kinetic energy and one for its dissipation rate. Reynolds Stress Models directly calculate the Reynolds stress tensor components instead of adopting the eddy viscosity approach. The Reynolds Stress model solving additional seven transport equations and the most commonly used two-equations models will be described in the next sections.

## 4.5 The $k$ - $\varepsilon$ Two-Equation Model

In this commonly used two-equation model, two transport equations are solved for the turbulent kinetic energy  $k$  and for the rate of dissipation of turbulent energy  $\varepsilon$ , where  $\varepsilon$  is the product of kinematic viscosity and velocity gradient of the turbulent fluctuations, as shown in Equation 4.17. As the  $u'_i$  remains unknown, we solve transport equations for  $k$  and for  $\varepsilon$ . We expect the  $\varepsilon$  dissipation to be high near the walls.

$$k = 1/2(\overline{u'^2} + \overline{v'^2} + \overline{w'^2}) \quad (4.16)$$

$$\varepsilon = \nu \overline{\left( \frac{\partial u'_i}{\partial x_j} \right) \left( \frac{\partial u'_i}{\partial x_j} \right)} \quad (4.17)$$

The velocity scale  $\vartheta$  and the length scale  $l$  are related to the kinetic energy and dissipation rate by:

$$\vartheta = k^{1/2} \quad (4.18)$$

$$l = \frac{k^{3/2}}{\varepsilon} \quad (4.19)$$

The turbulent viscosity is modelled as:

$$\mu_t = \rho_F C_\mu \frac{k^2}{\varepsilon} \quad (4.20)$$

The standard  $k - \varepsilon$  model solves the following transport equations for turbulent kinetic energy and dissipation rate:

$$\frac{\partial(\rho_F k)}{\partial t} + \frac{\partial(\rho_F U_i k)}{\partial x_i} = \frac{\partial}{\partial x_j} \left[ \left( \mu_F + \frac{\mu_t}{\sigma_k} \right) \frac{\partial k}{\partial x_j} \right] + \frac{1}{2} \mu_t E_{ij} E_{ij} - \rho_F \varepsilon \quad (4.21a)$$

$$\frac{\partial(\rho_F \varepsilon)}{\partial t} + \frac{\partial(\rho_F U_i \varepsilon)}{\partial x_i} = \frac{\partial}{\partial x_j} \left[ \left( \mu_F + \frac{\mu_t}{\sigma_k} \right) \frac{\partial \varepsilon}{\partial x_i} \right] + C_{1\varepsilon} \frac{\varepsilon}{k} \frac{1}{2} \mu_t E_{ij} E_{ij} - C_{2\varepsilon} \rho_F \frac{\varepsilon^2}{k} \quad (4.21b)$$

Where  $E_{ij}$  is a strain tensor:

$$E_{ij} = \left( \frac{\partial U_i}{\partial x_j} + \frac{\partial U_j}{\partial x_i} \right) \quad (4.22)$$

Suitable model constants are provided by Launder & Sharma (1974):

$$c_\mu = 0.09, \sigma_k = 1.00, \sigma_\varepsilon = 1.00, C_{1\varepsilon} = 1.44, C_{2\varepsilon} = 1.92$$

In Equations 4.21a and 4.21b the first term on the left is the rate of change of  $k$  or  $\varepsilon$  and the second term on the left is the transport of  $k$  and  $\varepsilon$  by convection. The terms on the right side of these equations denote the transport of  $k$  and  $\varepsilon$  by diffusion, their rate of production and the rate of destruction by viscous action. The diffusion term is modelled with a gradient hypothesis to even out the inhomogeneities. The assumption implies that the diffusion term transports  $k$  from regions where  $k$  is large to the regions where  $k$  is small. The parameters  $\sigma_k, \sigma_\varepsilon$  are the turbulent Prandtl numbers for  $k$  and epsilon. The Reynolds stresses in the production term are computed using the Boussinesq assumption (Equation 4.14). The production and destruction are linked with the factor  $\frac{\varepsilon}{k}$ . As the ratio  $\frac{\varepsilon}{k}$  increases or decreases, the generation and destruction of  $\varepsilon$  adapt accordingly.

With the flow with high Re numbers, wall functions can be employed, which relate the wall shear stress to the mean velocity, turbulence kinetic energy  $k$  and rate of dissipation  $\varepsilon$ . This allows to avoid integration of the model equations right to the wall. At low Reynolds numbers, the log-law is not valid. The remedy is to apply a two-layer approach known as the low-Re formulation number  $k$ -epsilon model, with additional damping functions, so that the model coefficients  $C_{1\varepsilon}, C_{2\varepsilon}, c_{\mu_F}$  become damped. This allows accounting for viscous effects in the near-wall sublayer.

## 4.6 The $k$ - $\omega$ Two-Equation Model

The next example of a two-equation model is a  $k - \omega$  model developed by Wilcox (1988). The two-equation model includes a transport equation for  $k$ , and a second equation for the turbulent frequency or specific turbulence dissipation rate  $\omega$  (units  $s^{-1}$ ):

$$\omega = \frac{\varepsilon}{C_\mu k}; C_\mu = 0.09 \quad (4.23)$$

The eddy viscosity is determined from:

$$\mu_t = \rho_F \frac{k}{\omega} \quad (4.24)$$

The transport equation for the turbulent kinetic energy is given by:

$$\frac{\partial(\rho_F k)}{\partial t} + \frac{\partial(\rho_F U_i k)}{\partial x_i} = \frac{\partial}{\partial x_j} \left[ \left( \mu_F + \frac{\mu_t}{\sigma_k} \right) \frac{\partial k}{\partial x_j} \right] + P_k - \beta^* \rho_F k \omega^2 \quad (4.25)$$

The specific dissipation rate equation is governed by:

$$\frac{\partial(\rho_F \omega)}{\partial t} + \frac{\partial(\rho_F U_i \omega)}{\partial x_i} = \frac{\partial}{\partial x_j} \left[ \left( \mu_F + \frac{\mu_t}{\sigma_\omega} \right) \frac{\partial \omega}{\partial x_j} \right] + \frac{\alpha}{\omega} P_k - \beta \rho_F k \omega^2 \quad (4.26)$$

The  $k - \omega$  model has different empirical coefficients  $(\alpha, \beta, \beta^*, \sigma_k, \sigma_\omega)$ . The advantage of the model is that it does not require a wall damping function near the wall for low Reynolds number applications. The main weakness of the model is that it is sensitive to the freestream turbulence conditions. The eddy-viscosity  $\mu_t$  is indeterminate as the boundary condition of  $\omega$  equals 0, so a small non-zero value needs to be defined. The specification of the freestream value of  $\omega$  strongly influences the final results, which is especially undesirable in external aerodynamics applications.

#### 4.6.1 Menter $k-\omega$ SST model

The shear stress transport (SST) formulation combines the best features of the  $k - \varepsilon$  and  $k - \omega$  models. The baseline model (BST) is identical to the  $k - \omega$  model (Equations 4.25, 4.26) in the near wall region but uses a blending function to gradually transit to the  $k - \varepsilon$  in the fully turbulent region far from the wall. The coefficients in the  $k-\omega$  equations are as follows [2]:

$$C = F_1 C_{k-\omega} + (1 - F_1) C_{k-\varepsilon} \quad (4.27)$$

Where  $C_{k-\omega}$  are coefficients from the  $k - \omega$  model and  $C_{k-\varepsilon}$  from the high Reynolds  $k - \varepsilon$  model.  $F_1$  is the blending function such that near the wall  $F_1 = 1$ , what activates the  $k - \omega$  model and away from the wall  $F_1 = 0$ , what activates the  $k - \varepsilon$  model.  $F_1$  is defined as the function of the turbulence length scale  $k^{1/2}/\omega$ , then the turbulence Reynolds number, and the third term is included to prevent the solution dependency on the freestream. It is expressed as follows:

$$F_1 = F_1 \left( \frac{k^{1/2}/\omega}{y}, \frac{(v/\omega)^{1/2}}{y}, \frac{(k\omega/\nabla k \cdot \nabla \omega)^{1/2}}{y} \right) \quad (4.28)$$

It was experimentally found that in boundary layers with adverse pressure gradients, the production is significantly larger than the dissipation, and the Boussinesq assumption was over-predicting the wall shear stress. To improve the performance with flows with adverse pressure gradients and wake regions, the SST modelling approach involves using limiters on turbulent viscosity. When the turbulent kinetic energy production is large, the limiters on turbulent viscosity are activated. Otherwise, the limitation is not active when the pro-



duction  $\simeq$  dissipation. The turbulent viscosity is defined as:

$$\mu_t = \frac{a_1 \rho_F k}{\max(a_1 \omega, S F_2)} \quad (4.29)$$

Where  $a_1 = \text{constant}$ ,  $S = \sqrt{2E_{ij}E_{ij}}$  which comes from the production term using the Boussinesq assumption, and  $F_2$  is another blending function similar to  $F_1$ .

## 4.7 Reynolds Stress Models

In the Reynolds stress equation models (RSM), six transport equations for each Reynolds stress are solved in conjunction with the transport equation for the rate of dissipation of turbulent kinetic energy  $\varepsilon$ .

The exact Reynolds stress transport equations can be derived from the Navier-Stokes equations. This is done by subtracting the RANS momentum equation 4.13 from the instantaneous Navier-Stokes equations 4.8. After manipulations, one reaches the material derivative, the rate of change of Reynolds stress  $\overline{u_i u_j}$  and its transport by convection,  $C_{ij}$ :

$$\frac{D\overline{u_i u_j}}{Dt} = \frac{\partial \overline{u_i u_j}}{\partial t} + C_{ij} = \frac{\partial \overline{u_i u_j}}{\partial t} + U_k \frac{\partial \overline{u_i u_j}}{\partial x_k} = P_{ij} - \varepsilon_{ij} + \phi_{ij} + D_{ij} \quad (4.30)$$

The final exact equation for the Reynolds stresses transport equation can be symbolically represented as:

$$\frac{D\overline{u_i u_j}}{Dt} = P_{ij} - \varepsilon_{ij} + \phi_{ij} - D_{ij} \quad (4.31)$$

On the right hand side terms are denoted as follows: the rate production of  $\overline{u_i u_j}$ ,  $P_{ij}$ , rate of dissipation of  $\overline{u_i u_j}$ ,  $\varepsilon_{ij}$ , transport of the  $\overline{u_i u_j}$  among the different components of the stress tensor due to turbulent pressure strain interactions  $\phi_{ij}$  and rate of diffusion,  $D_{ij}$ . If additional body forces are present due, for example, to buoyancy or rotation, there are further contributions to the redistribution and production terms.

The convection and the production terms can be retained in their exact form because of the contributions only from the Reynolds stresses and mean velocity gradient.

The  $P_{ij}$  term represents the production of turbulent kinetic energy by the mean flow field. In the  $k - \varepsilon$  model the Reynolds stresses in the production term are computed using the Boussinesq assumption,  $2\mu_t E_{ij} E_{ij}$  in the equations 4.21a, 4.21b. In the RSM, the production term is solved exactly:

$$P_{ij} = - \left( \overline{u_j u_k} \frac{\partial U_i}{\partial x_k} + \overline{u_i u_k} \frac{\partial U_j}{\partial x_k} \right) \quad (4.32)$$

To solve Equation 4.31, the models for the diffusion, dissipation rate and the pressure-strain correlation are necessary. Since this project is strictly related to industrial applications, further review will concentrate on the approaches widely used in commercial CFD codes. These are the high Reynolds LRR by Launder et al. [81] and high Reynolds SSG by Speziale et al. [125].

The dissipation rate  $\varepsilon_{ij}$  represents the destruction of  $\overline{u_i u_j}$ , via the cascade process and vortex stretching. It is modelled by assuming isotropic dissipation of the small eddies. The dissipation rate of Reynolds stress is modelled as:

$$\varepsilon_{ij} = \frac{2}{3}\varepsilon\delta_{ij} \quad (4.33)$$

The  $\varepsilon$  in the equation below is the dissipation rate of turbulent kinetic energy defined in the equation 4.17.

The rate of diffusion  $D_{ij}$  is defined as:

$$D_{ij} = D_{ij,t} + D_{ij,\mu_F} = \frac{\partial}{\partial x_k} \left[ \overline{u_i u_j u_k} + \frac{\overline{p u_i}}{\rho_F} \delta_{jk} + \frac{\overline{p u_j}}{\rho_F} \delta_{ik} - \mu_F \frac{\partial \overline{u_i u_j}}{\partial x_k} \right] \quad (4.34)$$

where  $D_{ij,t}$  and  $D_{ij,\mu_F}$  represent the turbulent and viscous diffusion respectively. In the  $k - \varepsilon$  models it is defined with the gradient hypothesis in Equations 4.21a, 4.21b. The assumption is that the diffusion term transports  $k$  from regions with large  $k$  to regions where  $k$  is small. Inhomogeneities are evened out through diffusion:

$$D^\varepsilon = \frac{\partial}{\partial x_j} \left[ \left( \mu_F + \frac{\mu_t}{\sigma_k} \right) \frac{\partial \varepsilon}{\partial x_i} \right]$$

$$D^k = \frac{\partial}{\partial x_j} \left[ \left( \mu_F + \frac{\mu_t}{\sigma_k} \right) \frac{\partial k}{\partial x_i} \right]$$

In the RSM models, the diffusion flux of  $k$  can be modelled in a more advanced fashion. More general gradient diffusion hypothesis (GGDH) of [30] involves the contribution from the transport equation of triple correlation  $\overline{u_i u_j u_k}$ . The diffusive contribution of the pressure component of the diffusion term is usually negligible, and viscous terms do not require modelling. The diffusion terms for  $k$  and  $\varepsilon$  modelled with the use of GGDH can be written as:

$$D_{ij,t} = c_S \frac{\partial}{\partial x_k} \left( \frac{k}{\varepsilon} \overline{u_k u_l} \frac{\partial \overline{u_i u_j}}{\partial x_l} \right) \quad (4.35)$$

where  $c_S = 0.25$

The pressure-strain correlation  $\phi_{ij}$  acts as a sink term in the shear stress equation:

$$\phi_{ij} = \frac{p}{\rho_F} \left( \frac{\partial u_j}{\partial x_j} + \frac{\partial u_i}{\partial x_j} \right) \quad (4.36)$$

$\phi_{ij}$  is modelled by taking the effect of the 'slow' pressure strain term and 'rapid' process. The slow term makes the turbulence more isotropic by decreasing the large normal stresses and increasing the small normal stresses. The slow term  $\phi_{ij}^{(1)}$  is modelled to be proportional to the degree of anisotropy of Reynolds stresses  $a_{ij}$ :

$$\phi_{ij}^{(1)} = -c_1 \frac{\varepsilon}{k} a_{ij} = -c_1 \frac{\varepsilon}{k} \left( \overline{u_i u_j} - \frac{2}{3} k \delta_{ij} \right) \quad (4.37)$$

where  $c_1 = 1.8$ .

The rapid term takes into account the very strong velocity gradient that produces the eddies so that the slow term can be initially neglected. It is called rapid because the presence of the velocity gradient gives the rapid response to change in strain. The rate of the rapid processes is modelled as proportional to the production process that generates anisotropy,  $P_{ij}$

$$\phi_{ij}^{(2)} = -c_2 \left( P_{ij} - \frac{2}{3} P \delta_{ij} \right) \quad (4.38)$$

where  $c_2 = 0.6$ .

The simplest form of the pressure-strain term is

$$\phi_{ij} = \phi_{ij}^{(1)} + \phi_{ij}^{(2)} \quad (4.39)$$

Finally, additional corrections are applied to account for the wall proximity on the pressure-strain terms. Applyin the equation 4.39 will have an effect on reducing the anisotropy of the Reynolds stresses while ignoring the increase of anisotropy of normal Reynolds stresses near the wall.

In LLR, a *wall reflection* term of [52] is applied to account for damping of turbulence from the wall proximity. To account for the damping of turbulence, the term which depends on the distance from the wall,  $x_2$  and turbulent length scale,  $k^{3/2}/\varepsilon$  is applied- the damping effect of the wall decrease with an increasing distance. Additionally, the term accounting on the wall shear stress is introduced, using two additional corrections to  $\phi_{ij}$  with the unit normal vector  $n_i$ . A rigid wall impedes the transfer of energy from the streamwise direction to that normal to the wall. The final form of the near wall correction in the pressure-strain correlation for the slow term applied in the LRR model is:

$$\phi_{ij}^{(1)} = C_{1ref} \frac{\varepsilon}{k} \left( \overline{u_k u_m} n_k n_m \delta_{ij} - \frac{3}{2} \overline{u_k u_i} n_k n_j - \frac{3}{2} \overline{u_k u_j} n_k n_i \right) \kappa \frac{k^{3/2}}{\varepsilon x_2} \quad (4.40)$$

and the correction of the rapid part reads as:

$$\phi_{ij}^{(2)} = C_{2ref} \left( \phi_{km}^{(2)} n_k n_m \delta_{ij} - \frac{3}{2} \phi_{ik}^{(2)} n_k n_j - \frac{3}{2} \phi_{jk}^{(2)} n_k n_i \right) \kappa \frac{k^{3/2}}{\varepsilon x_2} \quad (4.41)$$

where  $C_{1ref} = 0.5$ ,  $C_{2ref} = 0.3$  and  $\kappa = 0.41$ .

The pressure strain in the SSG model does not explicitly include wall-reflection terms. Instead, the most general form of  $\phi_{ij}$  from equation 4.39, is linear in mean strain and rotation tensors that vary quadratically with the stress anisotropy tensor  $a_{ij}$ . The  $a_{ij}$  is defined as:

$$a_{ij} = \frac{\overline{u_i u_j}}{k} - \frac{2}{3} \delta_{ij} \quad (4.42)$$

The final version of this model has a rapid part with a linear function of  $a_{ij}$  (equation 4.37) and a quadratically non-linear function in the slow part.

In the SSG model, the pressure-strain takes the following form:

$$\begin{aligned} \phi_{ij} = & -(C_1 \varepsilon + C_1^* P_k) a_{ij} + C_2 \varepsilon (a_{ik} a_{kj} - \frac{1}{3} a_{lm} a_{lm} \delta_{ij}) + (C_3 - C_3^* A_2) k S_{ij} + \\ & C_4 k (a_{ik} S_{jk} + a_{jk} S_{ik} - \frac{2}{3} a_{lm} S_{lm} \delta_{ij}) + C_5 k (a_{ik} \Omega_{jk} + a_{jk} \Omega_{ik}) \end{aligned} \quad (4.43)$$

where  $\Omega_{ij}$  is the mean vorticity tensor equal  $\frac{1}{2} \left( \frac{\partial U_i}{\partial x_j} - \frac{\partial U_j}{\partial x_i} \right)$ , and  $C_{1-5}$  are the constants calibrated for the model.

## 4.8 Reynolds stress models vs. eddy viscosity models

As shown in previous sections, the Reynolds Stress models (RSM) treat the production term exactly, while it has to be modelled in the Eddy Viscosity models (EVM). Figure 4.3a illustrates a streamlined curvature and rotation situation when the flow approaches a separation region or an obstacle. Until the streamlines are parallel to the wall, production will result from primary shear  $\frac{\partial U_1}{\partial x_2}$ . Whenever the streamline gets deflected, there is a shear due to the  $\frac{\partial U_2}{\partial x_1}$  and production term  $P_{12}$  will read as:

$$RSM : P_{12} = -\overline{u_2^2} \frac{\partial U_1}{\partial x_2} - \overline{u_1^2} \frac{\partial U_2}{\partial x_1} \quad (4.44)$$

The magnitude of  $P_{12}$  will increase as the  $\frac{\partial U_2}{\partial x_1} > 0$ . Two rotational strains,  $\frac{\partial U_1}{\partial x_2}$  and  $\frac{\partial U_2}{\partial x_1}$  on concave wall have the same sign, resulting in destabilizing effect on a turbulence. If the streamline is deflected on a convex wall  $\frac{\partial U_1}{\partial x_2}$  and  $\frac{\partial U_2}{\partial x_1}$  has opposite sign, resulting in stabilizing effect on turbulent fluctuations. In the case of  $k - \varepsilon$  model, the production term in the  $k$  equations is:

$$k - \varepsilon : P^k = \mu_t \left( \frac{\partial U_1}{\partial x_2} + \frac{\partial U_2}{\partial x_1} \right)^2 \quad (4.45)$$

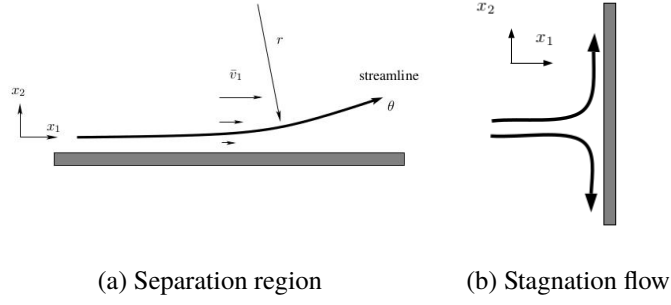


Figure 4.3. Example of a flow pattern when the flow approaches an obstacle [31]

The rotational strains in the production term are multiplied by the same coefficient, turbulent viscosity. Therefore the EVM models are insensitive to streamline curvature. The same applies to the flows with strong adverse pressure gradients and recirculation regions, particularly the  $k - \varepsilon$  model overestimates the shear stress and reduces the separation in flows over curved walls.

In the case of the flow pattern for *stagnation flow*, illustrated in Figure 4.3b again, the  $k - \varepsilon$  model does not model the normal stresses properly. The production term for RSM models is:

$$RSM : \frac{1}{2}(P_{11} + P_{22}) = -\overline{u_1^2} \frac{\partial U_1}{\partial x_1} - \overline{u_2^2} \frac{\partial U_2}{\partial x_2} \quad (4.46a)$$

after applying continuity:

$$\frac{\partial U_1}{\partial x_1} = -\frac{\partial U_2}{\partial x_2}$$

$$P_k = -\frac{\partial U_1}{\partial x_1} (\overline{u_1^2} - \overline{u_2^2}) \quad (4.46b)$$

Term  $(\overline{u_1^2} - \overline{u_2^2})$  is small at the stagnation point, resulting in small production rate of turbulence.

In the  $k - \varepsilon$ , production in the  $k$  equations for this case will be:

$$P_k = 2\mu_t \left( \left( \frac{\partial U_1}{\partial x_1} \right)^2 + \left( \frac{\partial U_2}{\partial x_2} \right)^2 \right) \quad (4.47)$$

The production rate of turbulence will be highly overestimated because of the square of velocity gradients, and the sign is not taken to account.

## 4.9 Law of the wall

In wall-bounded, fully developed, turbulent flow, along the solid boundaries, there is a thin layer where the viscous effects are dominant, and the outer region of inertia-dominated flow. Figure 4.4 illustrates a simple turbulent boundary layer over a plane surface and how

it can be subdivided into two main regions, the outer and inner region. In the outer region, the velocity is determined by the fluid properties, the boundary layer thickness and the wall distance. The size of the turbulent eddies are proportional to the thickness of the boundary layer. In the inner region, the velocity is independent of the boundary layer thickness, and it is dominated by the wall parameters. The inner region is very thin in relation to the boundary layer thickness. Thus, it may be assumed that the total shear stress remains constant across and equal to the wall shear stress,  $\tau_w$ . The size of the turbulent eddies is proportional to the wall distance,  $y$ . The inner region is further subdivided into:

- the fully turbulent inner region,
- the buffer region, where the turbulent eddies are rapidly dampened, and the turbulent shear stress is reduced to practically zero
- the viscous sub-layer, where there are no turbulent fluctuations and only the viscous stress is significant.

Near the wall, the mean velocity depends on the distance from the wall  $y$ , fluid density  $\rho_F$ , viscosity  $\nu$ , and the wall shear stress  $\tau_w$  [135]. In this region, we have:

$$U = f(y, \rho_F, \nu, \tau_w) \quad (4.48)$$

The dimensional analysis leads to a relation known as the *law of the wall*:

$$u^+ = f\left(\frac{\rho_F u_\tau y}{\nu}\right) = f(y^+) \quad (4.49)$$

The formula contains two dimensionless groups, non-dimensional velocity  $u^+$  and spatial coordinate normal to the surface  $y^+$ , defined as:

$$u^+ = \frac{u}{u_\tau} \quad (4.50a)$$

$$y^+ = y \frac{u_\tau}{\nu} \quad (4.50b)$$

Where  $u_\tau$  is the friction velocity is defined as:

$$u_\tau = \sqrt{\frac{\tau_w}{\rho_F}} \quad (4.50c)$$

The outer region is independent of viscosity, and the relation for this region is defined by the *defect law*. In this region, the size of the turbulent eddies is constant and proportional to the boundary layer thickness  $\delta$ . Velocity depends on the wall shear stress, fluid density, the boundary layer thickness and wall distance. In this region, we have:

$$U = f(y, \rho_F, \delta, \tau_w) \quad (4.51)$$

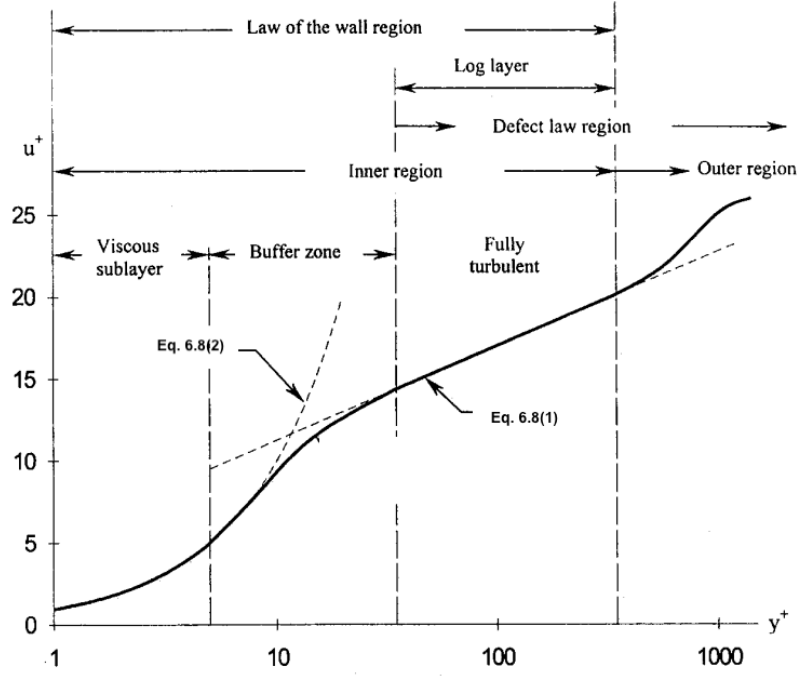


Figure 4.4. Non-dimensional velocity profile for an incompressible turbulent flow over a flat plate [59]. In Figure: Eq. 6.8(2):  $u^+ = y^+$ , Eq. 6.8(1):  $u^+ = \frac{1}{\kappa} \ln(Ey^+)$

Dimensional analysis yields:

$$u^+ = f\left(\frac{U}{u_\tau}\right) = f\left(\frac{y}{\delta}\right) \quad (4.52)$$

In simple boundary layers in local equilibrium within the viscous sub-layer, at a dimensionless distance  $y^+ [\equiv y(\tau_w/\rho_F)^{0.5}/\nu]$  of up to 5, the velocity is linearly proportional to the wall distance, whereas in the fully turbulent inner region,  $y^+ > 30$ , the velocity is logarithmically proportional to the wall distance. This is typically referred to as the *log-law*, or the *universal* law of the wall, depicted in Figure 4.4 where  $u^+ \equiv u(\tau_w/\rho_F)^{0.5}$ . The law of the wall is valid for the viscous sublayer, the buffer zone and the fully turbulent part of the boundary layer. To summarize, the velocity profile varies as follows:

$$u^+ = \begin{cases} u^+ = \frac{1}{\kappa} \ln(y^+) + B = \frac{1}{\kappa} \ln(Ey^+), & y^+ \gtrsim 30 \\ y^+, & y^+ \lesssim 5 \end{cases} \quad (4.53)$$

where the DNS data confirm  $\kappa = 0.41$ , and  $B = 5.25$ . Constant  $E$  is a function of the wall roughness where  $E = 9.8$  is applied for a smooth wall.

In the near wall region, the viscosity effects are dominant, and the relation between velocity and distance from the wall can be approximated to be linear,  $u^+ = y^+$ . The flow is assumed to be independent of viscosity in the log-law region. The relationship between  $y^+$  and  $u^+$  was derived with the assumption that the Reynolds shear stress is constant and equal to the wall shear stress, together with the Boussinesq assumption (Equation 4.14). In the buffer

layer, viscous and turbulent stresses are of similar magnitude and the velocity profile is not well defined in this region.

The velocity gradients are larger close to the wall, hence finer mesh is required to correctly resolve the near-wall region. Providing Equations 4.53 removes the requirement of fully resolving the near wall region and reduces the computational time. The first cell centre needs to be placed in the log-law region in order to ensure the accuracy of the simulation [138]. The strategy of applying the wall functions in modelling of near-wall turbulence is further explained in Section 6.7.3.

## 4.10 Summary

Several RANS turbulence models were introduced in this Chapter. It was mentioned that the convection of turbulence is not-modelled in the zero-equation model. Complex flow fields which include separated flows, require two-equation models to better represent the physics of turbulence.

Despite EVM limitations mentioned in Section 4.8 it is still a widely used approach in industrial applications because of its simplicity and fast performance. Also, EVM class of models is widely validated. As shown, the model will have poor performance in cases with large extra strains such as curved boundary layers or swirling flows. Over-predicting shear stress and reducing the recirculation region in the  $k - \varepsilon$ , has a practical impact in aerospace applications e.g. flow over an airfoil. In these applications, the  $k - \omega$  and  $k - \omega$  SST gives much better performance.

The RSM models address the limitations of the EVMs because it involves an exact representation of the Reynolds stress production and transport processes. Since they solve additional seven PDEs, the computing cost is largely increased. Also, the RSM is relatively difficult to implement, and it is not widely validated as the  $k - \varepsilon$  model. However, with today's achievable high computing performance, the disadvantage of the additional CPU time could not be so meaningful. The model is an accurate choice for many complex flows such as wall jets, fully-developed flows in non-circular ducts or swirling flows.

In the Chapter that follows the mathematical description of the fluid-structure interaction coupling is described.



# Chapter 5

## Fluid Structure Interaction

Fluid-Structure interactions (FSI) can be solved in two ways, monolithic and partitioned approaches. In the monolithic approach, flow and structural equations are combined and solved simultaneously. On the contrary, the partitioned approach requires separate solvers for the flow and structural equations. The partitioned approach thus requires implementing a coupling scheme to conserve the momentum and energy across the interface. The partitioned method is implemented in the OpenFOAM for fluid-solid interaction solver [130] therefore, this chapter will focus on the coupling of partitioned methods.

### 5.1 Coupling schemes

In the partitioned methods, fields required for a solution are defined at the boundary between fluid and solid interface. Variables are transferred between the fluid and solid surface from the fluid patch to the solid patch, as illustrated in Figure 5.1.

There are two solution procedures defining the fields which are exchanged at the fluid-structure interface: *one-way coupling*, also identified as weak coupling, and *two-way coupling*, known as strong coupling scheme. In the case of one-way coupling calculations, only the pressure and viscous force increment ( $\delta p_I$   $\delta t_I$ ) from the fluid interface is transferred to the structure solver interface [7]. With two-way coupling, the displacement increment at the solid side of the interface ( $\delta u_I$ ) and velocity ( $v_I$ ) is also transferred to the fluid side of the interface.

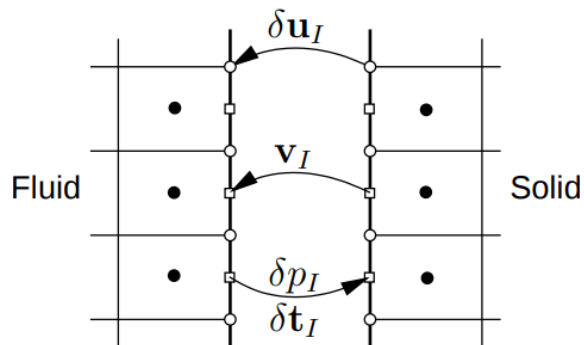


Figure 5.1. Transfer of coupling data in OpenFOAM [129]

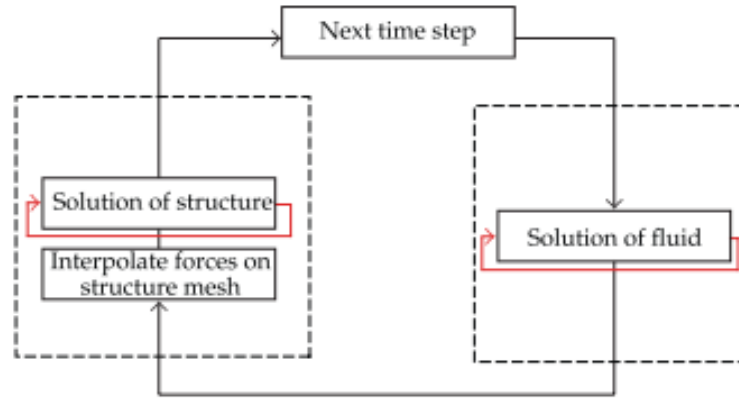


Figure 5.2. Solution algorithm for one way coupling [7]

### 5.1.1 One-way coupling

The entire weak coupling loop is conveniently illustrated in Figure 5.2. In the process algorithm goes as follows, (1) fluid field is solved until the convergence criteria is reached, (2) the calculated fluid forces are transferred to the structural solver boundaries, (3) the solid side is solved until the convergence criteria are reached, (4) the fluid flow is advanced to the next time step and calculated to convergence. In the weak approach, solvers for fluid and solid are applied sequentially only once per time step. Even though both solvers are implicit, the entire system is solved explicitly, which implies possible stability issues, and limitations on the time-step [70].

The one-way coupling algorithm is not a suitable choice for the simulation of flow-induced vibrations because of a time lag between fluid and solid solution and potential errors on loads transfer from the fluid boundary face to solid boundary faces with slender structures. Also, the literature research on experimental assessment of the FIV presented in Section 2.2 shows that sufficiently high flow velocities induce high deformation of the solid structure. The vibration amplitude can be sufficient to change the flow passage; therefore, the deformation of the fluid mesh is necessary.

### 5.1.2 Two-way coupling

In the two-way fluid-solid interactions formulation, the motion of the beam is induced by the fluid forces, but simultaneously the motion of the beam induces the fluid motion [50].

The fluid governing equations and solid models are coupled by two following conditions, which must be satisfied at the fluid-solid interface:

1. The kinematic coupling condition: The viscid fluid follows the motion of the neighbouring solid, thus the velocity and displacement must be continuous across the inter-

face:

$$u_{F,i} = u_{S,i} = \frac{dx_{S,i}}{dt} \quad (5.1)$$

Where  $u_F$  is the velocity of the fluid and  $x_S$  is the solid displacement, subscript  $i$  represents the quantities at the fluid-solid interface.  $x_S$  is equivalent to the  $u$  displacement in the solid governing equation, Equation 3.27.

2. The dynamic coupling condition follows the Newton Third Law of motion '*action = reaction*'. Fluid forces and solid forces are equal at the interface:

$$n_i \sigma_{F,i} = n_i \sigma_{S,i} \quad (5.2)$$

Where  $n_i$  is the normal unit vector at the interface. Subscripts  $F$  and  $S$  correspond to the fluid and solid domain, respectively.

The first interface condition is applied as the Dirichlet boundary condition. Velocity from the solid side is the boundary condition for the fluid. The second interface condition is realised as the Neumann boundary condition: the force, traction, from the fluid is applied as the boundary condition on the solid. The traction is calculated by using the fluid stress tensor  $\sigma_{F,i}$  which consists of the isotropic and viscous components, defined in the Navier-Stokes momentum equation (Equation 4.6):

$$\sigma_{F,i} = -p\delta_{ij} + \tau_{ij} \quad (5.3)$$

Where  $\tau_{ij}$ , viscous stress of a Newtonian fluid defined in Equation 4.7. The traction at the interface is finally:

$$t_{F,i} = n_i \sigma_{F,i} \quad (5.4)$$

This algorithm is known as the Dirichlet-Neumann (DN) approach, the flow model is solved for a given velocity (or solid displacement), and the solid model is solved for a given force imposed on the interface.

## 5.2 Gauss-Seidel scheme

The implicit method, with strong coupling, can be of second-order accuracy and are more stable [21]. To ensure that the equilibrium of the velocity and force on the fluid-solid interface is met for each time step, the strongly coupled Gauss-Seidel iteration procedure is applied. The non-linear system of fluid and solid coupled equations may be solved by sub-iterating between fluid and structure, with a relaxation step on the structure displacement. The flow chart of the coupled solution procedure is illustrated in Figure 5.3.

At every step,  $t^n$ , the Dirichlet-Neumann algorithm iterates over the fluid and solid sub-iteration until convergence is satisfied. The sub-iteration index is denoted by  $k$ . The as-

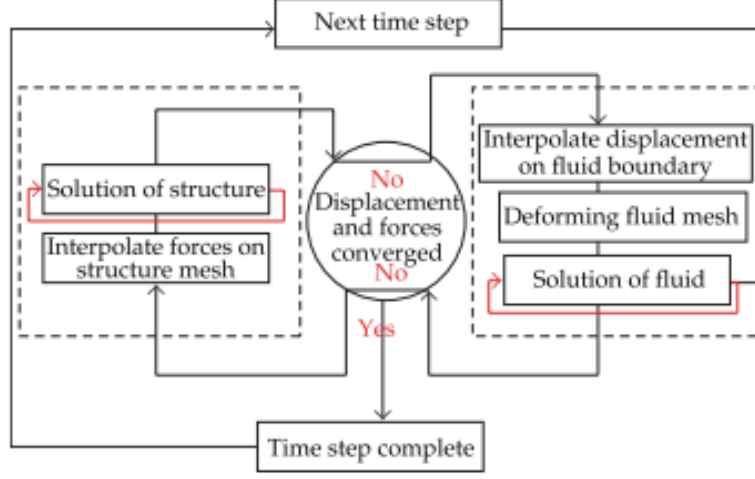


Figure 5.3. Strong, two-way coupling algorithm [7]

sumption is that the flow variables  $u_k, p_k$  and structure position  $x_k$  are known at  $k = 0$ . In the strongly coupled DN algorithm, the following steps are performed [50] :

- **Step 1:** Solve the fluid subiteration for  $u_{k+1}, p_{k+1}$  defined on fluid domain with Dirichlet boundary condition:

$$u_{k+1} = \frac{dx_k}{dt} \quad (5.5)$$

- **Step 2:** Solve for the new displacement of the structure  $x_{k+1}$ , using the just calculated fluid force  $\sigma_{F,k+1}$
- **Step 3:** Check the fluid-structure convergence criterion  $\epsilon_{FS}$ . It is defined as the change of the mean displacements:

$$\frac{\|x_{k+1} - x_k\|}{x_k} < \epsilon_{FS} \quad (5.6)$$

If satisfied set the next time step,  $x^{n+1} = x_{k+1}$  and  $p^{n+1} = p_{k+1}$ , if not repeat Steps 1-3.

- **Step 4:** Update the fluid mesh with the standard ALE update.

### 5.3 Under-relaxation

The simple block, Gauss-Seidel iterative algorithm requires a small relaxation value and a large number of sub-iterations [21, 92]. In order to accelerate the sub-iteration convergence, relaxation procedures can be applied.

The most straightforward technique is to use fixed relaxation factor  $\omega_k$  for all time steps. The currently calculated displacements  $\tilde{x}_k$  are linearly weighted with the displacements from the previous iteration  $x_{k-1}$ . At the **Step 2**, the fixed under-relaxation factor  $0 < \omega_k \leq 1$  is introduced, and the displacement  $x_{k+1}$  is calculated as follows:

$$x_k = \omega_k \tilde{x}_k + (1 - \omega_k) x_{k-1} \quad (5.7)$$

As shown in references [78, 121] it is relatively hard to estimate the optimal value of the  $\omega_k$ . It must be small enough to prevent the simulation from diverging but high enough to avoid extra, unnecessary FSI iterations. Therefore dynamic relaxation techniques will be further considered.

The Aitken acceleration procedure, [65] is based on using dynamically changing relaxation factor  $\omega_{k+1}$ , extrapolated with the displacements from the two preceding iterations. The unrelaxed displacement predicted by the **Step 2** will be denoted by  $\tilde{x}_{k+1}$ . The relaxation parameter  $\omega_{k+1}$  is then [4]:

$$\omega_{k+1} = \frac{(x_k - x_{k-1}) \cdot (x_k - \tilde{x}_{k+1} - x_{k-1} + \tilde{x}_k)}{|x_k - \tilde{x}_{k+1} - x_{k-1} + \tilde{x}_k|^2} \quad (5.8)$$

The update of the interface position is given by:

$$x_{k+1} = \omega_{k+1} \tilde{x}_{k+1} + (1 - \omega_{k+1}) x_k \quad (5.9)$$

This relaxation procedure is found to be simple to implement and efficient [78].

Lastly, the IQN-ILS, interface- quasi-Newton with inverse Jacobian from a least-squares model developed by [40] is available in the FSI container. As it was shown, the IQN-ILS approach is more complex and difficult to implement than the Aitken method [40]. For the project's current needs, the Aitken procedure will be adopted.

## 5.4 ALE formulation

Generally, the continuum mechanics algorithms use two classical motion descriptions: the Lagrangian and the Eulerian. Lagrangian techniques are employed in structural mechanics because each node of the computational mesh tracks the related material particle during motion. This technique facilitates following free surfaces and interfaces between various materials. Its limitation is that it cannot track large deformations in the computational domain without frequent re-mesh operations. In fluid dynamics, Eulerian techniques usually are applied. The computational mesh is fixed, while the continuum moves with respect to the grid. Large deformations in the continuum motion may be handled relatively quickly in the Eulerian description, albeit at the price of exact interface definition and resolution of flow details.

When modelling the FSI problem, the moving structure is described in a Lagrangian frame of reference, and fluid equations need to be computed in the time-varying boundary. It is achieved by using an Arbitrary Lagrangian-Eulerian (ALE) frame of reference in the fluid domain. The principle behind the ALE formulation is that the observer is neither at the fixed position in space nor moves with the material point. It is mathematically solved by using a relative velocity in convective terms of the conservation equations. Thus, the interface grid velocity,  $w$ , is employed in the convective term of the momentum equation. The

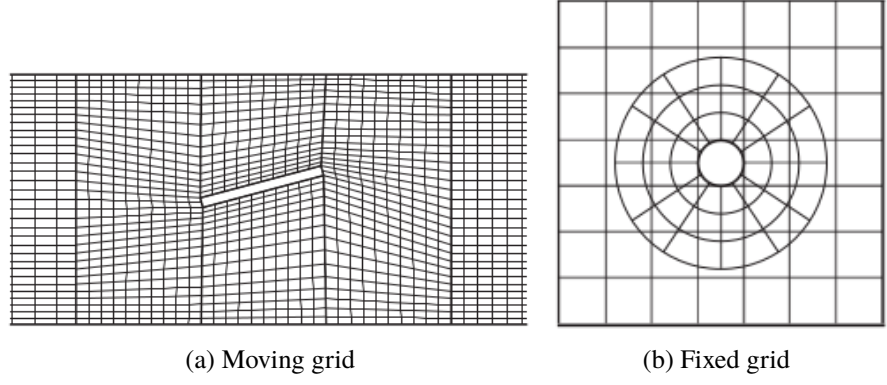


Figure 5.4. Examples of moving grid approaches [124]

conservation of mass and conservation of momentum (Equations 4.5, 4.6) are therefore reformulated to include the moving boundary:

$$\frac{\partial(U_i)}{\partial x_i} = 0 \quad (5.10a)$$

$$\frac{\partial(\rho_F U_i)}{\partial t} + \frac{\partial}{\partial x_j} [\rho_F (U_i - w) U_j] = -\frac{\partial P}{\partial x_i} + \frac{\partial}{\partial x_j} \left( \mu_F \frac{\partial U_i}{\partial x_j} \right) \quad (5.10b)$$

When  $w = 0$  and when  $w = U_i$ , the pure Euler and Lagrange formulations are restored, respectively. One of the major difficulties in the time integration of ALE Navier-Stokes equations is the non-linear term arising with the relative velocity  $U_i - w$ . The ALE description's practical implementation needs the development of an automated mesh-displacement method.

## 5.5 Mesh Deformation

When the fluid solution domain changes dynamically due to the movement or deformation of solid elements, the accompanying mesh dynamics become essential. There are two ways towards this problem: fixed grid and moving grid approach, as illustrated in Figure 5.4. In the fixed-grid methods, Figure 5.4b, the structure may freely move across the fixed Cartesian fluid grid without affecting the fluid's discretisation. The challenge is establishing the contact conditions between the structure and the fluid. Meshes which are required to resolve boundary layers in viscous flows are not enabled in this method [76].

Moving mesh approaches, Figure 5.4a, enable conducting flow simulations when the shape of the flow domain changes. Motion can be determined with simple interpolation techniques or more complex laplacian and pseudo-structure smoothing techniques. The mesh motion interpolation can also be defined with the Radial Basis Function (RBF) developed by Bos [13]. The RBF enables high-quality mesh, especially when dealing with large rotations. Motion equation based on laplacian smoothing is relatively cheap but does not maintain high mesh quality during high rotation angles or large deformation [67, 69].

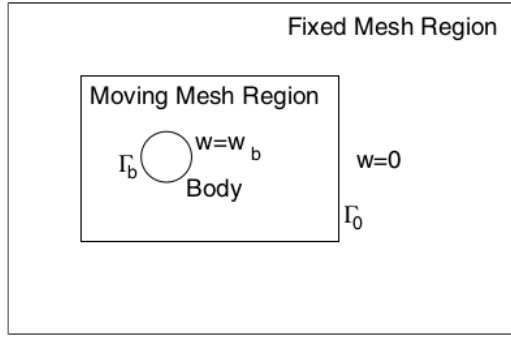


Figure 5.5. Mesh velocity field  $w$  [85]

## Distance-based methods

For the small amplitude of vibrations, the mesh motion will be computed with a Laplace equation with a diffusion coefficient that changes throughout the domain. This moving mesh approach is applied in OpenFOAM container for FSI [69].

To explain the approach, Figure 5.5 illustrating the mesh movement boundary conditions is first introduced. If the velocity of the solid surface is known,  $u_{s,i}$  from the Equation 5.1, the mesh velocity of a moving grid,  $w|_{\Gamma_b}$  is specified. Far away from these moving boundaries, the mesh velocity  $w|_{\Gamma_0}$  decreases to zero, and the grid is fixed [85]:

$$w|_{\Gamma_b} = u_{s,i} \quad (5.11a)$$

$$w|_{\Gamma_0} = 0 \quad (5.11b)$$

The objective is to generate a mesh velocity field with  $w$  the minimal element distortion. One way to obtain this is to smooth the velocity field. Figure 5.6 depicts the mesh movement for a 1D case. Mesh velocity is  $w_0$  at the domain's left end and vanishes at the right end. Assuming a linear decrease in mesh velocity and  $\Delta h$  as the change in size over a time-step for any two elements, we have:

$$\frac{\partial w}{\partial x} = g_w \quad (5.12a)$$

$$\Delta h = (w_2 - w_1)\Delta t = \Delta w \Delta t \quad (5.12b)$$

The size ratio between two elements  $(i, j)$  will be:

$$\left. \frac{h_i}{h_j} \right|^{n+1} = \frac{h_i + \Delta w_i \Delta t}{h_j + \Delta w_j \Delta t} = \frac{h_i + g_w h_i \Delta t}{h_j + g_w h_j \Delta t} = \left. \frac{h_i}{h_j} \right|^n \quad (5.13)$$

To conclude, the elements will retain their original size ratios, hence they will be deformed in approximately the same way.

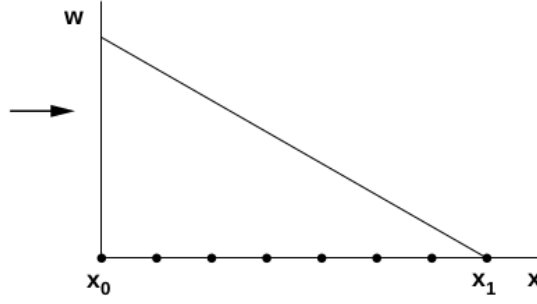


Figure 5.6. Velocity field vs. 1D mesh distortion  $x$  [85]

For the general case with constant gradients, the mesh velocity can be obtained by solution of the Laplace equation, with boundary conditions defined in the Equations 5.11a, 5.11b.

$$\frac{\partial}{\partial x_i} \left( \gamma \frac{\partial w}{\partial x_j} \right) = 0 \quad (5.14)$$

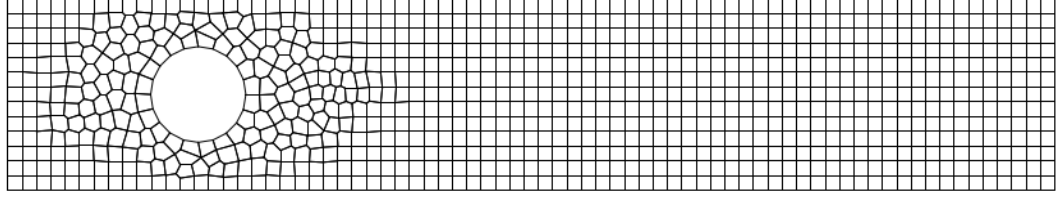
The largest point movement occurs next to the moving boundary when the Laplace equation determines the mesh motion. It implies that flow phenomena near the wall will be largely distorted, naturally leading to a loss of accuracy. The most extensive distortion should occur ideally inside the mesh. The solution is to apply diffusion coefficient  $\gamma$  as a function of distance from the body,  $l$ . The method was implied by Löhner and Yang in 1996 [84]. In OpenFOAM the *distance-based* applied method is similar to the originally proposed by Löhner and Yang [68]. The diffusion coefficient  $\gamma(l)$  is defined as:

$$\gamma(l) = \frac{1}{l^m} \quad (5.15)$$

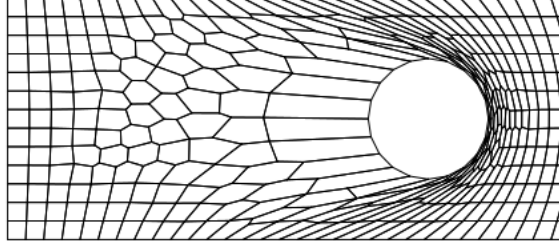
At small  $l$  the  $\gamma$  coefficient is high, leading to a small gradient of mesh velocity  $w$ . For large  $l$ ,  $\gamma$  is small, leading the large velocity gradient away from the moving body.

The mesh distortion method was tested numerically in [68]. In the tested case, the cylinder of a diameter  $D$  was moved in a channel of a height equal to  $2D$ . The channel's left and right boundaries are fixed, and a slip boundary condition is applied at the top and bottom. Constant motion velocity is applied for the cylinder boundary. Initial mesh is depicted in Figure 5.7a. Examples of mesh motion performance produced by the method are depicted in Figures 5.7b-5.7d. If the mesh velocity is obtained with the Laplace equation without a diffusion coefficient, the final mesh remains valid up to maximum cylinder displacement  $\Delta_{max}$  of  $1.2D$ . However, it is visible that the mesh quality is not satisfactory, and it needs to be improved close to the cylinder walls. The linear distance-based method where diffusivity field is inversely proportional to the distance from the boundary,  $\gamma(l) = l^{-1}$ , improves the mesh quality near the circle, with a maximum displacement of  $\Delta_{max} = 1.1D$ . With the quadratic function, the mesh quality near the wall is even more improved, but the cylinder could be displaced to the maximum distance of  $0.95D$ . Overall, it can be observed that the diffusion coefficient serves as a 'stiffness' to a mesh and improves the mesh quality near the moving object.

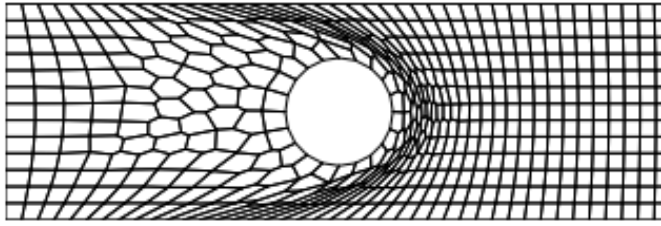




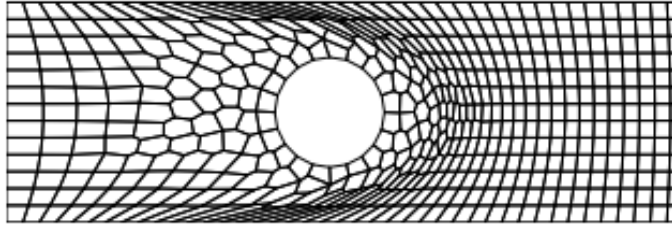
(a) Initial polygonal mesh



(b) Constant mesh distortion  $\gamma(l) = 1$ ,  $\Delta_{max} = 1.2D$



(c) Linear distance-based:  $\gamma(l) = l^{-1}$ ,  $\Delta_{max} = 1.1D$



(d) Quadratic distance-based:  $\gamma(l) = l^{-2}$ ,  $\Delta_{max} = 0.95D$

Figure 5.7. Examples of deformed mesh fields with Laplace mesh motion equation [68]

## 5.6 Interpolation at the fluid-structure interface

As illustrated in Figure 5.1 pressure and viscous forces determined at the fluid side of the interface must be transferred to the solid side interface and reversed. The most straightforward technique of mapping data across the interface is to use conforming meshes, then no interpolation of data is required. However, meshes on the solid and fluid side are often non-conformal, requiring an interpolation method between the meshes. In the FSI container in OpenFOAM, a reliable interpolation technique was proposed [130].

The process has two stages: *face interpolation procedure* with the interpolation of the fluid side boundary cell faces to the solid side boundary cell faces with the Generalised Grid Interface (GGI) coupling [5]. A face centre traction value at the solid side interface is calculated using the tractions at the face centres at the fluid side of the interface. Force at the

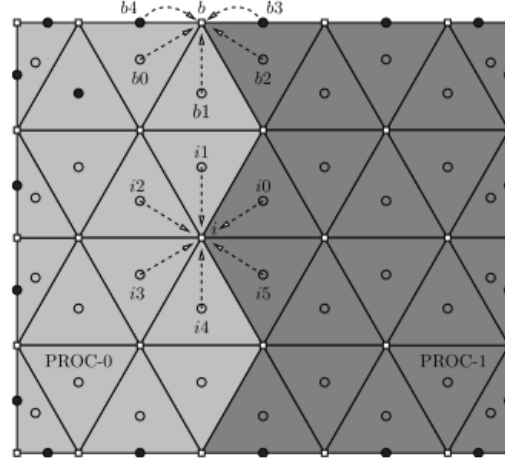


Figure 5.8. Interpolation for the vertex field in two-dimensional FV mesh [130]

centre of the solid face  $j$  is defined as:

$$t_{S,j} = \sum_k w_{j,k} t_{F,k} \quad (5.16)$$

where  $t_{F,k}$  is the traction at the centre of the fluid face  $k$ . Summation is applied to all fluid side faces  $k$  that intersect with solid side faces  $j$ . The  $w_{j,k}$  is the weighting factor between two patches, fluid face  $k$  and solid face  $j$ .

Unlike the fluid solver, the solid solver store the displacement and material properties at the vertices. Vertex-displacements  $i$  are interpolated from all cell-centre displacements  $i0 - i5$  sharing the vertex, Figure 5.8. The same figure illustrates that an additional inner-processor data exchange is applied when the vertex has to be interpolated from nodes on different processors.

The *vertex interpolation* procedure is applied for transferring displacements from the structural solver to the fluid solver. The displacements at the solid side are first translated to the face centre displacements. Faces on the solid side are decomposed into triangles using an extra central point. Then the displacement value at the central point is calculated with weighted interpolation. The GGI interface, Equation 5.16, interpolates the solid face centre displacements to the fluid centre displacements, causing the mesh to move [56].

## 5.7 Summary

The section was set out to determine the major elements that must be considered while designing the FSI model for analysing the axial flow-induced vibrations. The primary focus was to describe the two-way coupling scheme with small displacements. Because of the stability, the classical Dirichlet-Neumann coupling algorithm with Aitken's acceleration can be adopted for further FIV analysis. The choice is also constrained by the implementation readily available in the OpenFOAM. The quantitative analysis of the FSI cases tested in [130] showed good agreement with the available results. The standard ALE methods fail

only when the displacement is large [4] and that is not the case for the axial flow-induced vibration. Similarly, the mesh deformation method described will be suitable only for small deformations. Despite the constraints, the parallelisation approach of the OpenFOAM's FSI solver makes it an appropriate choice for industrial applications.

What follows is a description of several different discretisation schemes of the fluid equations and numerical methods on the fluid side implemented in OpenFOAM.

# Chapter 6

## Discretization of the fluid equations

This chapter discusses how the constitutive equations of the fluid motion are numerically solved. The Navier-Stokes equations are a set of coupled, non-linear partial differential equations (PDEs). In order to solve them numerically, the PDEs are transformed into a system of linear algebraic equations using the finite volume method. The discretization procedure in the finite volume method involves two steps. The process starts by dividing the flow domain into several small control volumes. Then it is necessary to integrate the partial differential equations over a control volume and translate them into equations of equilibrium. Interpolation methods are chosen to estimate the variable variation between the values on the surfaces and values on the cell centres. The following sections will present the Finite Volume method with details on the discretization of diffusion, convection and transient terms. The pressure-velocity coupling algorithm followed by Rhie-Chow interpolation is presented to compute the flow field for incompressible fluid flows. The performance and limitations of iterative algorithms with preconditioning are reviewed. Finally, a set of boundary conditions used in the numerical modelling of the turbulent fluid is provided.

### 6.1 Finite Volume method

The steady convection-diffusion equation for a general variable,  $\phi$  is:

$$\frac{\partial(\rho_F U_j \phi)}{\partial x_j} = \frac{\partial}{\partial x_j} \left( \Gamma \frac{\partial \phi}{\partial x_j} \right) + S_\phi \quad (6.1)$$

Where  $\Gamma$  is the diffusion coefficient of  $\phi$ , and  $S$  is the source term. Integrating over a control volume  $V$ , results in:

$$\int_V \frac{\partial(\rho_F U_j \phi)}{\partial x_j} dV = \int_V \frac{\partial}{\partial x_j} \left( \Gamma \frac{\partial \phi}{\partial x_j} \right) dV + \int_V S_\phi dV \quad (6.2)$$

Applying the Gauss's divergence theorem enables to convert the volume integral to the surface integral around the boundary of a control volume. This can be written as:

$$\int_A \rho_F U_j \phi n_j dA = \int_A \Gamma \frac{\partial \phi}{\partial x_j} n_j dA + \int_V S_\phi dV \quad (6.3)$$

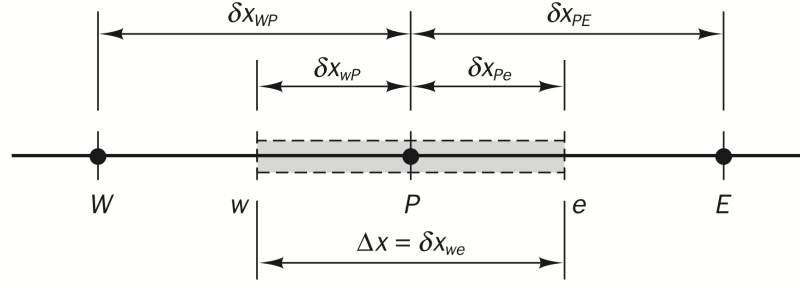


Figure 6.1. One dimensional grid used for discretization [135]

Where  $n_i$  is the normal vector to the control volume surface, and  $A$  is the surface area of the control volume.

In order to demonstrate the discretization, a simple one dimensional domain with a regular Cartesian grid, as shown in Figure 6.1, is considered. The control volume with the central node  $P$  is bounded by the cell faces: *east*,  $e$ , and *west*,  $w$ . The values of the property  $\phi$  are evaluated at nodal points  $P, W, E$ .

The volume integral is approximated by taking the average value of a source  $\bar{S}$  over the control volume  $\Delta V$ . The average source value is simply the value at central node  $(S_\phi)_P$ .

$$\int_V S_\phi dV \simeq \bar{S}_\phi \Delta V \simeq (S_\phi)_P \Delta V \quad (6.4)$$

In the absence of sources, the integration of the transport equation at its nodal point  $P$  gives:

$$(\rho_F U A \phi)_e - (\rho_F U A \phi)_w = \left( \Gamma A \frac{\partial \phi}{\partial x} \right)_e - \left( \Gamma A \frac{\partial \phi}{\partial x} \right)_w \quad (6.5)$$

Where  $(\rho_F U A)_e = F_e$  and  $(\rho_F U A)_w = F_w$  are mass fluxes through east and west faces. The flow must also satisfy the continuity equation thus:

$$F_e - F_w = 0 \quad (6.6)$$

## 6.2 Diffusion terms

The linear approximation is applied to calculate the gradients  $\partial \phi / \partial x$  at the control volume faces. Central difference formula uses values at nodal points  $E$  and  $W$  to estimate the gradient at the nodal point  $P$ .

$$\left( \frac{\partial \phi}{\partial x} \right)_P = \frac{\phi_E - \phi_W}{2\Delta x} + O(\Delta x^2) \quad (6.7)$$

Here for the uniform grid spacing  $\Delta x = \delta x_{WP} = \delta x_{EP}$ , the central difference approximation method is second order accurate, hence the error is proportional to the  $\Delta x^2$  [135].

The gradient at the cell face, e.g.  $'e'$ , is evaluated at the midpoint between  $P$  and  $E$ :

$$\left(\frac{\partial\phi}{\partial x}\right)_e = \frac{\phi_E - \phi_P}{\Delta x} \quad (6.8)$$

The diffusive flux terms are then evaluated as:

$$\left(\Gamma A \frac{\partial\phi}{\partial x}\right)_e = \Gamma_e A_e \left(\frac{\phi_E - \phi_P}{\delta x_{PE}}\right) \quad (6.9a)$$

$$\left(\Gamma A \frac{\partial\phi}{\partial x}\right)_w = \Gamma_w A_w \left(\frac{\phi_E - \phi_W}{\delta x_{WP}}\right) \quad (6.9b)$$

In the non-uniform grids, faces of a control volume are not at the midpoint between the nodes. To account for this interpolation factors  $f_W$  and  $f_P$  are introduced. The diffusion coefficients are interpolated to the cell faces  $w$  and  $e$  with the following formulas:

$$\Gamma_w = (1 - f_w)\Gamma_W + f_w\Gamma_P \quad (6.10a)$$

$$f_w = \frac{\delta x_{Ww}}{\delta x_{Ww} + \delta x_{wP}} \quad (6.10b)$$

$$\Gamma_e = (1 - f_P)\Gamma_w + f_P\Gamma_P \quad (6.11a)$$

$$f_P = \frac{\delta x_{Pe}}{\delta x_{Pe} + \delta x_{eE}} \quad (6.11b)$$

For convenience the diffusion conductance  $D$  at cell faces is introduced:

$$D_e = \left(\frac{\Gamma_e A_e}{\delta x_{PE}}\right) \quad (6.12a)$$

$$D_w = \left(\frac{\Gamma_w A_w}{\delta x_{WP}}\right) \quad (6.12b)$$

The integrated convection-diffusion 6.5 may be now expressed is a following way:

$$0 = -(F_e\phi_e - F_w\phi_w) + (D_e(\phi_E - \phi_P) - D_w(\phi_P - \phi_W)) \quad (6.13)$$

The left-hand side of the equation represents the rate of change of  $\phi_P$ , and the right-hand side represents the net influx across the element surface. In order to solve Equation 6.13, the transported property  $\phi_w$  and  $\phi_e$  at the west and east faces need to be calculated. The discretization schemes of the convection term are discussed in the next section.

## 6.3 Convection schemes

The default convection schemes employed in the further study are now presented. Initially, this term is discretized with linear approximation as the diffusion terms. The issues with this discretization scheme are presented. Then the more stable upwind scheme is described, followed by a description of higher-order profiles reducing the discretization error that are upwind biased.

### 6.3.1 Central differencing

Central differencing approximation was described in a diffusion terms section, Equation 6.7 and 6.8. For a uniform grid the face values reads as:

$$\phi_e = (\phi_P + \phi_E)/2 \quad (6.14a)$$

$$\phi_w = (\phi_W + \phi_P)/2 \quad (6.14b)$$

The approximation of convective terms, equations 6.14, and diffusive terms, equations 6.12, can be substituted to the integrated transport Equation 6.13. After rearrangements the discretization equation becomes:

$$a_P = a_W\phi_W + a_E\phi_E \quad (6.15)$$

with coefficients  $a_W$ ,  $a_E$  and  $a_P$  defined as:

$$a_E = D_e - F_e/2 \quad (6.16a)$$

$$a_W = D_w + F_w/2 \quad (6.16b)$$

$$a_P = a_E + a_W + (F_e - F_w) \quad (6.16c)$$

This scheme provides an accurate solution as long as diffusion is the dominant transfer mechanism. However, it produces nonphysical oscillations once the convection overwhelms diffusion. Due to this constraint, central differencing is not suitable for general-purpose flow calculations [135].

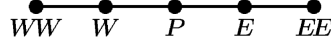


Figure 6.2. A schematic showing the  $EE$  and  $WW$  nodes locations used for describing the SOU scheme profile [48]

### 6.3.2 Upwind scheme

In the upwind differencing scheme the flow direction determines the value at the cell faces. The value  $\phi$  at the face can be approximated by the first node upstream to the face. For the east face of a cell the upwind scheme sets:

$$\phi_e = \phi_P \text{ for } F_e > 0 \quad (6.17a)$$

$$\phi_e = \phi_E \text{ for } F_e < 0 \quad (6.17b)$$

Where  $F_e$  is the mass flux through the east face of the cell defined in Equation 6.5, the discretisation equations can be found in Appendix A. The scheme is stable and always bounded [87]. That is, when the condition is satisfied, an increase/decrease of a variable  $\phi$  at one node should result in an increase/decrease of the net influx - the value of  $\phi_{nb}$  at neighbouring nodes. The scheme is first-order accurate; therefore, the error decreases linearly with the grid spacing. To achieve the adequate accuracy of the solution, a very fine grid may be required.

### 6.3.3 Second order upwind scheme

To improve the accuracy of the upwind schemes the value of a scalar at face is approximated by the second order upwind extrapolation (SOU). The linear profile is constructed by employing the values  $\phi_{EE}$  and  $\phi_{WW}$  depicted schematically in the Figure 6.2

For a uniform grid, at the east face the of a cell the the second order upwind sets [87]:

$$\phi_e = \frac{3}{2}\phi_P - \frac{1}{2}\phi_W \text{ for } F_e > 0 \quad (6.18a)$$

$$\phi_e = \frac{3}{2}\phi_E - \frac{1}{2}\phi_{EE} \text{ for } F_e < 0 \quad (6.18b)$$

Similarly to the upwind scheme, this scheme is a lot more stable than central differencing but not bounded [109]. It can be oscillatory when the gradient  $\nabla\phi$  is strong, therefore the commercial codes limit the gradient to prevent oscillations [1, 49]. The scheme is also second-order accurate [88]. Details on discretisation can be found in the Appendix B.



### 6.3.4 QUICK scheme

The QUICK (Quadratic Upstream Interpolation for Convective Kinetics) uses a quadratic interpolation profile passing through two upstream nodes and one downstream node. For the uniform grid,  $\phi$  at the east face of a cell is given by the following formula:

$$\phi_e = \frac{3}{8}\phi_E + \frac{3}{4}\phi_P - \frac{1}{8}\phi_W \quad \text{for } F_e > 0 \quad (6.19a)$$

$$\phi_e = \frac{3}{8}\phi_P + \frac{3}{4}\phi_E - \frac{1}{8}\phi_{EE} \quad \text{for } F_e < 0 \quad (6.19b)$$

The discretisation can be found in Appendix C. The scheme is third-order accurate [88], however the solution boundedness is not always guaranteed [135].

### 6.3.5 TVD schemes

In order to avoid issues caused by the QUICK scheme and other higher-order schemes, second-order TVD (Total Variation Diminishing) schemes were developed. TVD scheme is employed to realise the oscillation-free solutions by adding an artificial diffusion or weighting towards upstream contribution. Initially, these schemes have been developed to capture sharper shocks without any misleading oscillations but have also become popular in general CFD applications [135].

The face value  $\phi_f$  in a flux limited scheme is evaluated as:

$$\phi_f = (\phi_f)_{UD} + \Psi(r)[(\phi_f)_{HO} - (\phi_f)_{UD}] \quad (6.20)$$

Where  $\Psi(r)$  is the limiter function to combine the higher-order scheme (HO) with the bounded upwind scheme (UD) and  $r$  is the ratio of successive gradients of  $\phi$ :

$$r = \frac{\phi_P - \phi_W}{\phi_E - \phi_P} \quad (6.21)$$

When the limiter is equal to zero, the upwind scheme is restored. Higher-order schemes are switched on when the limiter  $\phi_f$  is equal to 1. By monitoring the ratio  $r$ , the limiter switches locally to an upwind scheme when it detects significant gradients or changes in slope. The choice of limiter function  $\Psi(r)$  is determined by a particular problem considered.

## 6.4 Temporal discretization

The preceding section discussed the steady state conditions, hence the transient term was not included in the transport equation.

The transport equation for transient behaviour can be formulated as:

$$\frac{\partial(\rho_F\phi)}{\partial t} + L(\phi) = 0 \quad (6.22)$$

Where the  $\partial(\rho_F\phi)/\partial t$  is the transient operator and  $L(\phi)$  is the operator containing all non-transient terms (convection, diffusion and sources). Integrating over the control volume gives:

$$\int_V \frac{\partial(\rho_F\phi)}{\partial t} dV + \int_V L\phi dV = 0 \quad (6.23)$$

Following the spatial discretization about the volume centre  $P$ , gives:

$$\frac{\partial(\rho_F\phi_P)}{\partial t} \Delta V + L(\phi_P^t) \quad (6.24)$$

where  $\Delta V$  is the volume of a discretized element and  $L(\phi_P^t)$  is the operator at some defined time  $t$  expressed as:

$$L(\phi_P^t) = a_P\phi_P^t + \sum_{Neigh} a_F\phi_F^t - b_P \quad (6.25)$$

where  $a_P$ ,  $a_F$  and  $b_P$  are coefficients obtained from the spatial discretization (in the Sections above).

### 6.4.1 First Order Implicit Euler Scheme

In the first order implicit Euler scheme the integration over time interval  $[t, t + \Delta t]$  yields to:

$$\frac{\rho_F\Delta V(\phi_P - \phi_P^o)}{\Delta t} + L(\phi_P) = 0 \quad (6.26)$$

Where no superscript indicates is the current time increment and  $o = t - \Delta t$  indicates the previous time increment. The coefficients of algebraic equation of the spacial operator, Equation 6.25, are assembled to complete the algebraic form of transient scalar equation:

$$\left(a_P + \frac{\rho_F\Delta V}{\Delta t}\right)\phi_P + \sum_{Neigh} a_F\phi_F = b_P - \frac{\rho_F\Delta V}{\Delta t}\phi_P^o \quad (6.27)$$

The scheme is always stable independent of the time step, but it is first-order accurate, indicating that small time steps are necessary to achieve high accuracy solutions [88].

### 6.4.2 Second Order Implicit Euler Scheme

The development of the second order scheme requires expanding the integration to a previous time step,  $t - \Delta t$ , and two steps earlier,  $t - \Delta 2t$ , resulting in:

$$\frac{\rho_F \Delta V (3\phi_P - 4\phi_P^o + \phi_P^{oo})}{2\Delta t} + L(\phi_P) = 0 \quad (6.28)$$

Algebraic coefficients are assembled to the Equation 6.25 result in:

$$a_P = a_P + \frac{3\rho_F \Delta V}{2\Delta t} \quad (6.29)$$

$$b_P = b_P + \frac{2\rho_F \Delta V}{\Delta t} - \frac{\rho_F \Delta V \phi_P^{oo}}{2\Delta t} \quad (6.30)$$

The scheme is second-order accurate and stable. However, it is not bounded. An increase in  $\phi_P^{oo}$  will reduce the  $\phi_P$ , which can lead to unphysical oscillations. The undesirable effects are compensated by the large  $\phi_P^o$  coefficient of the opposite sign.

## 6.5 Pressure velocity coupling

In the last sections, the algorithms were constructed based on the assumption that the velocity was known. In general, the solution for the momentum equation requires the known pressure field. In the case of incompressible flow, the continuity equation can not be used to obtain it. The iterative procedure to address this issue and compute the incompressible flow field, SIMPLE (Semi-Implicit method for Pressure Linked equations) scheme, based on the work of Patankar [107] is implemented.

For the two-dimensional flow the discretized momentum equation for  $u$  and  $v$ , without any sources, has the form:

$$a_P u_P = \sum_{Neigh} a_{nb} u_{nb} + (P_P - P_E) \Delta y \quad (6.31)$$

$$a_P v_P = \sum_{Neigh} a_{nb} v_{nb} + (P_P - P_N) \Delta x \quad (6.32)$$

Where the term  $(P_P - P_E) \Delta y$  is the pressure difference acting on a face area. The first step is to calculate the velocity field based on guessed pressure field  $p^*$

$$a_P u_P^* = \sum_{Neigh} a_{nb} u_{nb}^* + (P_P^* - P_E^*) \Delta y \quad (6.33)$$

$$a_P v_P^* = \sum_{Neigh} a_{nb} v_{nb}^* + (P_P^* - P_N^*) \Delta x \quad (6.34)$$

Where  $U^*$  denotes the velocity field obtained from the guessed pressure field. Now defining the required corrections for the guessed values, such they will gradually satisfy the continuity equation, results in:

$$P = P^* + P' \quad (6.35a)$$

$$U = U^* + U' \quad (6.35b)$$

$$V = V^* + V' \quad (6.35c)$$

The prime values being the necessary corrections. Subtracting the Equation 6.33 from the Equation 6.31 results in:

$$a_P u_P' = \sum_{Neigh} a_{nb} u_{nb}' + (P_P' - P_E') \Delta y \quad (6.36)$$

The SIMPLE algorithm neglects the  $\sum_{Neigh} a_{nb} u_{nb}'$  term because the correction will be zero when the iterating procedure is completed. Otherwise, during the iterating, this term would involve pressure corrections at all grid points of the domain. Velocity-correction formula is then written as:

$$u_P' = u_P^* + \frac{\Delta y}{a_P} (P_P' - P_E') \quad (6.37)$$

The mass flow rate at the cell faces will be corrected as well, giving the following expressions:

$$(u_e^* - u_w^*) \rho_F \Delta y + (v_n^* - v_s^*) \rho_F \Delta x = 0 \quad (6.38)$$

and,

$$(u_e' - u_w') \rho_F \Delta y + (v_n' - v_s') \rho_F \Delta x = -S_m \quad (6.39)$$

Substituting the expressions for the velocity corrections in the continuity equation results in:

$$a_P p_P' = \sum_{Neigh} a_{nb} P_{nb}' - S_m \quad (6.40)$$

where  $S_m = (u_e - u_w) \rho_F \Delta y + (v_n - v_s) \rho_F \Delta x$  is the mass imbalance across the cell. When  $S_m$  is zero then no further corrections are needed.

The sequence in the SIMPLE algorithm can be summarized as:

1. Start with the guessed pressure  $P^*$  and velocity  $U_i^*$
2. Solve the momentum equations for new velocity fields, Equation 6.33.
3. Solve the pressure correction, Equation 6.40
4. Update pressure from the Equation 6.35a, and the velocity fields  $u', v'$  from Equation 6.37
5. Repeat from Step 2 until solution has converged

The PISO algorithm is an enhancement of the SIMPLE algorithm. The acceleration of the iteration is achieved by adding the second correction step after Step 4 of a SIMPLE algorithm.

Second corrector step in the PISO algorithm is:

$$P^{***} = P^{**} + P'' \quad \text{where } P'' = P^* + P' \quad (6.41a)$$

$$U^{***} = U^{**} + U'' \quad \text{where } U'' = U^* + U' \quad (6.41b)$$

$$V^{***} = V^{**} + V'' \quad \text{where } V'' = V^* + V' \quad (6.41c)$$

where  $P^{***}, U^{***}, V^{***}$  is a twice-corrected pressure and velocity.  $P'', U'', V''$  is the second correction of the pressure and velocity fields.

In transient simulations, the second corrector step leads to higher-order temporal accuracy [135]. When applying a second-order temporal differencing scheme (i.e. Section 6.4.2) and suitably small time step, the pressure and velocity fields obtained at the end of the PISO process are accurate enough to proceed to the next time-step immediately, without further iterations. Therefore the PISO algorithm is less expensive than the SIMPLE algorithm and recommended for transient, three-dimensional simulations.

## 6.6 Rhie-Chow Interpolation

The discretization of the pressure term may be achieved by a central difference scheme. The discretized pressure gradient integral will be:

$$\int_V \frac{\partial P}{\partial x} dV = \left( \frac{\partial P}{\partial x} \right)_P \Delta V = \frac{P_E - P_W}{2\Delta x} \Delta V \quad (6.42)$$

The expression involves two alternating points  $E$  and  $W$  for estimating the pressure difference. In the same way, the continuity equation relates the velocity at two alternating grid points:

$$u_E - u_W = 0 \quad (6.43)$$

The pressure gradient term depends on two alternating grid points rather than two consecutive grid points. Similarly, the continuity equation ensures the mass conservation at two alternating grid points. It leads to 'checkerboard' oscillations, an unphysical pressure field that can still appear uniform in the discretized momentum equation.

Rhie and Chow [113] proposed adding a correction to the interpolated face-velocity. The solution involves the addition of the third derivative of pressure gradient term to the interpolated velocity. Cell face velocity  $u_e$  will be:

$$u_e = \frac{u_P + u_E}{2} + \frac{d}{4} \frac{\partial^3 p}{\partial x^3} \bigg|_e \Delta x^3 \quad (6.44)$$

Where the pressure term is:

$$\frac{\partial^3 p}{\partial x^3} \bigg|_e \Delta x^3 = (p_{EE} - 3P_E + 3P_P - P_W) \quad (6.45)$$

The checkerboarding is avoided because the face velocities incorporate the pressure from adjacent cells.

## 6.7 Boundary conditions

Boundary conditions are required to set the constraints to the solution variable  $\phi$ . The following section will discuss the implementation of the inlet, outlet and wall boundary conditions used in the subsequent simulations. The Law of the wall used to develop wall functions was explained in Section 4.9.

### 6.7.1 Inlet

At the inlet boundaries, the distribution of all flow variables needs to be provided, so the values for  $\phi_{inlet}^{n+1}$  are specified as fixed values by the user (Dirichlet condition). Pressure is specified as a homogeneous Neumann boundary condition with zero flux at the boundary (normal gradient to the face equals zero).

When a uniform velocity is applied at the inlet, an approximate inlet and initial estimates of turbulent kinetic energy  $k$ , the turbulence dissipation rate  $\varepsilon$ , may be derived using the following formulae [135]:

$$k = \frac{3}{2} (u_{ref} T_i)^2 \quad (6.46a)$$

$$\varepsilon = \frac{c_\mu^{0.75} k^{1.5}}{l} \quad (6.46b)$$

Where  $u_{ref}$  is a reference flow velocity (m/s) and  $T_i$  is the turbulence intensity. In all following numerical simulations  $T_i = 5\%$ . In Equation 6.46b,  $c_\mu = 0.09$  is a model constant,

$l = 0.07L$  is a length scale proportional to the a characteristic length  $L$  of the mean flow.

For the solution of Reynolds Stress Models, approximate distributions of Reynolds stresses are given as [46, 135]:

$$\overline{u_1^2} = \overline{u_2^2} = \overline{u_3^2} = \frac{2}{3}k \quad (6.47a)$$

$$\overline{u_i u_j} = 0 \quad (i \neq j) \quad (6.47b)$$

The initialization of turbulence specific dissipation rate  $\omega$  follows as [71]:

$$\omega = \frac{k^{0.5}}{c_\mu^{1/4} l} \quad (6.48)$$

#### Fully developed flow at the inlet

One way to generate fully developed inflow conditions for the wall-bounded flows is to extend the computational domain of the channel entrance. However, this method requires a considerable upstream distance (typically in the order of 50 hydraulic diameters [135]). A simpler method is to perform an auxiliary simulation with periodic boundary conditions in the streamwise direction and extract a fully developed velocity field. OpenFOAM provides the steady-state solver for incompressible, 1D turbulent flow [95]. The solver is designed to create fully developed velocity and turbulence inflow conditions ( $k, \varepsilon, \omega, \overline{u_i u_j}$ ). An average target velocity is specified, and the pressure gradient drives the flow until fully developed conditions with the required bulk velocity are reached. The resulting turbulence inflow conditions based on a fully developed flow profile can be then mapped to the inlet of the channel.

#### 6.7.2 Outlet

At an outlet, the profile of  $\phi$  is assumed to be fully developed, which is achieved by setting the normal gradient to the face as zero ( $\frac{\partial \phi}{\partial n} = 0$ ). For the pressure, a Dirichlet boundary condition (fixed value) is imposed to set a reference pressure.

#### 6.7.3 Wall

The no-slip boundary condition for the velocity components is applied at solid walls. It implies that the velocity of the fluid at the wall ( $u_{F,w}$ ) is equal to that of the wall velocity. For the stationary wall, it will be zero; for the moving wall, the appropriate boundary conditions were presented in Section 5.1.2. The pressure gradient normal to the wall is set to zero ( $\frac{\partial p}{\partial n} = 0$ ).

As far as the modelling of near-wall turbulence is concerned, there are two implications:

- The need to use turbulence models that can produce the effects of wall damping on the near-wall turbulence.
- The need to use a fine enough near-wall mesh, typically about 20 grid nodes from the wall to  $y^+$  of around 30, to accurately resolve the buffer layer and viscous sub-layer regions.

The latter can cause prohibitively large increases in computational costs, especially in three-dimensional and time-dependent flows. This is what led to the developments of the wall function strategies.

The primary objective of wall function approach is to avoid the use of fine near-wall grids. As depicted in Figure 6.3, control volume is sufficiently large for the near-wall node to be in the fully turbulent region. The advantage of the wall function is that the viscous and buffer layers, which require approximately 20 control volumes to be adequately resolved in a low-Re-model approach, are covered with a single control volume.

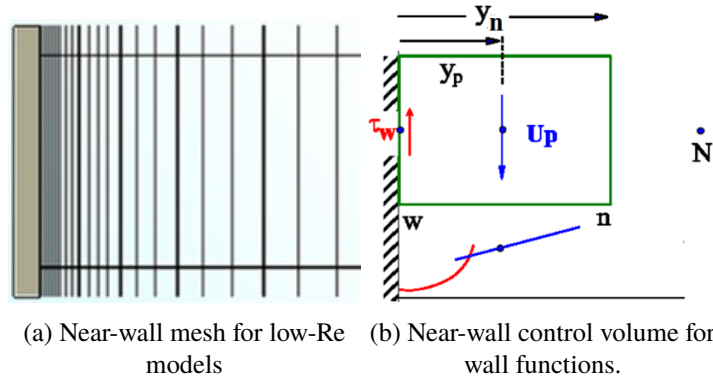


Figure 6.3. Grid resolution with different approaches to near-wall turbulence modelling [62]

The approximation of boundary values relies on the wall function employed. Conventional wall functions are based on the idea that the near-wall velocity varies logarithmically.

$$\frac{U}{U_\tau} = \frac{1}{\kappa} \ln \left( \frac{Ey U_\tau}{\nu} \right) \quad (6.49)$$

where  $U_\tau = (\tau_w/\rho)^{1/2}$ ,  $\kappa = 0.41$ ,  $E = 8.4$ . Applying Equation 6.49 to the near-wall control volume of Figure 6.3b, results in:

$$\frac{U_P}{\sqrt{\tau_w/\rho}} = \frac{1}{\kappa} \ln \left( \frac{Ey_P \sqrt{\tau_w/\rho}}{\nu} \right) \quad (6.50)$$

Several variants of conventional wall functions have been developed from Equation 6.50

In the *standard* version,  $U_\tau [\equiv (\tau_w/\rho)^{1/2}]$  on the right-hand side of Equation 6.50 is replaced by  $c_\mu^{1/4} k_P^{1/2}$ . This results in:

$$\tau_w = \frac{\kappa c_\mu^{1/4} k_P^{1/2} U_P}{\ln(E) c_\mu^{1/4} y_P^*} \quad (6.51)$$

where  $y_P^* = k_P^{1/2} y_P / \nu$ .



Value of the turbulent kinetic energy is derived through the solution of a modified discretized transport equation for the turbulent kinetic energy  $k$  over the near-wall control volume. The modifications include setting the diffusion of  $k$  to the wall to zero then calculating the cell-averaged values of the generation and dissipation rates of turbulence from:

$$\overline{P_k} = \frac{\tau_w^2}{\kappa \rho k_P^{1/2} y_n} \ln \left( \frac{y_n}{y_v} \right) \quad (6.52)$$

$$\overline{\varepsilon} = \frac{k_p^{3/2}}{y_n} \left[ \frac{2}{y_v^*} + \frac{1}{c_l} \ln \left( \frac{y_n}{y_v} \right) \right] \quad (6.53)$$

where  $y_n$  is as in Figure 6.3b,  $y_v^* = 20$  and  $y_v$  the value of  $y$  when  $y k_P^{1/2} / \nu = 20$ .

The average  $P_k$  is derived by analytically integrating the formula from  $y_v$  to  $y_n$ , with the turbulent shear stress,  $\overline{uv}$ , equal to the wall shear stress,  $\tau_w$ , and the velocity gradient derived from the log-law equation 6.49. The average  $\varepsilon$  is determined using analytical integration by assuming that from the wall to  $y_v$ ,  $\varepsilon = 2\nu k_P / y_v^2$  and from  $y_v$  to  $y_n$ ,  $\varepsilon = k_P^{3/2} / c_l y$ .

$$\varepsilon = k_P^{3/2} / c_l y \quad (6.54)$$

Equations 6.51, 6.52, 6.53 make up the *standard* wall function, though in the case of OpenFOAM instead of equations 6.52 and 6.53 the cell-averaged values of  $P_k$  and  $\varepsilon$  are approximated by their nodal values, with the latter evaluated from equation 6.54.

The general application of the wall function concept to second-moment closures can be found in [94]. In the case of OpenFOAM zero gradient boundary condition is applied for the Reynolds stress tensor field:

$$\frac{\partial \overline{u_i u_j}}{\partial n} = 0 \quad (6.55)$$

The same method is applied for the  $k-\omega$  model with wall functions by requiring dissipation of turbulent kinetic energy to balance its production rate,  $\omega_C$  is:

$$\omega_C = \frac{k_C^{1/2}}{\kappa C_\mu^{1/4} y_C} \quad (6.56)$$

## 6.8 Solution algorithm

The discretisation of the transport equations results in a set of linearised coupled equations assembled for all control volumes. A final form is expressed as:

$$[A][\phi] = [b] \quad (6.57)$$

Where  $A$  is the sparse matrix of coefficients of elements  $a_{ij}$ ,  $\phi$  is the vector of unknown variables, and  $b$  is the vector containing all sources, constants and boundary conditions. As

shown in [87] direct methods of solving linear systems of equations such as Direct Matrix Inversion, Gauss Elimination or TriDiagonal Matrix Algorithm (TDMA) are generally not recommended for solving large systems of equations because they are computationally expensive. Most CFD codes use iterative methods. The sparse coefficient matrix  $A$  can be decomposed into upper triangular  $U$ , lower triangular  $L$  and the diagonal matrix  $D$  as in the Equation 6.58.

$$A = D + L + U \quad (6.58)$$

In the Jacobi method iteration sequence is performed as in the Equation 6.59:

$$D\phi^{(m+1)} = -(L + U)\phi^{(m)} + b \quad (6.59)$$

where  $\phi^{(m)}$  is the solution estimate at the iteration  $m$  and  $\phi^{(m+1)}$  is a new solution estimate. As the number of iterations  $m$  increases, the solution  $\phi^{(m)}$  will converge to the exact solution  $\phi$ . However, usually, the exact solution is not required and stopping criteria are introduced. The solution algorithm monitors the residual  $r^{(m)}$ , which is a measure of the solution convergence. It is defined in the Equation 6.60:

$$r^{(m)} = A\phi^{(m)} - b \quad (6.60)$$

### 6.8.1 Conjugate Gradient method

The Conjugate Gradient (GC) method is another solution procedure used in the CFD calculations. As shown in [87] this scheme converges faster than the iterative methods presented above, and it is recommended for large problems with unstructured meshes. The basic principle behind the method is to define the search path  $d^{(m)}$  to obtain a new solution estimate:

$$\phi^{(m+1)} = \phi^{(m)} + \alpha^{(m)}d^{(m)} \quad (6.61)$$

Where  $\alpha^{(m)}$  is some relaxation factor computed at each iteration, so the next residual is small as possible. It is calculated by the Equation 6.62:

$$\alpha^{(m)} = \frac{(d^{(m)})^T r^{(m)}}{(d^{(m)})^T A d^{(m)}} \quad (6.62)$$

The Conjugate Gradient algorithm steps are as follows:

1. Choose residual  $r^0$  and start iterating

$$d^{(0)} = r^{(0)} = b - A\phi^{(0)} \quad (6.63)$$

2. Choose factor  $\alpha$  in  $d$  direction, Equation 6.62
3. Calculate a new solution estimate  $\phi^{(m+1)}$ , Equation 6.61

4. Calculate the new residual

$$r^{(m+1)} = r^{(m)} - \alpha^{(m)} A d^{(m)} \quad (6.64)$$

5. Calculate conjugate residual coefficient  $\beta$

$$\beta^{(m)} = \frac{r^{(m+1)T} r^{(m+1)}}{r^{(m)T} r^{(m)}} \quad (6.65)$$

6. Calculate a new search direction

$$d^{(n+1)} = r^{(n+1)} + \beta^{(m)} d^{(m)} \quad (6.66)$$

The set of search path vectors  $d^{(0)}, d^{(1)}, \dots, d^{(n-1)}$  are orthogonal, it can be shown that the solution will be found after  $N$  steps where  $N$  is the size of a matrix [88]. In practice, less than  $N$  iterations are needed for an approximate solution.

### 6.8.2 Preconditioning and asymmetry

Preconditioning improves the convergence rate of the GC method. This is done by multiplying the original Equation 6.57 by the inverse of a preconditioned matrix  $P^{-1}$  as in the Equation 6.67

$$P^{-1} A \phi = P^{-1} b \quad (6.67)$$

The matrix  $P$  is defined such that the matrix  $P^{-1} A$  is better conditioned than matrix  $A$ . To guarantee symmetry, the Cholesky decomposition is used to represent  $P$  in the form:

$$P = L L^T \quad (6.68)$$

The system of equations is then expressed as:

$$L^{-1} A L^{-T} L^T \phi = L^{-1} b \quad (6.69)$$

Where  $L^{-1} A L^{-T}$  is a symmetric positive-definite matrix.

Bi-conjugate Gradient Method (BiCG) is a CG variant dedicated to non-symmetric matrix systems. The symmetric matrix has the same coefficients on both sides of the diagonal  $a_{ij} = a_{ji}$ . The matrix  $A$  can often be asymmetrical, which arises from discretising the convection term. For example, if the upwind scheme is applied, a contribution will be to the coefficient upstream to the face (i.e.  $a_{2,1}$ ) but not to the downstream of a face (i.e.  $a_{1,2}$ ) [54]. BiCG method converts the asymmetrical system to symmetrical, which allows then to

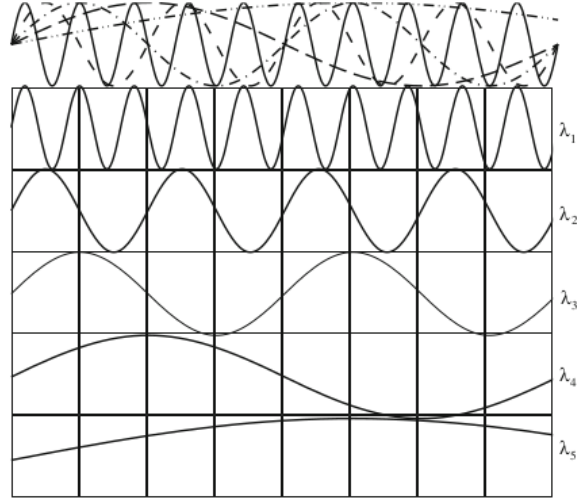


Figure 6.4. Different error modes in one-dimensional grid [87]

solve it with GC, Equation 6.70:

$$\begin{bmatrix} 0 & A \\ A^T & 0 \end{bmatrix} \begin{bmatrix} \hat{\phi} \\ \phi \end{bmatrix} = \begin{bmatrix} b \\ 0 \end{bmatrix} \quad (6.70)$$

Where  $\hat{\phi}$  is a dummy variable introduced to be able to convert the asymmetrical system to the symmetrical one. As a result, the second set of calculations for the coefficient matrix  $A^T$  is performed, and the computational cost will be approximately two times that of the CG method. Preconditioning can also be used with the BiCG method.

### 6.8.3 The Multigrid approach

The rate of convergence of iterative methods worsens as the size of the algebraic system expands, i.e. as the mesh is refined [135]. It has been demonstrated that the solution error has components with a range of wavelengths, which is schematically illustrated in Figure 6.4. Iterative approaches reduce the error components with short wavelengths. The long-wavelength components of the error are hardest to damp out and tend to decay very slowly. For the coarse mesh, all error components decrease very quickly because the longest possible error wavelength lies in the range of short wavelengths.

The multigrid method uses meshes with varying degrees of coarseness to develop a solution strategy. The first step solves the residual vector  $r$  and the matrix  $A$  on the original, finest mesh to the partial convergence ( i.e. when the residuals drop by a factor of 2). The solution is then transferred to the coarse mesh, and the error on this mesh will reduce rapidly. The error vector from the coarse mesh is transferred to the finest mesh, and linear interpolation is performed on the intermediate points in the fine mesh. The error vector is then used to correct the original error vector and solve for the corrected intermediate solution.

## 6.9 Under-relaxation

In order to improve convergence and stabilize the iteration process, a method called under-relaxation is introduced. The method reduces the amount that a variable changes during a solution step. During an iteration step value of the variable  $\phi_P$  changes from  $\phi_P^*$  from the previous iteration to the just calculated new value of  $\phi_P^{new}$ . Under-relaxation will reduce the change  $\delta\phi = \phi_P^{new} - \phi_P^*$  by a fraction  $\alpha$ . As a result, the value obtained at that solution step will be:

$$\phi_P = \alpha\phi_P^{new} + (1 - \alpha)\phi_P^* \quad (6.71)$$

Where  $0 < \alpha < 1$ , typical suitable under-relaxation factor lies in the range of 0.1-0.5 [140].

The central coefficient  $a_P$  and a new source term  $b_P$  in the under-relaxed form become:

$$a_P = \frac{a_P}{\alpha} \quad (6.72)$$

$$b_P = b_P + \frac{(1 - \alpha)}{\alpha} a_P \phi_P^* \quad (6.73)$$

## 6.10 Summary

This chapter summarizes the Finite Volume discretization model to solve the Navier-Stokes equations. It explains the methods implemented in the OpenFOAM toolbox for the FSI simulations. The convective and diffusive terms were discretized on the one-dimensional uniform grid for simplicity of explanation. The temporal discretization is available using the first order and second-order schemes. The resulting pressure-velocity coupled system was derived on the two dimensional, uniform, orthogonal grid. Two algorithms were described: SIMPLE, which will be applied to the initial steady-state simulations, and PISO, which is typically used for the transient simulations. The Rhie-Chow interpolation method for pressure-velocity coupling in co-located grid arrangement was presented. A brief discussion on the boundary constraints imposed in further simulations and the treatment of the near-wall region were discussed. The iterative procedures (Jacobi, Gauss-Seidel and conjugate gradient method) of solving the system of algebraic equations were reviewed, followed by a multigrid approach addressing their limitations.

Numerical methods for the elasticity equations will be derived in the following chapter.

# Chapter 7

## Discretization of the solid equations

This chapter describes the cell-centred finite volume discretisation of the linear elastic governing equation defined in Chapter 3. In the OpenFOAM container for FSI [131] discretization of governing equations follows the numerical approach, which was first proposed by Demirdžić and Muzaferija [43]. For the solid model, the discretisation procedure is the same as for the fluid model. The solution domain is divided into a set of control volumes. The integral form of the linear momentum equation, Equation 3.27, is then transformed from the surface integrals to the sum of face integrals. This chapter will present the application of finite volume linear stress analysis on a two-dimensional Cartesian mesh.

### 7.1 Finite Volume discretization

Consider the steady state, two-dimensional stress equilibrium equation 3.14. Assuming the body forces  $f_i$  to be negligible, the governing equation reduces to:

$$\rho_S \frac{\partial^2 u_i}{\partial t^2} + \frac{\partial \sigma_{ij}}{\partial x_j} = 0 \quad (7.1)$$

Integrating over a cell of a volume  $V$  and applying the Gauss divergence theorem gives:

$$\int_S \sigma_{ij} n_j dS = 0 \quad (7.2)$$

Where  $S$  is the enclosing surface of a control volume. The discretisation is performed on a control volume depicted in Figure 7.1.

The constitutive relations, Equations 3.26 for equilibrium of forces acting in the  $x$  direction are applied.

$$\sigma_{xx} = 2\mu \frac{\partial u}{\partial x} + \lambda \left( \frac{\partial u}{\partial x} + \frac{\partial v}{\partial y} \right) \quad (7.3)$$

Where  $u$  and  $v$  are the displacements in the  $x$  and  $y$  direction, respectively. The relation 7.2 for the east and west faces becomes:

$$\left[ \int_S \sigma_{xx} \right]_w^e = \underbrace{\int_{S_e} \left[ (2\mu + \lambda) \frac{\partial u}{\partial x} + \lambda \frac{\partial v}{\partial y} \right] dS}_{T_{xe}} - \underbrace{\int_{S_w} \left[ (2\mu + \lambda) \frac{\partial u}{\partial x} + \lambda \frac{\partial v}{\partial y} \right] dS}_{T_{xw}} \quad (7.4)$$

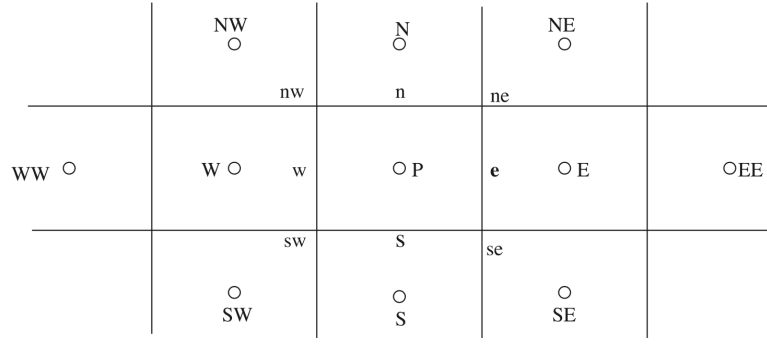


Figure 7.1. Two dimensional, Cartesian control volume [42]

After applying the strain-displacement equation, Equation 3.26b, the integration for the north and south cell faces becomes:

$$\left[ \int_S \tau_{xy} \right]_n^s = \underbrace{\int_{S_n} \left( \mu \frac{\partial u}{\partial y} + \mu \frac{\partial v}{\partial x} \right) dS}_{T_{xn}} - \underbrace{\int_{S_s} \left( \mu \frac{\partial u}{\partial y} + \mu \frac{\partial v}{\partial x} \right) dS}_{T_{xs}} \quad (7.5)$$

Applying the central differencing to the gradient of displacement, similarly to the diffusion terms in the fluid discretization equation, the terms  $T_{xe}$ ,  $T_{xw}$ ,  $T_{xn}$ ,  $T_{xs}$  are evaluated as:

$$T_{xe} = (2\mu + \lambda) \frac{u_E - u_P}{\delta x_e} S_e + \lambda \frac{v_{ne} - v_{se}}{\delta y_e} S_e \quad (7.6a)$$

$$T_{xw} = (2\mu + \lambda) \frac{u_P - u_W}{\delta x_w} S_w + \lambda \frac{v_{nw} - v_{sw}}{\delta y_w} S_w \quad (7.6b)$$

$$T_{xn} = \mu \frac{u_N - u_P}{\delta y_n} S_n + \mu \frac{v_{ne} - v_{nw}}{\delta y_n} S_n \quad (7.6c)$$

$$T_{xs} = \mu \frac{u_P - u_S}{\delta y_s} S_s + \mu \frac{v_{se} - v_{sw}}{\delta y_s} S_s \quad (7.6d)$$

The displacements at the vertices  $v_{ne}$ ,  $v_{nw}$ ,  $v_{se}$ ,  $v_{sw}$  are obtained by interpolation from the surrounding cell centres as described in the Section 7.2. The discretised equilibrium equation becomes:

$$(a_E + a_W + a_N + a_S)u_P - a_E u_E - a_W u_W - a_N u_N - a_S u_S = b_P \quad (7.7)$$

Where,

$$a_E = (2\mu + \lambda) \frac{S_e}{\delta x_e} \quad (7.8a)$$

$$a_W = (2\mu + \lambda) \frac{S_w}{\delta x_w} \quad (7.8b)$$

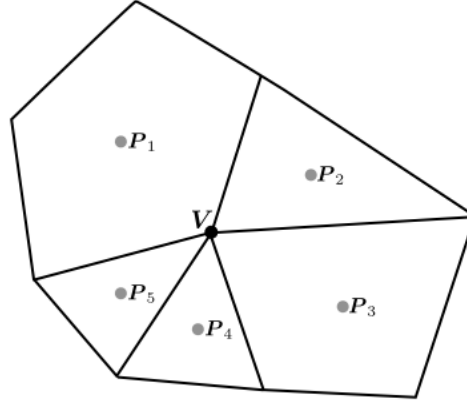


Figure 7.2. Vertex  $V$  surrounded by cell centres  $P_i$  [19]

$$a_N = \mu \frac{S_n}{\delta y_n} \quad (7.8c)$$

$$a_S = \mu \frac{S_s}{\delta y_s} \quad (7.8d)$$

$$b_P = \lambda \frac{v_{ne} - v_{se}}{\delta y_e} S_e - \lambda \frac{v_{nw} - v_{sw}}{\delta y_w} S_w + \mu \frac{v_{ne} - v_{nw}}{\delta x_n} S_n - \mu \frac{v_{se} - v_{sw}}{\delta x_s} S_s \quad (7.8e)$$

and  $b_P$  are the source terms treated explicitly, determined by using the values from the previous iteration - it is further explained in Section 7.5.

## 7.2 Vertex interpolation

When using a Lagrangian approach, the mesh is moved, and stress fields are updated to the new configuration at the end of each time step. To move the mesh, the displacements at the cell centres must be interpolated to the cell vertices. In OpenFOAM, this is done by using the *inverse distance interpolation method*. To illustrate the concept, Figure 7.2 is introduced. The value is known at cell-centres  $P_i$ . A weighted average of a variable at vertex  $\phi_V$  is found as:

$$\phi_V = \frac{\sum_{i=1}^P \omega_{P_i} \phi_{P_i}}{\sum_{i=1}^P \omega_{P_i}} \quad (7.9)$$

Where  $\phi_{P_i}$  is the value at the neighbour cell centre  $P$ , and there are  $P$  neighbouring cell centres. The weighting factor,  $\omega_{P_i}$ , is given by:

$$\omega_{P_i} = \frac{1}{|r_V - r_{P_i}|} \quad (7.10)$$

Where  $r_V$  is the vertex position vector and the  $r_{P_i}$  is the cell centre position vector. For the



grid presented in Figure 7.1, i.e for a vertex  $ne$ , the interpolation will be simplified as:

$$u_{ne} = \frac{1}{4}(u_P + u_E + u_N + u_{NE}) \quad (7.11)$$

### 7.3 Temporal discretisation

The time discretisation is performed using the first order implicit order scheme, described in Section 6.4.1. As in the discretisation of the fluid solver, the time derivative of a variable  $\phi$  at the cell centre  $P$  is defined as:

$$\left(\frac{\partial \phi_P}{\partial t}\right)^{[m]} = \frac{\phi_P^{[m]} - \phi_P^{[m-1]}}{\delta t} \quad (7.12)$$

Where superscript  $[m]$  indicates the current time increment and  $[m - 1]$  indicates the previous time increment. For the solid solver, the rate of change of  $\phi_P$  for a control volume is:

$$\frac{\partial}{\partial t} \int_V \frac{\partial \phi_P}{\partial t} dV = \frac{1}{\delta t} \left[ \rho_S \Delta V \left( \frac{\partial \phi_P^{[m]} - \partial \phi_P^{[m-1]}}{\delta t} \right) \right] \quad (7.13)$$

The final discretized temporal term is derived by substituting the Equation 7.12 to the Equation 7.13

$$\frac{\partial}{\partial t} \int_V \frac{\partial \phi_P}{\partial t} dV = \frac{1}{\delta t} \left[ \rho_S \Delta V \left( \frac{\phi_P^{[m]} - 2\phi_P^{[m-1]} + \phi_P^{[m-2]}}{\delta t} \right) \right] \quad (7.14)$$

All terms in Equation 7.7 are evaluated at the new time instance  $t^{[m]} = t^{[m-1]} + \delta t$ . The discretisation is bounded but first-order accurate in time. Thus it can cause some numerical dissipation when the time step is not small enough.

The remedy would be to construct the second-order accurate scheme using three 'old' time levels [66]:

$$\frac{\partial^2 \phi_P}{\partial t^2} = \frac{2\phi_P^{[m]} - 5\phi_P^{[m-1]} + 4\phi_P^{[m-2]} - \phi_P^{[m-3]}}{\delta t^2} \quad (7.15)$$

Where  $\phi_P^{[m-3]} = \phi_P(t - 2\delta t)$ . As a result, the scheme is nominally more accurate, but it can be unbounded, leading to unphysical stress peaks in the solution [66]. Even though the second-order scheme will converge faster than the first order, small artificial stress peaks can lead to a misleading interpretation of the flow-induced vibration. The first-order accurate scheme with relatively small time steps was also the preferred method in linear elasticity simulations in [66].

### 7.4 Boundary conditions

The solution of the solid model is completed by setting the boundary conditions. The boundary conditions of the following types (time-varying or constant) were used in the numerical

modelling of a solid structure for the FIV study:

- fixed displacement
- fixed traction
- free surfaces - zero traction

The solution displacement can then be applied to set the distribution of stresses or any other variables of interest.

Dirichlet boundary condition sets the value of displacement  $u_b$  at the centre of the boundary face  $\phi_b$ . The boundary face value is then substituted into the displacement gradient computation in Equation 7.6. Figure 7.3 with a control volume next to a boundary is provided to explain the implementation of the fixed displacement boundary condition. In this case the displacement  $u_E$  in the term  $T_{xe}$  (Equation 7.6a) is substituted with the known value of  $u_B$ . When the traction is given, normal gradient  $t_{Bx}$  can be directly substituted into Equation 7.6a, term  $T_{xe}$  becomes:

$$T_{xe} = t_{Bx} S_e \quad (7.16)$$

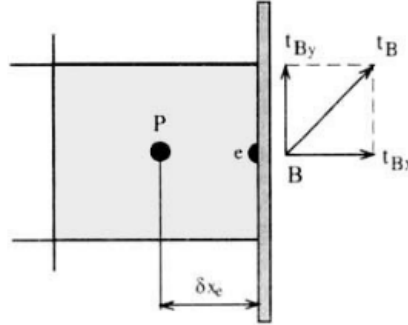


Figure 7.3. Cartesian CV next to a boundary [43]

## 7.5 Solution procedure

The discretised solid model in Equation 7.7 is assembled for all control volumes with a final form expressed as:

$$[A][u] = [b] \quad (7.17)$$

Where  $[A]$  is a sparse matrix of coefficients  $a_P$  on the diagonal,  $[u]$  is the vector of cell-centre displacements and  $[b]$  is the source vector. The system of linear algebraic equations is solved using the segregated algorithm described in [17, 18, 131]. It requires that the displacement vector  $u$  is temporally decomposed into three components and solved iteratively. Then outer iterations are performed explicitly to re-couple the momentum equation, where the right-hand side vector  $b$  is updated using the displacement vector increment from the previous iteration. The sparse matrix  $A$  is symmetric and weakly diagonally dominant [131].

The system of Equations 7.17 can be solved with preconditioned gradient method introduced in Section 6.8.1 or with the geometric agglomerated algebraic multigrid solver (GAMG), which concept is introduced in Section 6.8.3.

## **7.6 Summary**

This chapter summarises the Finite Volume discretisation procedure developed to solve the Navier-Displacement equation. All methods used in the OpenFOAM toolbox for the FSI simulations were presented. The solver applies a second-order central differencing scheme for spatial discretisation of conservation of linear momentum. First-order and second-order temporal discretisation methods are available and have been reviewed. Finally, a brief discussion on boundary conditions used in further simulations and the solution methods of the linearised system of equations were presented.

In the following chapter, the information on the numerical methods from the two preceding chapters is applied to the simulations.

# Chapter 8

## Simulation results

The following Chapter describes the development of FIV benchmark simulation of the cylindrical cantilever beam subjected to the axial turbulent flow that has been performed. The process of selecting valuable test cases is described in Methodology. Then successive test cases with conclusions that lead to the final modelling approach are presented. Finally, the full 3D model corresponding to the geometry and flow velocity in the experiment from [26] is presented. This final model will be serving as a benchmark for turbulence-induced vibrations.

### 8.1 Methodology

A detailed analysis of FIV mechanisms presented in Section 1.3 shows that the fuel rod in the Fuel Assembly component will be subjected to turbulent buffeting and coupling effects induced by neighbouring fuel rods. Based on this and the conclusions from Section 5.1.1 strongly coupled modelling approach was selected in further study.

The primary aim of this PhD project has been to present a fully validated benchmark simulation of the flow-induced vibration of a free-clamped cylinder exposed to axial turbulent flow, which can inform future studies on PWR fuel bundles. The investigation takes the form of a case study of the following simulation test cases:

- Validation of the FSI methodology against a well-known FSI benchmark case [132]
- Assessment and evaluation of the URANS effective viscosity ( $k-\omega$ ,  $k-\varepsilon$ ,  $k-\omega$  SST) and Reynolds Stress models on a suitable representative 2D test case with rigid walls [15]
- Free vibration of the blunt-end rod in vacuum
- Two-way FSI simulations validated against the experimental data [26].

A case-study approach was chosen to develop a cost-effective URANS modelling methodology for flow-induced vibration of cylindrical structures in axial flow, validated against the experimental data obtained with a free-clamped cylinder by [26]. In order to achieve this objective, it is first necessary to assess and evaluate the suitability of URANS models

(namely, the effective viscosity models,  $k-\omega$ ,  $k-\varepsilon$ ,  $k-\omega$  SST and Reynolds Stress Models LRR and SSG) to effectively reproduce fluctuating forces which can induce vibrations, because turbulent buffeting is a key source of excitation for cylindrical structures in axial flow. A suitable representative 2D test case with rigid walls [15] was chosen for this purpose.

In all models, the high-Reynolds-number approach with the wall functions has been adopted. The Low-Reynolds models with finer mesh resolution at the near-wall region have not been considered in this study for two reasons:

- To reduce the computational effort in future FSI simulations in the PWR rod bundle, example of which can be found in [29, 141]. The requirement of  $y^+ < 2$  could be challenging for such a complex geometric structure.
- Reynolds number (based on cooling channel hydraulic diameter in the fuel lattice) during PWR normal operating conditions is of the range of  $\sim 5 \times 10^5$  [26, 27]. High-Reynolds approach for reproducing the flow conditions in the core and around the fuel assembly is thus justified in [137, 141].

The FSI *solids4foam* toolbox developed for OpenFOAM [16] is based on the cell-centered finite volume discretization method for both, fluid and solid governing equations and strongly coupled iteration scheme. Having the single, self-contained toolbox minimize the errors on loads transfer from the fluid boundary face to the solid boundary faces and reverse. This makes it suitable for simulating small-amplitude, turbulence-induced vibrations. Prior to commencing the study, the validation of the FSI numerical modelling methodology against a laminar test case with in benchmark case [132] has been done.

In the partitioned approach, the fluid domain and solid domain are solved separately, therefore a separate simulation of a freely vibrating rod in vacuum was necessary to establish the solid side settings.

Finally, the knowledge gained from the preceding numerical explorations is brought together and directed to the simulation of turbulent flow-induced vibrations exerted on a single rod subjected to axial flow. This final two-way FSI simulation serves as benchmark simulation for the Flow-Induced Vibration phenomena in nuclear industry.

## 8.2 Laminar FSI Analysis: Validation of the FSI methodology

The elastic plate located behind the rigid cylinder schematically represented in Figure 8.1 is a well-known benchmark FSI case [132] against which the present FSI methodology has already been tested [131]. Besides validating the implementation of the FSI methodology, this test case was also informative in selecting a linear variation of the diffusion coefficient with the distance from the boundary in the mesh deformation equation (Equation 5.14).

Figure 8.1 presents the computational domain with structural details for the elastic plate. The flow over the cylinder leads to vortex shedding, and this causes oscillatory lift and drag

Property	Value
Fluid density $\rho_F [kgm^{-3}]$	$10^3$
Fluid kinematic viscosity $\nu_F [m^2s^{-1}]$	$10^{-3}$
Mean inlet velocity $\bar{u} [ms^{-1}]$	2
solid density $\rho_S [kgm^{-3}]$	$10^3$
Young's modulus $E_S [Pa]$	$5.6 \times 10^6$
Poisson's ratio $\nu_S [-]$	$4 \times 10^{-2}$

Table 8.1. Fluid and solid properties in the FSI laminar simulation

forces acting on the elastic plate (flag). Displacements are tracked at the plate tip's control point (A).

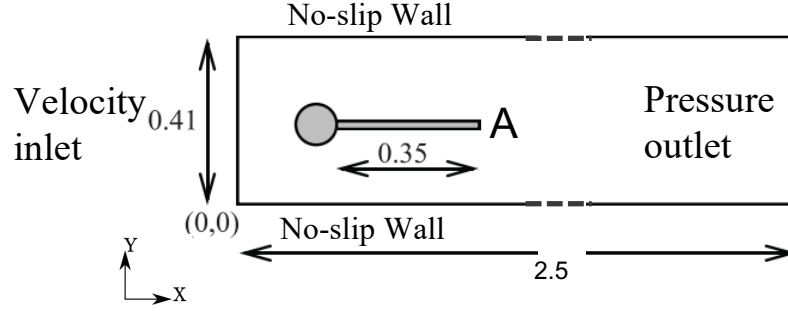


Figure 8.1. Computational domain of the FSI laminar flow test. All dimensions are in meters [131].

The fluid enters the channel from the left-hand side with a parabolic velocity profile, which is expressed in Equation 8.1.

$$u(y) = 1.5\bar{u} \frac{4}{0.1681} y(0.41 - y) \quad (8.1)$$

The flow is assumed to be laminar ( $Re=200$  based on cylinder diameter). The structure is assumed to be elastic and compressible. Deformation of the elastic flag is described by a hyper-elastic material model allowing large deformations introduced in Section 3.5. Fluid and solid properties and mean inlet velocity  $\bar{u}$  for the elastic plate behind a rigid cylinder are summarized in Table 8.1. Constant pressure is imposed at the channel outlet, and a no-slip boundary condition is applied to the walls. The numerical solution is obtained with the time step  $\Delta t = 10^{-3}s$ . The coupling is activated after 2s. The periodic motion of the plate was achieved at 3.5 seconds.

The grid convergence study used three different meshes on the fluid side, namely: fine 1 ( $\sim 21 \times 10^3$  cells), fine 2 ( $\sim 85 \times 10^3$  cells) and fine 3 ( $\sim 340 \times 10^3$  cells). The solid side mesh was fixed at 2500 cells. For the 'fine 1' case, the diffusion coefficient varies quadratically with distance from the boundary  $\gamma(l) = l^{-2}$  while in the case 'fine 2' and fine 3' the linear function for diffusivity is applied  $\gamma(l) = l^{-1}$ .

Figure 8.2 depicts the simulation snapshot with details of the mesh. An example of a 'fine 2' deformed mesh at a maximum deflection of a beam is presented in Figure 8.2c. Meshes on the solid and fluid sides are non-conformal, as depicted in Figure 8.2b. It can be observed that the computational mesh is ideally adjusted to the shape of a deflected beam, and

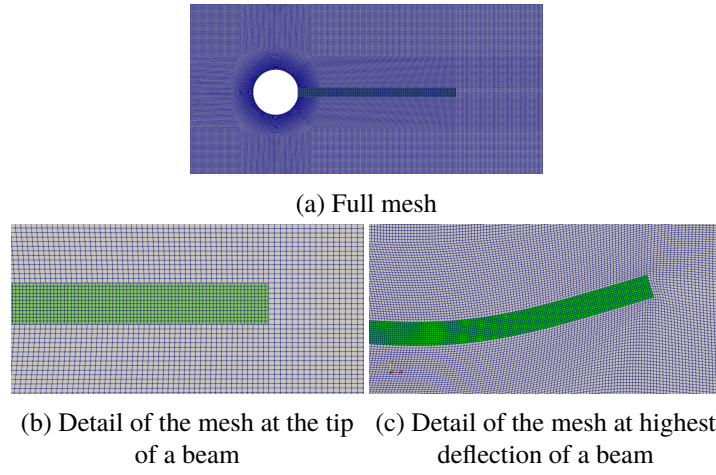


Figure 8.2. Example of the 'fine2' fluid mesh (grey) and solid mesh (green) used for the validation study

the mesh quality is preserved during the motion.

The results of the validation study are summarized in Table 8.2. The frequency has been determined from a 2.5-seconds long displacement time series via the Fast Fourier Transform. Data were analyzed after an initial 3.5 seconds required to reach a periodic motion of a plate. The frequency bandwidth is 0.4Hz. It is evident in Table 8.2 that the calculated frequencies are in good agreement with the benchmark frequencies, therefore validating the present FSI implementation. The validation is additionally supported by plots of displacements over the full period of oscillation as presented in Figures 8.3a-8.3b. The mean and amplitude value are computed from the last period of oscillations as suggested by the benchmark authors. The amplitude error for the x-displacement is 7%, but the mean value is only 0.3% higher than that of the benchmark. The mean of the y-displacement is underestimated by about 7%, but the amplitude is only marginally higher than that of the benchmark.

Forces exerted by the fluid are calculated on the whole submerged body (cylinder and flag). Results of the temporal variation in the lift and drag force exerted on the body are visualized in Figure 8.4. The quantitative difference between the calculated and the reference benchmark results are summarized in Table 8.3. As the mesh is refined, the amplitude of the drag force is estimated with an error of 7%, and the amplitude of the lift with an error of 13% in comparison to the reference value. The calculated frequencies are in good agreement with reference values, approximately with the error of 2% for the frequency of drag and 0.5% for the frequency of lift. The mean value of drag is only 0.3% higher than that of the reference. The mean lift force resulting from the simulation is two times higher than that of the benchmark. However, the mean value in the referenced benchmark is determined as  $mean = 0.5(max + min)$ . Therefore it is difficult to determine the mean when its value is close to zero. Careful investigation of Figure 8.4b shows that the plot of lift variation is in good agreement with the benchmark reference.

Case	$\bar{d}_x$ [10 <sup>-3</sup> m]	$A_x$ [10 <sup>-3</sup> m]	$f_{Nx}$ [Hz]	$\bar{d}_y$ [10 <sup>-3</sup> m]	$A_y$ [10 <sup>-3</sup> m]	$f_{Ny}$ [Hz]
Fine 1	-2.71	2.60	10.8	1.47	33.90	5.6
Fine 2	-2.86	2.73	10.8	1.41	34.90	5.6
Fine 3	-2.86	2.74	10.8	1.39	34.94	5.6
Turek and Hron [132]	-2.85	2.56	10.9	1.53	34.35	5.3

Table 8.2. x- and y-displacement of the control point A versus the FSI benchmark. Data are denoted as: mean  $\bar{d}$ , amplitude  $A$  and frequency  $f_N$

Case	Mean Drag $\bar{F}_D$ [N]	$A_D$ [N]	$f_D$ [Hz]	Mean Lift $\bar{F}_L$ [N]	$A_L$ [N]	$f_L$ [Hz]
Fine 1	461.2	27.7	10.0	4.2	169.7	5.5
Fine 2	460.4	28.8	10.0	4.01	171.8	5.5
Fine 3	461.4	29.7	10.0	4.92	175.3	5.5
Turek and Hron [51]	460.2	27.7	10.9	2.47	154.8	5.47

Table 8.3. Lift and drag force on the cylinder and flag versus the FSI benchmark. Data are denoted as: mean lift force  $\bar{F}_L$ , mean drag force  $\bar{F}_D$  amplitude  $A$  and frequency  $f_N$

### 8.2.1 Conclusions

This section presented the laminar test case, which allows to quickly confirm that the selected partitioned, two-way FSI solver is appropriate for further investigations. The choice of mesh deformation method is a key factor influencing the amplitudes of deflections. A mesh displacement based on Laplacian smoothing is relatively cheap but does not maintain high mesh quality during high rotation angles, or large deformation [67, 69]. The axial flow-induced vibrations of interest here are characterized by relatively small deformations, similarly to the present benchmark with the 'fine 2' and 'fine 3' cases, so that a diffusion coefficient varying linearly with the distance from the moving walls was deemed appropriate.

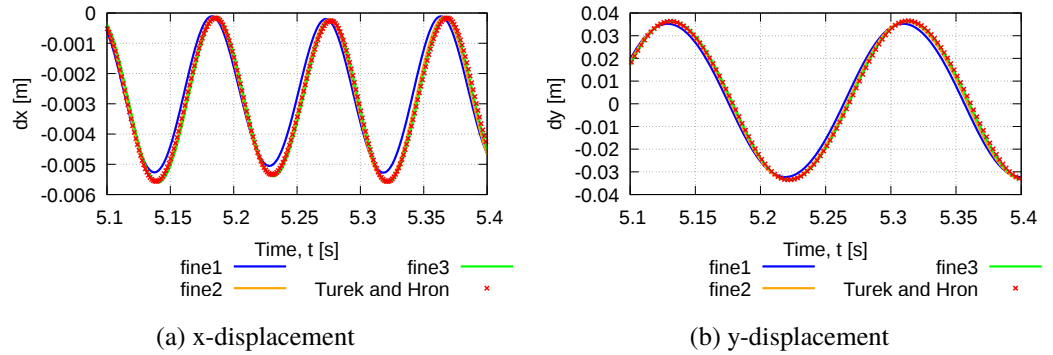


Figure 8.3. Displacement history of a control point A



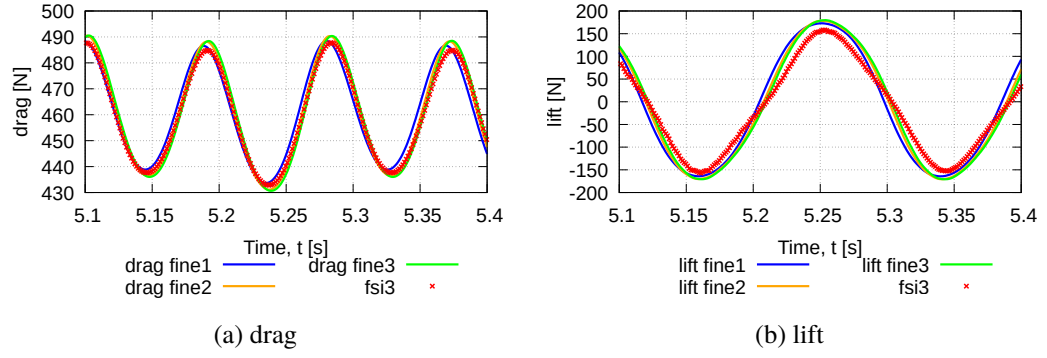


Figure 8.4. Lift and drag force on the cylinder+flag

### 8.3 Rigid body: Analysis of the turbulence models

The purpose of the following numerical explorations has been to demonstrate the effectiveness of various turbulence models in reproducing large-scale flow oscillations. The chosen URANS model are: EVM ( $k - \omega$ ,  $k - \varepsilon$ ,  $k - \omega$  SST) and Reynolds Stress (SSG, LRR) models. The study also involves the assessment of second-order and third-order discretisation convection schemes.

The experimental benchmark selected for use here is provided by Camussi [15], who investigated the wall pressure fluctuations generated by shear flow separated at the edge of a forward-facing step with the simultaneous PIV visualisation. Experiments were performed at a Reynolds number  $Re_h = 2.6 \times 10^4$  based on the step height  $h$ , and free stream velocity  $U_0 = 1.5m/s$ . They demonstrated that the pulsating motion of the recirculation bubble that forms at the step causes high energy and low-frequency pressure oscillations, characterised by a Strouhal number of around  $St = 0.1 - 0.2$  (7.5Hz-15Hz).

The schematic of the computational domain with all dimensions is depicted in Figure 8.5. The inlet height, the step location and the entire length of the channel are scaled in relation to the step height  $h$ , which equals 20 mm. As investigated in the experiment, the unsteady recirculation bubble is formed at the step's reattachment region. In this case for the location  $x/h < 2.1$  and at the vertical side of the step at  $y/h \sim 0.5$ . In the present simulations, a no-slip boundary condition is applied for the top and bottom walls and the forward-facing obstacle, and fully developed flow conditions are applied at the inlet.

In order to generate a fully developed flow at the channel entrance, an initial simulation with the use of the steady-state solver for incompressible, 1D turbulent flow was carried out [95]. The solver is specifically designed to create fully developed velocity and turbulence inflow conditions. An average target velocity of  $1.5m/s$  was specified, and the pressure gradient drives the flow until fully developed conditions with the required bulk velocity are reached. The resulting profile is then mapped to the inlet of the channel.

The grid close to the forward-facing step is depicted in Figure 8.6. The mesh consists of  $\sim 200,000$  uniform hexahedral cells, and it is orthogonal. The cell size was chosen to ensure that the dimensionless wall distance of the near-wall node at the inlet,  $y^+$ , has a value of 30,

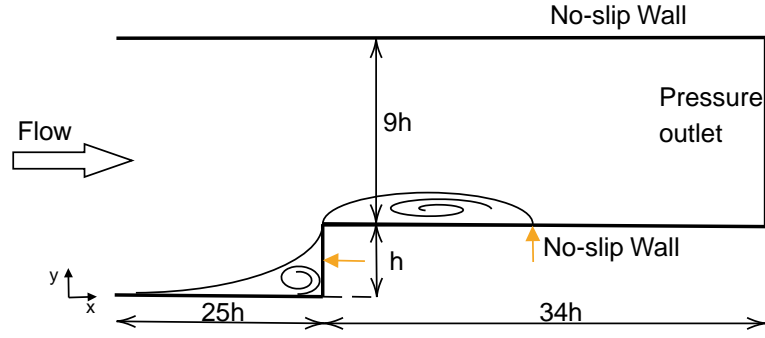


Figure 8.5. Schematic diagram of a 2D forward-facing step Orange arrows indicate the separation point downstream the step (at  $x/h \sim 2.1$ ) and upstream the step (at  $y/h \sim 0.5$ )

which is consistent with the use of wall functions. As indicated by the red cones, pressure probes close to the wall were placed at the  $x$ -locations before the step and after the step. The distance between pressure probes was fixed to  $0.75h$ , corresponding to the location of pressure transducers in the experiment. The time step  $\Delta t = 5 \times 10^{-5} s$  has been adopted to maintain the Courant number below 0.1 and capture all flow instabilities. The pressure has been sampled at each time step for a total duration of 10 seconds. The Second Order Euler Scheme (SOUE) [87] for temporal discretisation has been adopted.

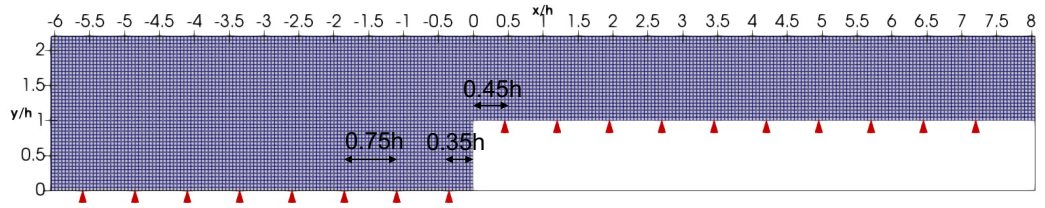


Figure 8.6. Mesh grid used for the validation of turbulence models. Red arrows indicate the location of the pressure probes for the wall pressure measurements.

The first set of investigations aimed to determine the suitable discretisation of the convection scheme. First-order and second-order accurate Upwind schemes and the third-order QUICK scheme have been tested. Figure 8.7 shows the pressure fluctuation history right next to the reattachment length over the last 4 seconds of the simulation, using the  $k - \omega$  model. The pressure fluctuation coefficient is computed by subtracting the mean pressure  $\bar{p}$  from the instantaneous pressure  $p'$  and then by normalising with the specific kinetic energy of the inflow, as indicated in the Equation 8.2:

$$C_p = \frac{p' - \bar{p}}{0.5\rho_F U_0^2} \quad (8.2)$$

Not surprisingly, as shown in Figure 8.7, the first and second-order upwind schemes do not capture any pressure variation and are therefore not suitable for the prediction of the pressure fluctuations. On the other hand, the third order QUICK scheme resulted in the prediction of pressure fluctuations sufficiently strong for further processing. Careful investigation of the residuals showed that the result was physical and unrelated to numerical oscillations. The third-order QUICK scheme was therefore adopted for the discretisation of the convec-

tive terms of the transport equations of all EVM models. In the case of the stress transport models, like the LRR and SSG, the use of the QUICK scheme, which is not bounded, results in numerical instabilities. To achieve stability of the schemes, the  $k$ ,  $\varepsilon$  and Reynolds stress fields were discretised with the TVD limited linear differencing scheme (*limitedLinear* described in [83, 96]).

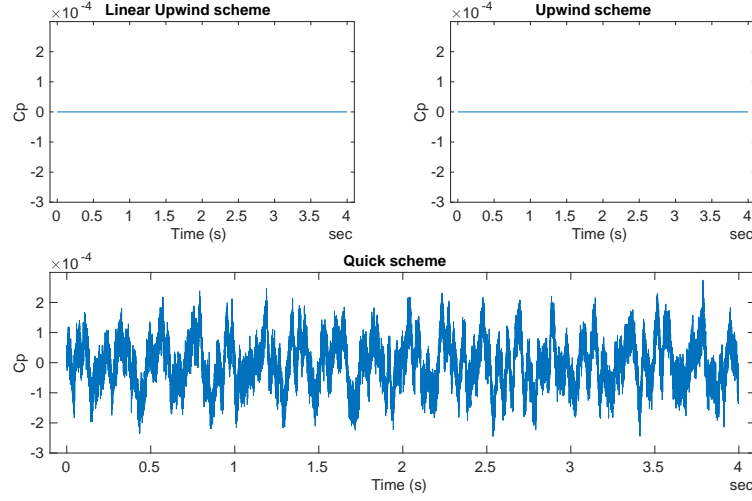


Figure 8.7. Pressure fluctuations sampled at  $x=1.95h$ ,  $k-\omega$  model. Top: first order Upwind and the second order upwind. Bottom: QUICK scheme

The further analysis focuses on the comparison between the statistics of wall pressure fluctuations along the channel observed in the experiment and those resulting from the URANS computations. The root mean square pressure coefficient  $C_{prm.s}$  defined in Equation 8.3 has been examined.

$$C_{prm.s} = \frac{\sigma_p}{0.5\rho_F U_0^2} \quad (8.3)$$

Here  $\sigma_p$  is the standard deviation of pressure,  $\rho_F$  is the fluid density, and  $U_0$  is the inlet velocity (1.5m/s). Figure 8.8 depicts the instantaneous pressure signal at the reattachment length ( $x/h = 1.95$ ) for selected URANS models. The SSG model and LRR provided nearly the same pressure signal. Therefore only the LLR model is depicted for clarity. From the graph, we can observe that the amplitude of the pressure signal calculated by the Reynolds Stress models is four orders of magnitude higher than that of the EVM models. This is further confirmed in Figure 8.9 where the evolution of the wall pressure fluctuations ( $C_{prm.s}$ ) are compared with the experimental data. From Figure 8.9, it is evident that the largest pressure fluctuations occur right downstream of the step, with a maximum value at the reattachment length at around  $x/h = 2$ , which is consistent with the experimental data.

From the comparisons of Figure 8.9, it is apparent that the Reynolds Stress models are able to predict pressure fluctuations of the same magnitude range as those of the experiment. Moreover, the sharp increase in the amplitude of  $C_{prm.s}$  at the reattachment point is also reproduced by the two Reynolds stress transport models. For the eddy viscosity models, the amplitude of pressure fluctuations is from two to four orders of magnitude lower than those in the experiment, but the steep rise in the amplitude of pressure fluctuations at the leading edge of a step is captured.

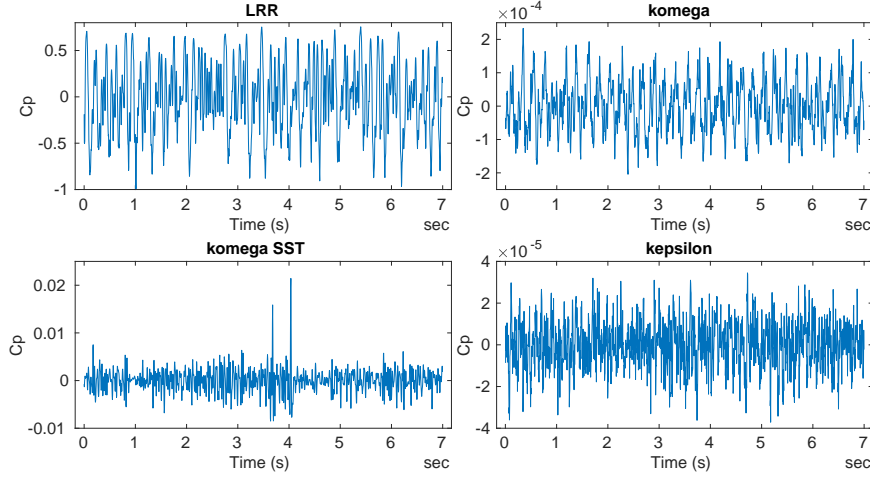


Figure 8.8. Pressure fluctuations sampled at  $x=1.95h$ , Top: RSM- LRR and  $k - \omega$  model. Bottom:  $k - \omega$  SST and  $k - \epsilon$

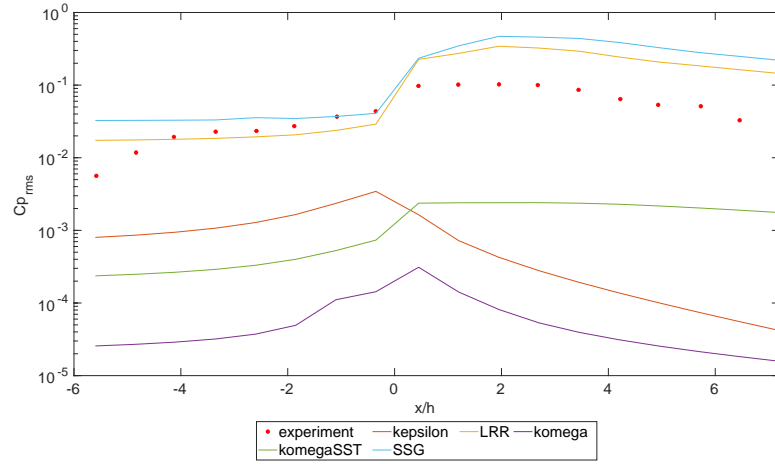


Figure 8.9. Evolution of the  $Cp_{rms}$  in terms of non-dimensional distance from the step

Figure 8.10 shows the instantaneous flow fields for the selected model, which clearly indicate that the Reynolds Stress models capture the flow's large eddy oscillations. The video presenting the motion of recirculation bubble that forms at the step and moves further downstream the step is included in reference [120]. The two Reynolds Stress models also show stronger large-scale instabilities, large scale vortices are continuously shed from the corner. These stronger flow instabilities in the predictions of the stress models are consistent with the stronger pressure fluctuations predicted by these two models in Figure 8.9. The EVM models, on the other hand, show a separation bubble downstream of the corner, with the SST returning a far larger region of flow separation. The reattachment length was established by analysing the time-averaged velocity fields. Both  $k - \omega$  and  $k - \epsilon$  models predict the separation with good accuracy. With the  $k - \omega$  SST model, the reattachment length is two times greater than that of the experiment. Similar findings were already reported in [108] where the validation of the  $k - \omega$  SST model was investigated. This model can underestimate the turbulent velocity scale near the wall, which in turn underestimates the turbulent eddy viscosity, thereby explaining why the reattachment length is over-predicted. For the Reynolds Stress models, the separation is overestimated by around 60%. A full discussion of the over-prediction of the separation lies beyond the scope of this study.

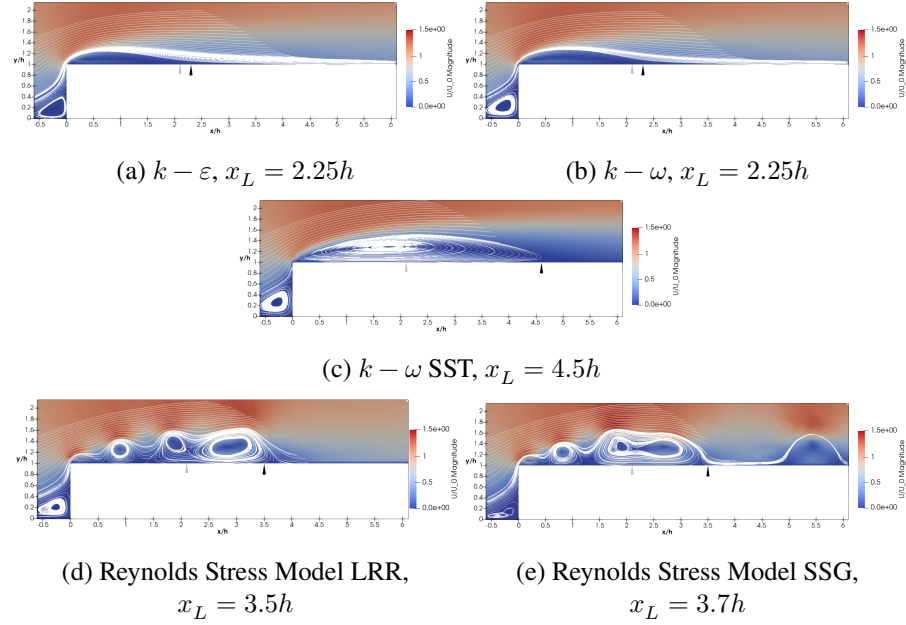


Figure 8.10. Flow patterns for different URANS models at time  $t = 9.9s$ . The black arrow indicates the reattachment length  $x_L$  from the simulation. The grey arrow indicates the reattachment length from the experiment  $x_{L,exp} = 2.1h$

Another highly informative comparison is that of the spectral distribution of the pressure fluctuations right after the step ( $x=0.45h$ ) and at the reattachment length where the pressure fluctuations amplitude is the highest ( $x=1.95h$ ), which is presented in Figures 8.11 and 8.12 respectively. Following on from the preceding pressure statistics comparisons, here, the attention is confined to the assessment of how the LRR model and EVMs perform in comparison to the experimental data. Frequency spectra are plotted against the Strouhal number ( $St = fh/U_0$ ) based on the free-stream velocity  $U_0$  and the step height  $h$ . As shown in Figure 8.11, the behaviour of the pressure PSD for the LRR scheme matches well the experimental results. Four dominating peaks at around 4Hz, 5.6Hz, 6.71Hz, and 8.29Hz are identified. For the  $k - \omega$  scheme, one clear dominating peak at around 4.72Hz is identified for all locations. The amplitude is of three orders of magnitude lower, which is consistent with the  $C_{prms}$  trend. Similarly, for the  $k - \omega$  SST two adjacent peaks at 5.42Hz and 6.29Hz after the step are identified. Their amplitude is of two orders of magnitude lower than that of the experiment. The PSD for the  $k - \varepsilon$  has not revealed any dominating peaks at either location and has not been depicted in the figure for clarity.

The PSD for the locations further downstream the step at  $x/h=2.7$  and  $x/h=6.45$ , beyond the reattachment length are depicted in Figures 8.13 and 8.14 respectively. The most interesting aspect of the graphs is that the pressure amplitude peaks found right after the step are reproduced further downstream. In the case of the LRR scheme, the pressure amplitude peaks at frequencies 4.14Hz and 6.71Hz are observed at all locations downstream of the step. The amplitude of the pressure peak at location  $x/h= 2.7$  is of two orders of magnitude higher than that of the experiment. This is, however, consistent with the pulsating motion of the recirculation bubble that forms at the step and  $C_{prms}$  trend. The more surprising correlation is with the  $k - \omega$  SST and  $k - \omega$  models, where the dominating peaks at 4.14Hz, 5.42Hz and 6.29Hz formed at the leading edge of a step transverse further downstream. The cor-

relations are related to  $C_{prm s}$  trend (Figure 8.9), but they are not directly visible from the observation of flow patterns in Figures 8.10b, 8.10c.

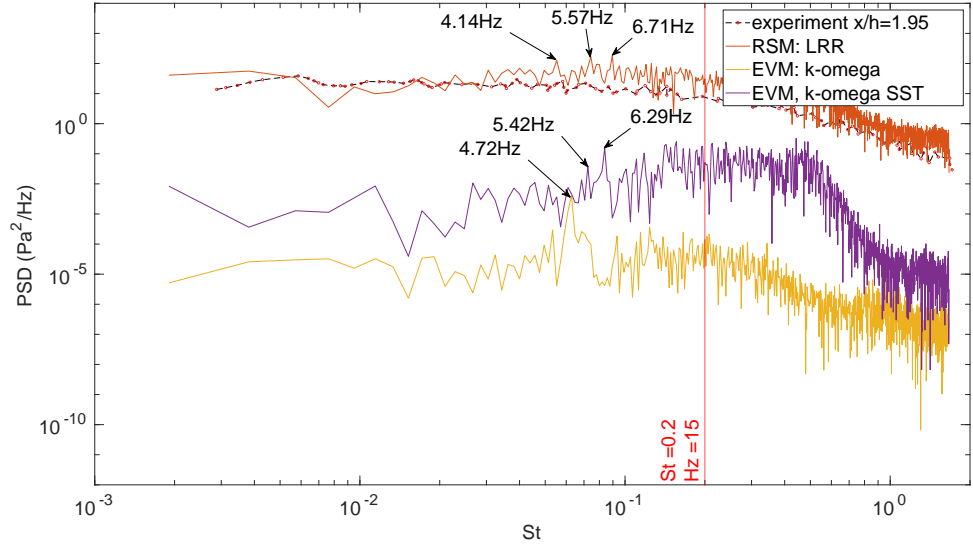


Figure 8.11. PSD for the LRR Reynolds Stress Model,  $k - \omega$  and  $k - \omega$  SST at  $x=1.95h$  compared to experimental results. The red line indicates the limit for high energy pressure oscillations (15Hz). Arrows indicate dominating frequency peaks

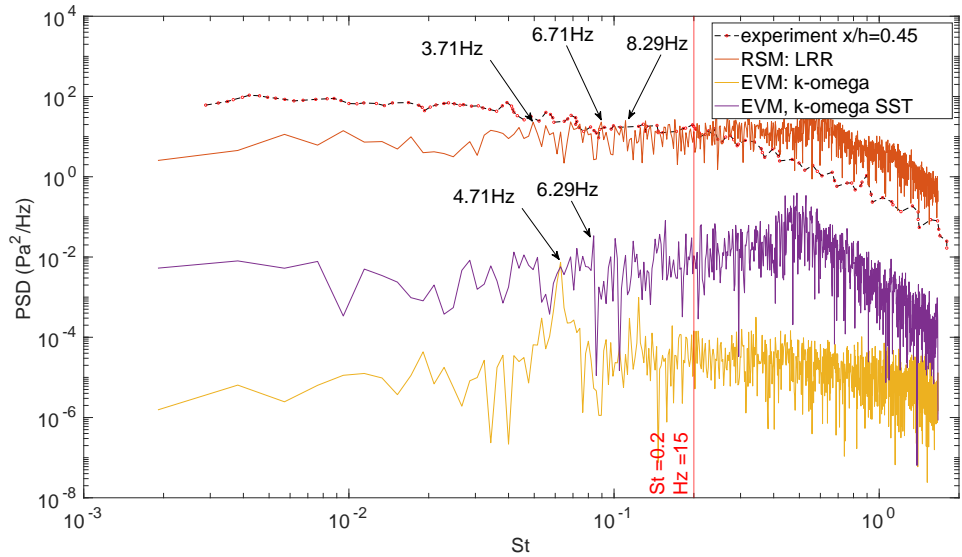


Figure 8.12. PSD for the LRR Reynolds Stress Model,  $k - \omega$  and  $k - \omega$  SST at  $x=0.45h$  compared to experimental results. An indication is the same as in the Figure 8.11

Further analysis of data is presented in the form of comparisons of the Probability Density Functions (PDF) obtained for pressure signals upstream and downstream of the step for the LRR scheme and those of the experiment (Figure 8.15). The random fluctuations were normalised to have zero mean and unitary standard deviation. In the experiment, the departure from the Gaussian distribution was reported for upstream and downstream the step. From the LLR simulation, it can be seen that PDF shapes are also affected by the flow conditions. The predicted pressure fluctuation peaks will have the same statistical distribution as those



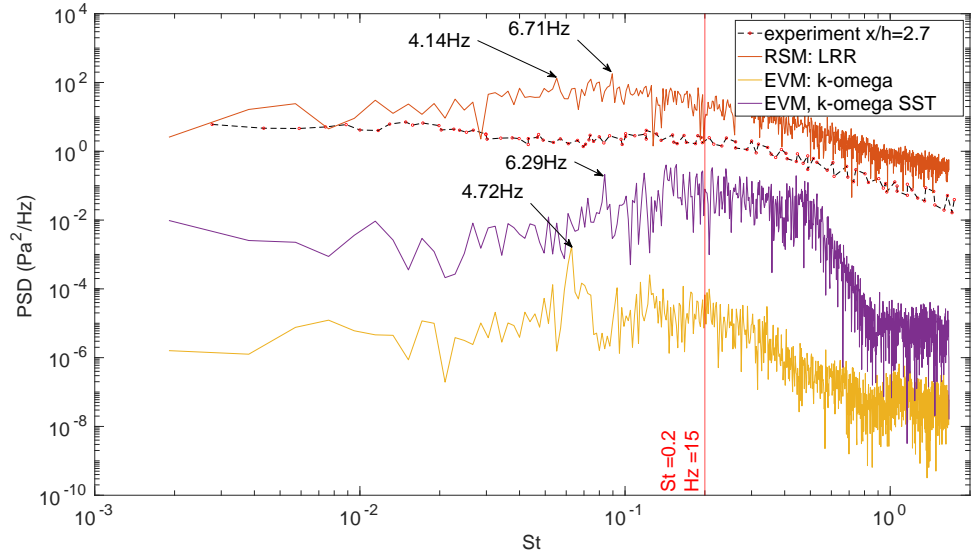


Figure 8.13. PSD for the LRR Reynolds Stress Model,  $k-\omega$  and  $k-\omega$  SST at  $x=2.7h$  compared to experimental results. An indication is the same as in the Figure 8.11

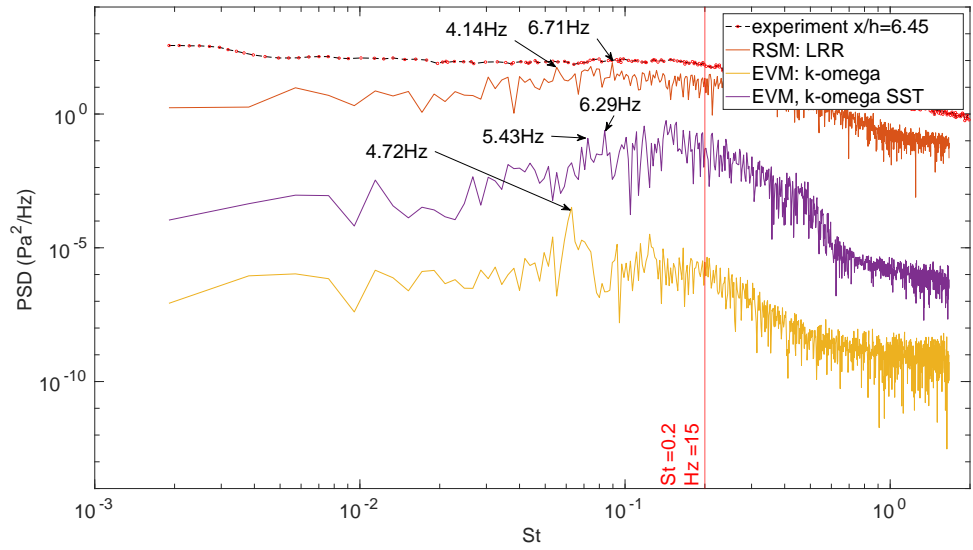


Figure 8.14. PSD for the LRR Reynolds Stress Model,  $k-\omega$  and  $k-\omega$  SST at  $x=6.45h$  compared to experimental results. An indication is the same as in the Figure 8.11

of the experiment. Pressure signals in the region upstream of the step are skewed to the right, positive values, where significant positive pressure surges are present. The step negative pressure surges prevail from the adverse pressure gradient in the region downstream, and the simulation predicts the same negative surges.

The same analysis was carried out for all EVM models. PDFs for  $k-\omega$  scheme are depicted in Figure 8.16. PDFs obtained for  $k-\omega$  SST and  $k-\varepsilon$  can be found in Appendix D - Figure D.1, Figure D.2. It is apparent from these Figures that in all cases, the universal shape of statistical pressure distribution was reproduced independent of the distance to the step. This clearly indicates no evidence of the stronger positive or negative pressure surges predicted

by these simulations. Despite the promising result of a statistical distribution of pressure fluctuations reproduced by the  $k - \omega$  SST and also the  $k - \omega$  model, no alternating pressure surges are predicted. In the case of  $k - \varepsilon$ , the poor statistical pressure distributions confirm the lack of the dominating pressure peaks in the PSD analyses.

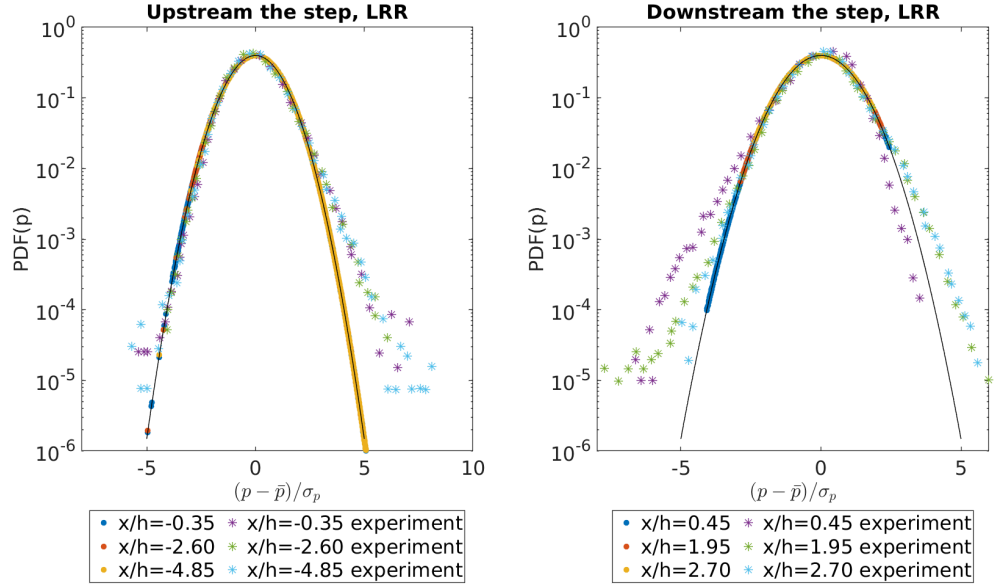


Figure 8.15. PDF of the normalised wall pressure fluctuations, LRR scheme. Different colours correspond to different locations of the step. Circles are the results of simulation and crosses from the experiment. Locations upstream of the step are grouped on the left sub-figure, and locations downstream of the step are grouped on the right sub-figure. The solid line is the Gaussian reference curve.

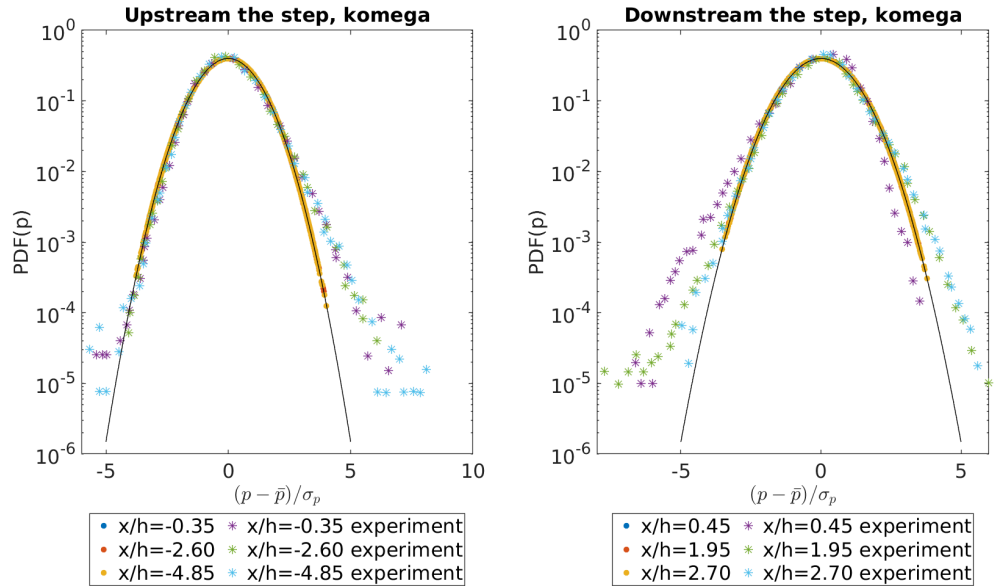


Figure 8.16. PDF of the normalised wall pressure fluctuations,  $k - \omega$  scheme. Indications are the same as in the Figure 8.15.



### 8.3.1 Conclusions

The results of this study indicate that the EVM class of models, even with the third order QUICK discretisation scheme, cannot trigger or sustain induced vibrations. When, however, the stress models (LRR, SSG) are used with bounded TVD discretisation schemes, which over most of the flow domain are second order, they are able to reproduce the large-scale flow instabilities responsible for flow-induced vibrations. It is apparent that the amplitude of pressure fluctuation is strongly underestimated with the EVMs. As shown in Section 4.8, the RSM models address the limitations of the EVMs because they include an exact representation of the Reynolds stress production, the transport processes and generally a more realistic representation of the physical processes that govern the distribution of the turbulent stresses. The LRR predictions show that this model is able to reproduce the large-scale, low-frequency vortices at the leading edge of the forward-facing step. The pressure surges of the same frequencies and amplitude as in the experiment indicate that this model is able to predict the frequency and the amplitude of flow instabilities with good accuracy. The LRR scheme is consequently selected for the two-way FSI analysis that follows.

## 8.4 Two-way FSI Simulations of Cantilever Cylinder

In this section, the knowledge gained in the numerical explorations of the two previous sections is brought together and directed to the simulation of turbulent flow-induced vibrations exerted on a single rod subjected to axial flow. This is the case for which earlier experimental investigations [26] provide validation data. In a preliminary test of the solid deformation part of the solver, the 3-D simulation of a cylindrical rod in a vacuum was performed. The rod is initially subjected to a force which is subsequently removed, allowing the rod to oscillate. This is then followed by the 3-D simulations of the full 2-way flow-induced vibrations induced by the turbulent axial flow.

The test assembly of the corresponding experiment [26] is shown in Figure 8.17. The rod subjected to the axial flow is a  $1m$  long circular stainless steel tube filled with lead shots to approximate the linear density of actual PWR fuel rods. The lead shots are tightly packed inside the tube. The maximum vibration amplitude has reached as large as  $100\mu m$  for the analyzed mass flow rate. The motion of the free end was recorded with a fast-imaging camera, whilst a second camera was used to measure the flow field via PIV. Additionally, the test section had an embedded flow straightener, and the pump location was relatively far from the inlet (2-3m). The geometry of the experimental system was designed to be informative of pressurized-water-cooled reactor flow conditions.

The experiment results indicate that the beam end shape does not influence the cantilever dynamics below a certain critical velocity, and vibrations are only due to the turbulent buffeting from the external flow. These results are similar to those reported by Rinaldi [117].

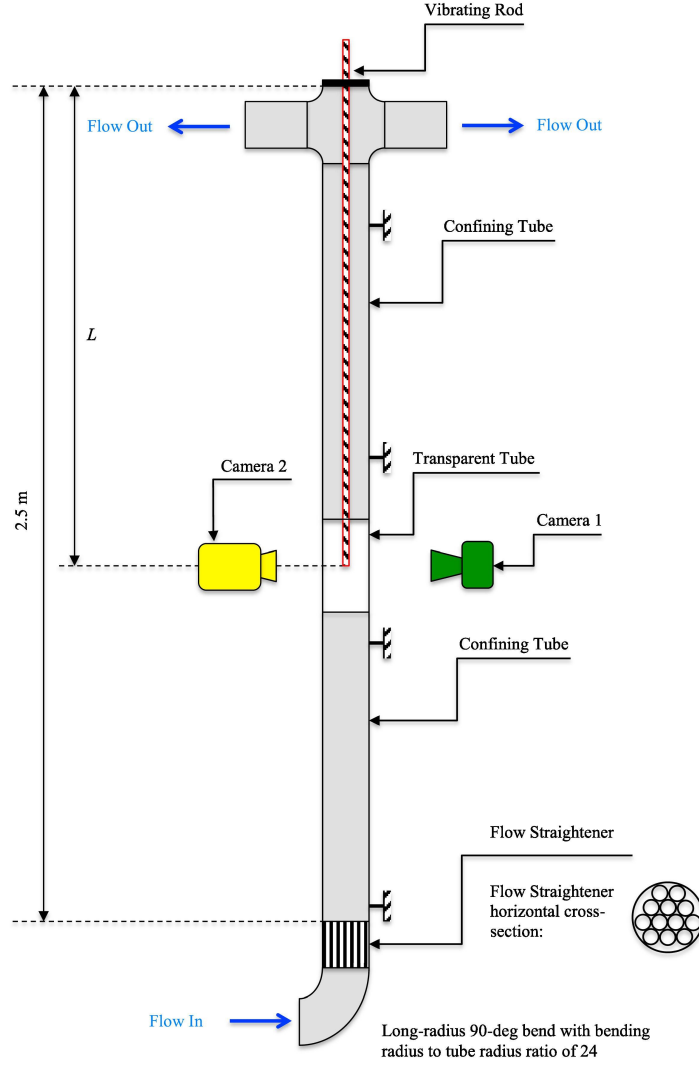


Figure 8.17. Schematic representation of the test rig [26]

## 8.5 Solid Mechanics Part - cantilever beam in vacuum

The clamped-free beam with a circular cross-section was subjected to a uniform peak force  $P(t) = 1N$  for  $t = 10^{-3}$  seconds. The force is then removed, causing the beam to vibrate. The beam is made out of one material, stainless steel, to simplify the simulation. The beam vibrates harmonically at natural frequency  $f_N$  and the associated mode shape  $\widetilde{y}_N(x)$ . For a cantilever beam in a vacuum,  $f_N$  can be predicted with Euler-Bernoulli beam theory as in Equation 8.4:

$$f_N = \frac{c_N^2}{2\pi L^2} \sqrt{\frac{EI}{m_{rod}}} \quad (8.4)$$

Where  $c_N = 1.875$  is the natural frequency parameter for a first mode shape,  $E$  is the elastic modulus,  $I$  is the second moment of area of the beam's cross-section,  $L$  is the length of a beam and  $m_{rod} = \rho A$  is the mass of the beam per unit length.

The case domain and the mesh used in the simulation are depicted in Figure 8.18. The solid properties are summarised in Table 8.4. The material properties have been adapted to match

the natural frequency of a freely vibrating beam in [26]. The mesh consists of  $\sim 170,000$  hexahedral cells. The structural mesh size is adopted to facilitate the interpolation of the displacement increment to the fluid side at the fluid-structure interface. The structural mesh with a reduced number of cells has not been considered at this stage.

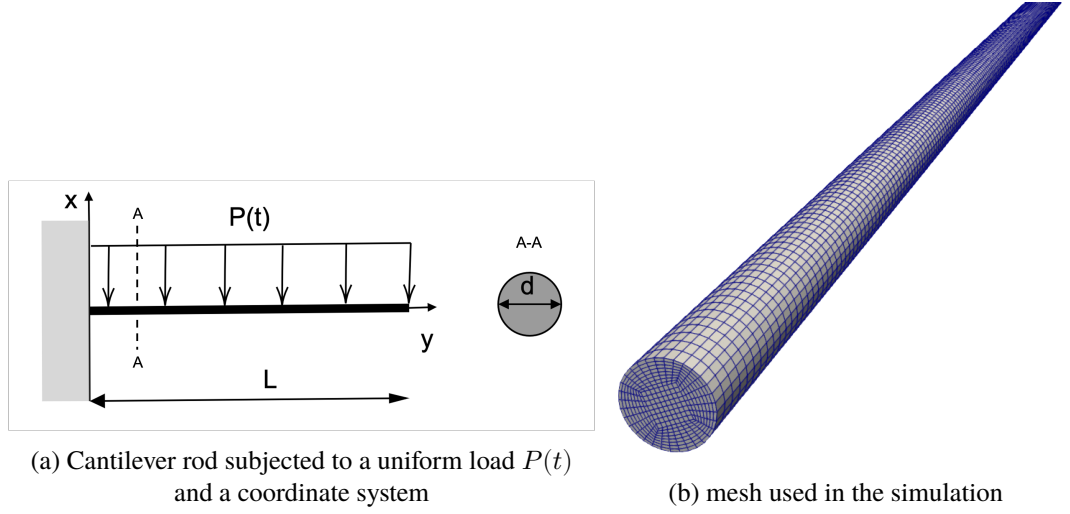


Figure 8.18. Geometry of the domain for a flexible beam in vacuum simulation

Solid properties	
Length, $L$ [m]	1.06
Diameter, $d$ [m]	0.01
Density, $\rho_S$ [ $\frac{kg}{m^3} \times 10^3$ ]	7.49
Young modulus, $E$ [GPa]	76.4
Natural frequency (I mode), $f_N$ [Hz]	3.98
Natural frequency in experiment [26] [Hz]	3.98

Table 8.4. Solid properties used in the flexible beam in vacuum simulation

The time discretisation is performed using the first-order implicit order scheme, which can cause some numerical dissipation when the time step is not small enough [66].

A set of four tests has been carried out to determine the optimum time step and number of iterations per time step to be adopted for the full two-way FSI simulation. In the first three simulations, the number of loop iterations is 1000 and the time step,  $\Delta t$ , has values of  $10^{-5}s$ ,  $2.5 \times 10^{-5}s$  and  $5 \times 10^{-5}s$ , for 'Case 1', 'Case 2' and 'Case 3' respectively. In 'Case 4', the number of iterative loop iterations is reduced to 200, and the value of  $\Delta t$  is kept to  $5 \times 10^{-5}s$ .

As can be seen in Figure 8.19, all schemes predict practically identical behaviour over the first two oscillations. Looking at this Figure, it is apparent that a very small time step of  $1 \times 10^{-5}s$  needs to be adopted to avoid numerical damping. However, increasing the time-step and limiting the number of outer loops by a factor of 5 results in achieving a 25 times faster simulation than in 'Case 1'. The displacement amplitude appeared to be unaffected by numerical diffusion for the first half-period of the oscillation. For the first full period of oscillation, the amplitude is marginally lower (0.01mm) than for the reference case. Considering that the beam subjected to the turbulent flow is under constant excitation, the numerical damping will not affect the amplitude of the FIV. Having the benefit of fast compu-

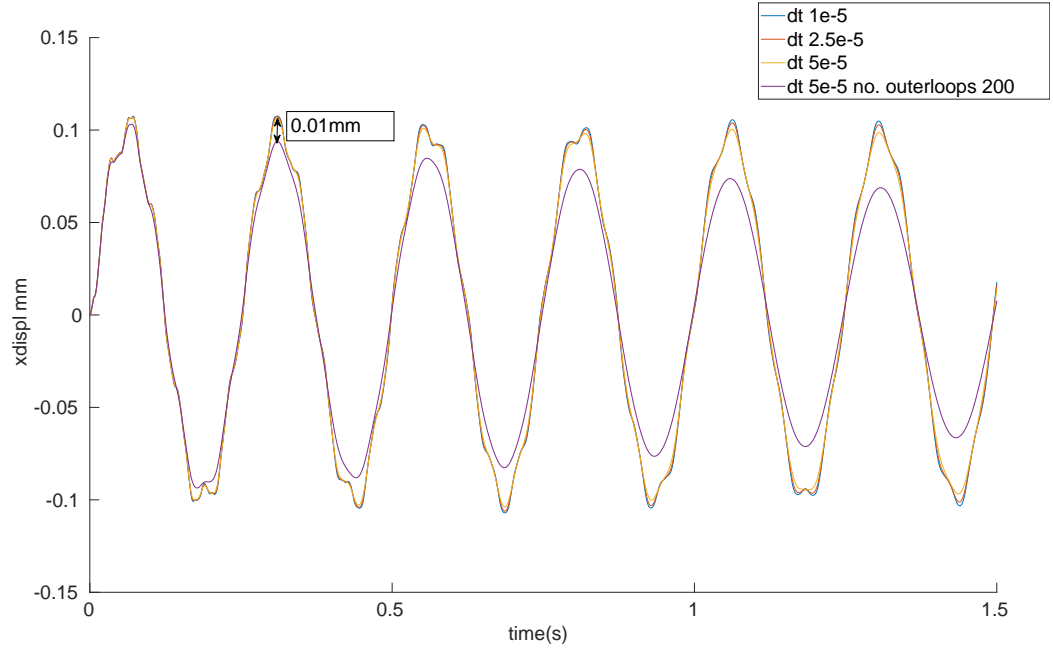


Figure 8.19. Free-end displacement time series for a simulation of a cantilever in vacuum

tation time, Case 4 will be adopted in the next simulation. This conclusion is further confirmed by the frequency comparisons of Table 8.5, in which 'Case 4' predicts the free oscillation frequency to be within 2.3% of the analytical value.

Simulation Case ( $\Delta t$ , no of outer loops)	Frequency [Hz]	Error [%]
Analytical solution	3.98	
Case 1 ( $\Delta t = 1 \times 10^{-5}s$ , 1000)	3.99	0.30%
Case 2 ( $\Delta t = 2.5 \times 10^{-5}s$ , 1000)	4.03	1.30%
Case 3 ( $\Delta t = 5 \times 10^{-5}s$ , 1000)	4.02	1.05%
Case 4 ( $\Delta t = 5 \times 10^{-5}s$ , 200)	4.07	2.31%

Table 8.5. Effect of the time step on the calculated natural frequency

### 8.5.1 Conclusions

The validation case of a slender beam in a vacuum exposed that the convergence of a segregated approach is slow and inefficient. The poor efficiency was noted for bending thin, slender beams in [18]. The deflection of the long slender beam exceeded even  $10^5$  outer iterations, significantly increasing the run-time. The explicitly treated terms in the discretisation of solid equations have a large contribution. Consequently, many outer iterations are required to re-couple the momentum equation. The computational time of this benchmark could be improved by using the mesh on the solid side with a reduced number of cells. Then consequently, the number of cells in the fluid mesh would need to be reduced to avoid having large non-conformality at the FSI interface. However, the fluid mesh has to be fine enough to reproduce the flow unsteadiness to induce the movement of a structure. Another way is to adopt the block-coupled implementation presented in [28, 122]. This method was not considered because it was not implemented in the OpenFOAM while developing this benchmark. Finally, the computational time has been improved by enforcing the limit on the number of outer iterations required to re-couple the momentum equation.

## 8.6 Two-way FSI simulations

The cantilever beam described in Section 8.5.1 is now subjected to axial turbulent flow. The flow is directed from the rod free-end to the clamped-end. Properties of the fluid are summarised in Table 8.6. The inlet velocity  $u_{in}$  in the simulation has been chosen to correspond to the reduced velocity  $u^*$  from the experiment.  $Re_{ann}$  is based on the annulus hydraulic diameter, and  $V_{avg}$  is an average flow velocity in the annulus between the rod and confining tube. The non-dimensional velocity is defined as:

$$u^* = \frac{V_{avg}}{f_0 d} \quad (8.5)$$

Where  $f_0 = 3.6Hz$  is the natural frequency of the cantilever beam in static water calculated with Equation 8.4 by adding the mass of the confined water  $m_{add}$  to the mass of a beam. The mass of the confined water is calculated as [11]:

$$m_{add} = \rho_F \frac{\pi}{4} d^2 \frac{1 + (d/D)^2}{1 - (d/D)^2} \quad (8.6)$$

Fluid properties	Value
Chanel diameter, D [m]	0.021
Chanel length, L [m]	1.12
Hydraulic diameter $d_h$ [m]	0.011
Density, $\rho_F [kgm^{-3}]$	997
Kinematic viscosity, $\nu_F [m^2 s^{-1} (\times 10^{-6})]$	0.893
Inlet velocity, $u_{in} [ms^{-1}]$	1
Annular gap velocity, $V_{avg} [ms^{-1}]$	1.3
Reduced velocity, $u^*$	36
Reynolds, $Re_{ann}$	$16.1 \times 10^3$

Table 8.6. Fluid properties and simulation parameters

The computational domain used in the simulation is depicted in Figure 8.20. The cantilever beam can move, due to elastic deformation, in the x and y directions. The mesh of the fluid domain consists of  $\sim 600,000$  hexahedral cells. A fully developed flow is imposed at the inlet using the same method described in Section 8.3. Constant pressure is imposed at the outlet of the channel. The LRR Reynolds stress model has been selected on the fluid side with the same temporal and convective discretisation practices described in the fluid flow validation Section 8.3.

### 8.6.1 Simulation with the rigid rod

Before proceeding to examine the full FSI simulation, flow over a rigid rod has been computed first to validate the fluid side of the simulation. Figure 8.21 presents the predicted (using the LRR) contours of the instantaneous velocity field at three time steps and also a comparison between predicted and measured (through PIV) time-averaged velocity fields. Velocity has been normalised with  $V_{inf}$  corresponding to the centerline velocity of the approaching flow. The simulation was run for 1 second, after an initial 2 seconds required for

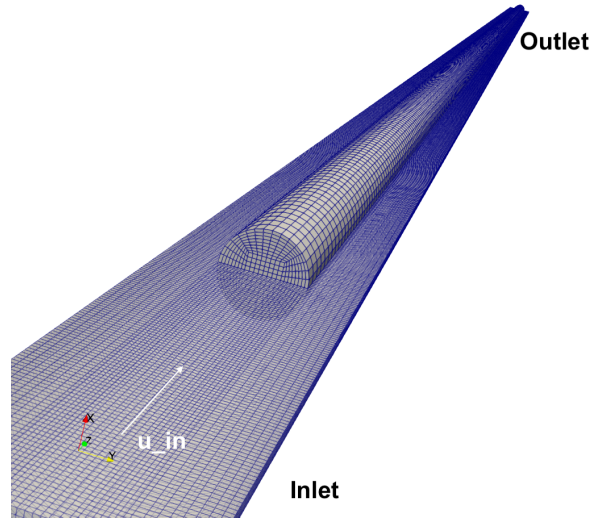


Figure 8.20. Computational domain for a cantilever in turbulent flow simulation

a particle of fluid to traverse the length of the channel. It is visible that the induced flow fluctuations travel along the length of a channel, and the confinement changes the dynamics of the flow. For instance, at location  $\frac{y}{D} = 1.4$  in Figure 8.21a and at location  $\frac{y}{D} = 1.2$  in Figure 8.21c fluctuations appear to be enhanced by the channel walls. The mean velocity, depicted in Figure 8.21d over a period of 1 second, shows two separation regions near the rod tip.

Figure 8.22 includes the quantitative comparison between the calculated and measured averaged axial and radial velocity profiles at three different vertical elevations: upstream of the rod free-end, at the free-end tip and downstream of the rod free-end. In the experiment, the flow field in the region on the left of the rods was not resolved because this part was not illuminated by the laser. Due to the modest lack of symmetry in the flow field upstream of the beam, evident in the measured axial velocity component, the radial velocity field that develops subsequently is not fully symmetric (or, to be more precise, anti-symmetric). The upstream profile comparisons show some asymmetry in the upstream measured velocity, while a symmetric inlet flow is imposed in the simulation. This inevitably leads to further deviations between the predicted and measured velocity profiles further downstream, but overall the simulations produce the same flow development as that presented in the measurements. Interestingly, the instantaneous velocity visualisation Figure 8.21e, did not reveal a flow detachment for the blunt-end. It has been assumed that the fluid was adapting to the movement of vibrating rods. However, the reason could be due to the relatively small resolution of the PIV in the experiment.

### 8.6.2 Simulation with the moving rod

Moving now to consider the cantilever beam from Section 8.5.1 subjected to axial turbulent flow, we arrive to the final benchmark simulation. The fluid mesh has been allowed to move with the linear distance-based method. The Aitken under-relaxation was chosen for the coupling with the relaxation factor set to 0.2 for the first FSI iteration (then it adap-

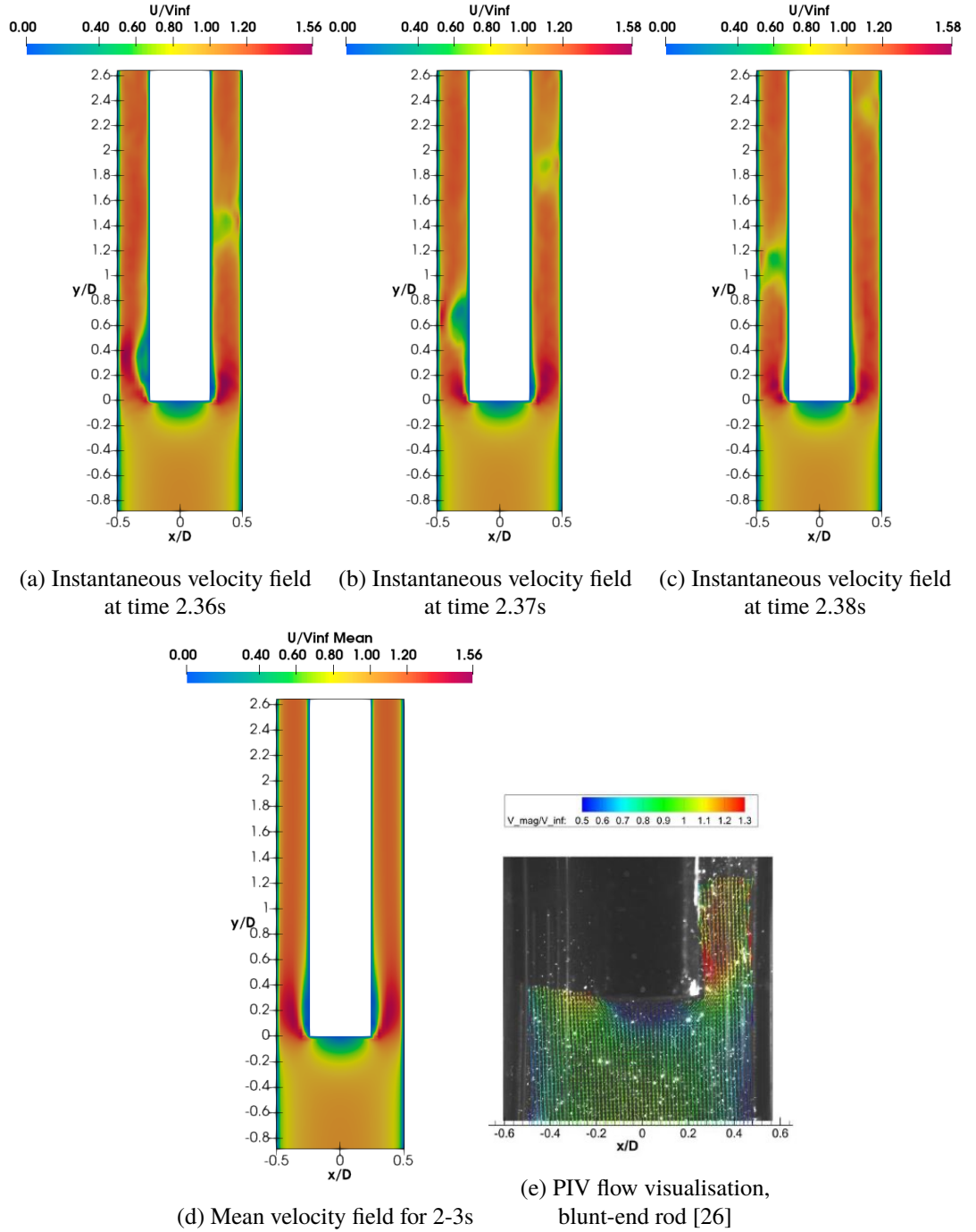


Figure 8.21. Flow fields around the rod tip at low flow velocity, results from the  $u^*=36$  and the experimental results  $u^*=35.7$

tively changes as described in Section 5.3). The fluid-structure residual was set to  $10^{-4}$ . This convergence criterion was selected with trial and error, and it is a minimal value to prevent solid mesh overlapping on a fluid mesh. The coupling starts after the initial 2 seconds. The simulation was decomposed to 36 processors and set to simulate a total period of 10.5 seconds. This requires using the High Performance Computing cluster at the University of Manchester (2x16-core Intel Xeon Gold 6130 CPU @ 2.10GHz Mellanox Infini-Band). The video presenting the instantaneous velocity field and the pressure field with a simultaneous rod movement and the mesh adoption is included in the reference [119]. The equivalent computational time (ECT), defined as computing time for 0.1 s of the simulation on a single core, is 14 days for this case. The result can be compared to the findings of De

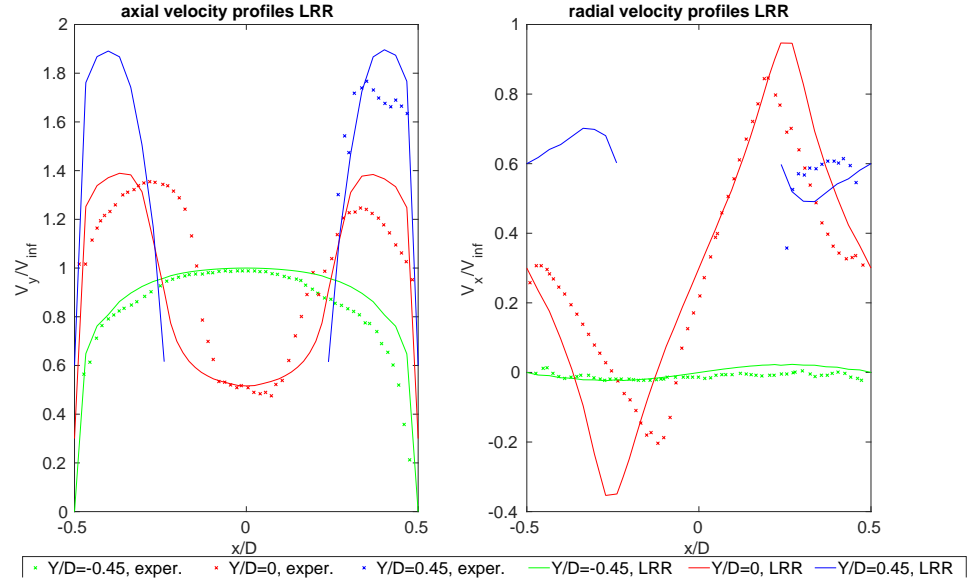


Figure 8.22. Velocity profiles for velocity  $u^*=36$ , vertical elevation locations are provided in the legend

Ridder et al. [34] where Large Eddy Simulations were used to compute the pressure spectrum in an annular channel with nearly the same hydraulic diameter and with nine times shorter channel length. The minimal number of cells for the referred simulation is 8 million, and the ECT is 63 days. If the LES was adopted for the current geometry, it would require about 567 ECT days to calculate solely the rigid simulation, which is 40.5 times more CPU expensive than the current two-way FSI settings.

Further analysis compares the measured and computed (using the LRR model) time-histories of the displacement of the rod free-end, over a period of 5 seconds depicted in Figure 8.23. The x-displacement track for the entire simulation is presented in the same Figure. It can be observed that the computed displacement matches the range of displacements observed in the experiment. The movement of the rod was induced by the flow unsteadiness, and no initial displacement needed to be applied. It can be observed that after the 6 seconds of the simulation, the amplitude becomes damped till 7 seconds. The same intermittent behaviour was observed during the experiment [26], where the maximum displacement of the rod was large enough to noticeably change the geometry of the flow passage. In the simulated case, when the rod reached an excessive amplitude, it was bounced back from the channel walls through fluid coupling. It can thus be suggested that two-way FSI coupling is necessary for modelling of the FIV in the Fuel Assembly. In addition, the fuel rod in the Fuel Assembly component will be subjected to coupling effects induced by neighbouring fuel rods as shown in [90]. Table 8.7 presents comparisons between the experimental and computed (using the LRR) dominant frequency, determined using FFT, and the RMS amplitude. The frequency bandwidth of 0.1Hz is defined with full width at half the maximum of a frequency peak. The reduced root-mean-square amplitude  $A^*$  is defined as:

$$A^* = \frac{A_{rms}}{d} \quad (8.7)$$



These quantitative comparisons of Table 8.7 provide further confirmation to what is demonstrated in Figure 8.23. Considering the numerical and experimental errors, the simulated frequency and the RMS amplitude match the experimental data, validating the present benchmark implementation.

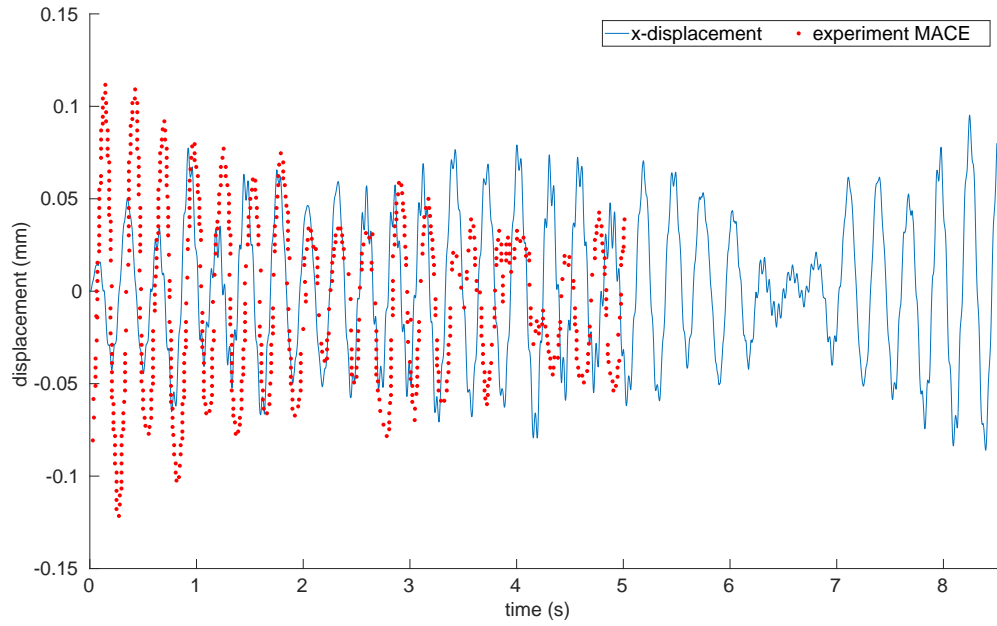


Figure 8.23. Displacement of a free-end vibrating beam in the x direction vs. experimental data

Value	Simulation	Experiment [26]
Frequency	$3.55 \pm 0.05 \text{ Hz}$	$3.6\text{-}3.75 \text{ Hz}$
Amplitude, $A^*$	0.004	0.004-0.006

Table 8.7. Frequency and Amplitude of flow-induced vibration x-plane, LRR scheme

Simple statistical analysis was used to further compare the experimental results with the simulated ones. Figure 8.24 presents the histogram of displacement time series from the experiment compared to the same histogram from the simulation. The histogram data were normalised using probability density function estimate in MATLAB. The normal density function is fitted to the data to further visualise their trend. Overall the distribution of simulated displacement matches well the distribution from the experiment. The distribution of displacements obtained during the experiment shows two distinct peaks, which lie between negative  $40\text{-}70 \mu\text{m}$  and positive  $10\text{-}50 \mu\text{m}$ . The simulation presents more Gaussian-like distribution with dominating peak in the middle of the distribution (at  $0 \mu\text{m}$ ) and 95% of observations lying within  $\pm 80 \mu\text{m}$ . It is almost certain that the simulated amplitude of vibration will not exceed  $122 \mu\text{m}$ . The same statistic extracted from the experiment gives  $143 \pm 10 \mu\text{m}$ , which is from 8 to 21% higher than that of the simulation.

For the sake of completeness, the time series of free-end displacement in the y-direction is depicted in Figure 8.25 and summarised in Table 8.8. The most interesting aspect of this graph is that the displacement is visibly higher than that of the experiment. The comparisons in Table 8.8 show that the frequency of induced vibration is the same as the one in the x-plane, but the reduced RMS amplitude ( $A^*$ ) is at least 17% overestimated with respect to the experiment. Since the experiment provides the result in only one direction, the x-

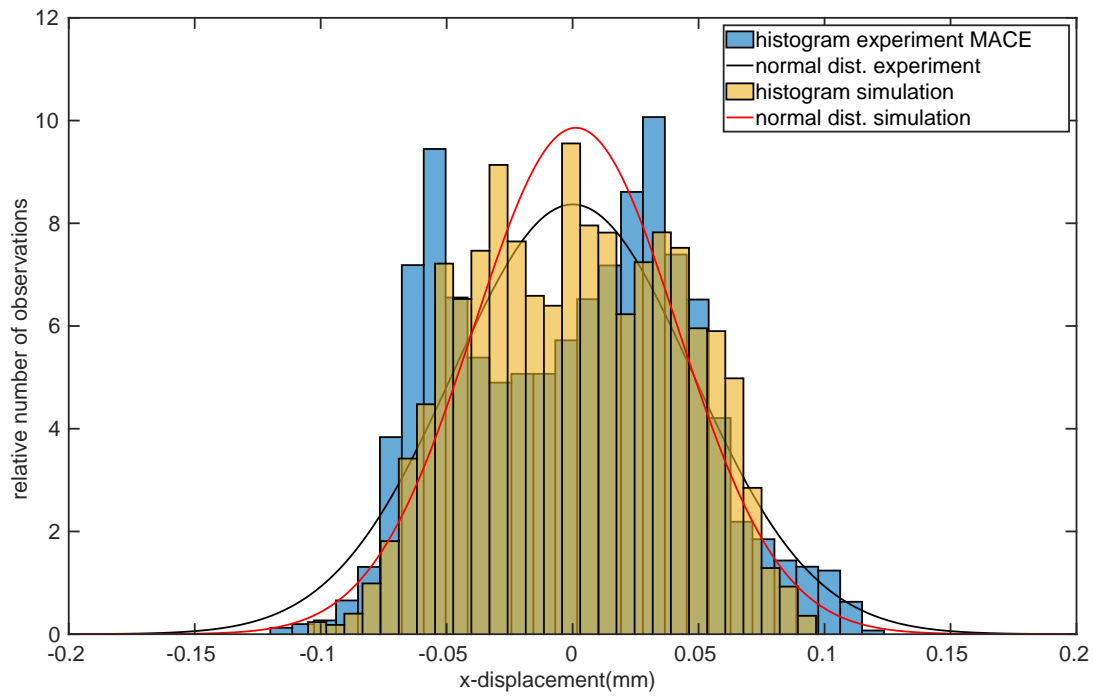


Figure 8.24. Normalized histogram of a number of occurrences observed for a free-end displacement on x-plane. Simulation vs experiment

displacement track series is the actual numerical benchmark. Figure 8.26 provides the summary statistics for free-end displacement in the y-plane time series. The histogram has the same Gaussian-like distribution as the x-displacement but with a much wider spread of the observed displacements, with 95% values recorded in the range between  $\pm 143\mu m$ . Almost certainly, the simulated amplitude of vibration will not exceed  $214\mu m$ , and it is approximately 30% higher than that of the experiment. These findings may be useful in establishing the design criteria for Flow-Induced Vibrations, where maximum achievable amplitude should be considered.

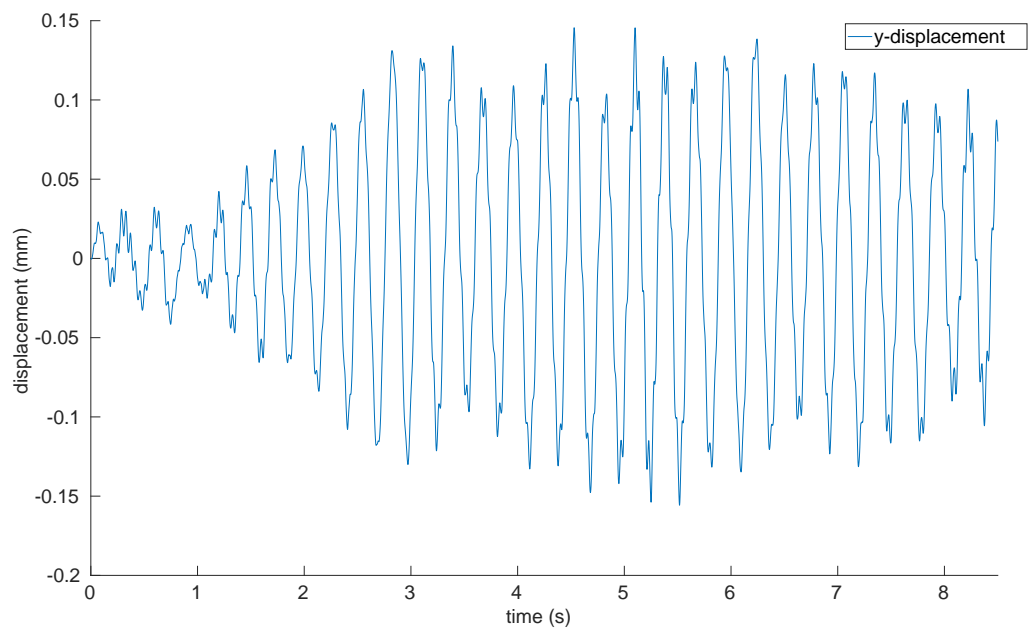


Figure 8.25. Displacement of a free-end vibrating beam in the y direction vs. experimental data

Value	Simulation	Experiment [26]
Frequency	$3.55 \pm 0.05 \text{ Hz}$	3.6-3.75 Hz
Amplitude, $A^*$	0.007	0.004-0.006

Table 8.8. Frequency and Amplitude of flow-induced vibration y-plane, LRR scheme

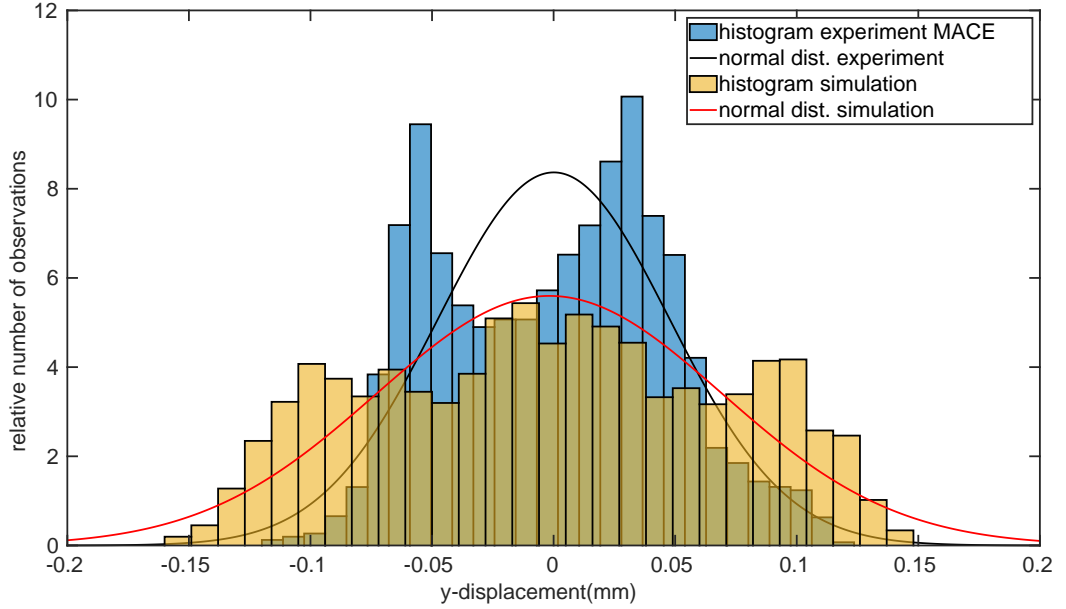


Figure 8.26. Normalized histogram of the number of occurrences observed for a free-end displacement on y-plane simulation vs experiment

By contrast, the corresponding comparisons of Table 8.9 for FSI predictions obtained using the  $k - \omega$  model (with the same computational domain) show that while this EVM is able to predict the correct frequency of oscillations, the amplitude of oscillations predicted by this model is two orders of magnitude lower than that found in the experiment which practically makes it zero. A comparison of the findings with those of other studies reported in Section 8.1 confirms that the EVMs are incapable of reproducing the amplitude of the rod vibrations.

Value	Simulation	Experiment [26]
Frequency	$3.69 \pm 0.4 \text{ Hz}$	3.6-3.75 Hz
Amplitude, $A^*$	$1.89 \times 10^{-5}$	0.004-0.006

Table 8.9. Frequency and Amplitude of flow-induced vibration,  $k - \omega$  scheme

### 8.6.3 Conclusions

This study has presented a valid modelling approach for creating the benchmark simulation of the turbulent flow interaction with the flexible structure. The investigation of the 2D test case with the rigid wall in Section 8.3.1, has shown that the Reynolds Stress Models are better able to reproduce the type of flow unsteadiness which leads to flow-induced vibrations. The final results of the simulations are consequently based mainly on the use

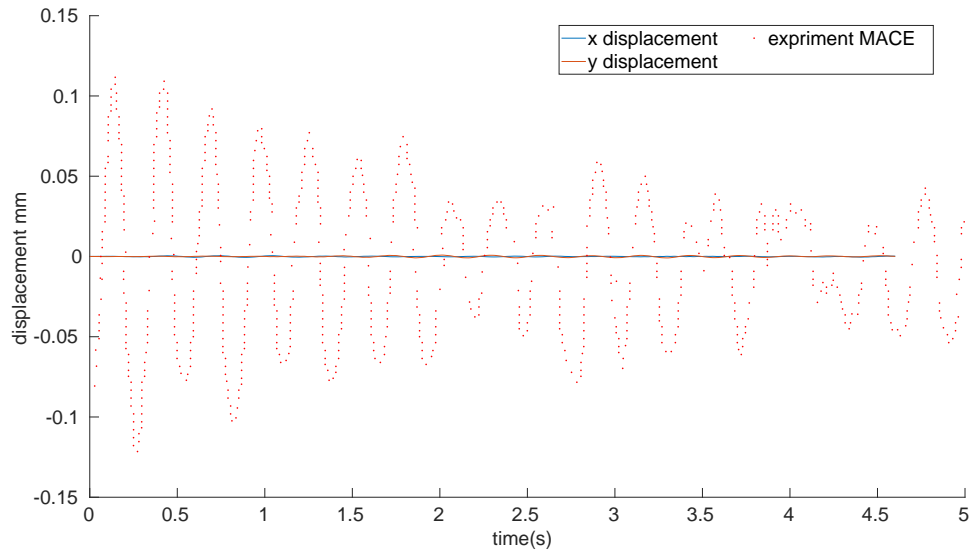


Figure 8.27. Displacement of a free-end vibrating beam vs. experimental data

of the Reynolds Stress Model and show good agreement with the experimental data. The adopted approach allowed to predict the frequency of vibrations and the amplitude of vibrations with good accuracy. The movement of the rod is triggered by the flow itself, and vibrations remain self-sustained without being damped out. The resulting comparisons show that for the first time, to my knowledge, both the frequency and the amplitude of the flow-induced vibrations of this case have been reproduced with such accuracy. Moreover, the achieved CPU time is reasonable for the strongly coupled FSI simulations, and it is about 40 times lower as compared to the LES rigid simulations, making the proposed numerical methodology optimal for industrial applications.

# Chapter 9

## Conclusions and further work

The initial aim of this research was to explore the modelling approaches toward assessing the flow-induced vibrations of cantilever rods subjected to turbulent axial flow at operating conditions relevant to those of fuel rods of pressurised-water-cooled (PWR) nuclear reactors. These are long, slender rods subjected to turbulent axial flow.

The investigation of nuclear component failures has shown that excessive vibration of the nuclear reactor components like heat exchangers and fuel rods can lead to a component failure causing safety hazards and financial loss. As shown in Chapter 1 the grid-to-rod fretting phenomenon occurring in fuel assembly is an ongoing problem in the nuclear industry. The survey has also identified two main sources of FIV in the design of the fuel assembly: turbulent buffeting and movement-induced vibration mechanism.

The findings from the literature review have raised an important question about the understanding of the relation of excitation forces to vibration exerted on the fuel rods. The experimental test rig for investigating this flow-induced vibration phenomenon was first installed at the University of Manchester in 2018 under the financial support of the EDF [26]. The obtained data are particularly suited for FSI simulation benchmarking. The availability of these data was an inspiration for the current study.

In this project, fluid-structure interaction (FSI) benchmark simulation of the cylindrical cantilever beam subjected to the axial turbulent flow has been performed. The primary aim has been to assemble all the modelling elements needed for a cost-effective and thus URANS-based modelling strategy, employing high-Reynolds-number turbulence models.

In order to meet this objective, the modelling strategy needs to combine three main elements:

- URANS high-Reynolds-number models that are able to reproduce the strength of the large-scale flow oscillations which cause the flow-induced vibrations.
- A two-way FSI numerical solver, in which the pressure and viscous forces generated by the flow over the rod surface are used as input to the solution of the elastic deformation equations, which provide the rod deformation, and the rod deformation is then used to modify the geometry of the flow domain.

- A mesh regeneration method that is able to adjust the mesh of the fluid domain after each rod deformation.

First, by considering the oscillations generated by laminar flow over an elastic plate attached downstream of a cylinder, it has been demonstrated that:

- (a) An ALE approach in which the fluid dynamics equations and the solid elastic deformation equations are discretised and solved within the same finite-volume solver, with an Eulerian and Lagrangian formulation for the fluid and solid equations, respectively, provides a suitable two-way FSI solver.
- (b) A Laplacian smoothing of the displacement of the fluid mesh is adequate for the relatively small deformations encountered in this application.

Then by considering turbulent flow over the forward-facing step, it has been established that high-Reynolds-number Reynolds Stress Models, such as the LRR [81] and SSG [125], with high order convection discretisation schemes are able to reproduce the large-scale flow instabilities with satisfactory accuracy.

As a result, by combining all the above elements, which include the use of the LRR [81] Reynolds Stress URANS model, it becomes possible to reproduce the oscillatory behaviour of a cantilever beam exposed to axial flow with considerable accuracy. On the other hand, the effective-viscosity models severely underestimate the strength of flow unsteadiness and, consequently, the amplitude of the rod oscillations. This is the first successful simulation of flow-induced oscillations of cantilever rods relevant to PWR applications based on the use of URANS.

The most important limitation of the proposed benchmark is that the numerical damping on the structural model in a vacuum was accepted to reach a reasonable computation time. As explained in Section 8.5.1, the analysed beam will be subjected to constant excitation from the turbulent flow field and, as shown in later sections, did not lead to underestimation of root-mean-square amplitude of induced vibrations. The system of equations of the linear elastic model is solved in a segregated manner which has noticeably slow performance in finite volume structural solvers.

## 9.1 Recommendations for further research work

The literature review exposed that the amplitude of vibration depends strongly on the shape of the beam-end and the direction of flow approaching the beam. Further research could use this benchmark with the flow directed from the clamped-end towards the free-end and compare the amplitude of vibration. This investigation will have practical importance for the nuclear reactor in-core instrumentation [12, 110].

Another important practical implication is the assessment of the amplitude of vibration with the beam with the streamlined end. The solid, fluid and FSI settings developed in this

project will be valid for the approach, but extensive work is required to develop the solid mesh and the matching fluid mesh.

A future study investigating the fluid-coupling effects would be very interesting. The study of FIV of two bare rods subjected to axial flow with a small pitch-to-diameter ratio could be a valuable case study for investigations of the causes of excessive vibrations in the fuel assembly. This is a strongly coupled FSI problem, thus the simulation could be established starting from the settings developed for this benchmark.

Another possible area of future research would be to perform FSI simulations of a large fuel assembly. While this simulation remains computationally expensive and challenging, it was shown in this study, that the CPU achieved for this benchmark is very reasonable. A strongly coupled FSI simulation of the entire fuel assembly will help analyse the component's underlying FIV mechanism and possibly lead to necessary design changes in the nuclear PWR reactors.

# References

1. *ANSYS FLUENT 12.0 Theory Guide - 18.3.1 Spatial Discretization* <https://www.afs.enea.it/project/neptunius/docs/fluent/html/th/node366.htm>.
2. Apsley, D. D. & Leschziner, M. A. Advanced turbulence modelling of separated flow in a diffuser. *Flow, Turbulence and Combustion* **63**, 81–112. ISSN: 13866184 (2000).
3. Basile, D., Fauré, J. & Ohlmer, E. Experimental study on the vibrations of various fuel rod models in parallel flow. *Nuclear Engineering and Design* **7**, 517–534 (1968).
4. Basting, S., Quaini, A., Canic, S. & Glowinski, R. On the implementation and benchmarking of an extended ALE method for FSI problems. *Fluid-Structure Interaction*, 3–40 (Nov. 2017).
5. Beaudoin, M. & Jasak, H. Development of a Generalized Grid Interface for Turbomachinery simulations with OpenFOAM. *Talk*, 1–11. papers3://publication/uuid/81CCD00D-DF48-4595-B591-C577955CEA06 (2008).
6. Belytschko, T. *Nonlinear finite elements for continua and structures* Second edition. eng (ed Belytschko, T.) ISBN: 9781118700051 (Wiley, Chichester, England, 2014).
7. Benra, F.-K., Dohmen, H. J., Pei, J., Schuster, S. & Wan, B. A Comparison of One-Way and Two-Way Coupling Methods for Numerical Analysis of Fluid-Structure Interactions. *Journal of Applied Mathematics* **2011**, 16 (2011).
8. Blau, P. J. A multi-stage wear model for grid-to-rod fretting of nuclear fuel rods. *Wear* **313**, 89–96. ISSN: 0043-1648 (May 2014).
9. Blevins, R. D. Flow-induced vibration in nuclear reactors: A review. *Progress in Nuclear Energy* **4**, 25–49. ISSN: 01491970 (1979).
10. Blevins, R. D. *Formulas for natural frequency and mode shape* (Van Nostrand Reinhold Company, 1979).
11. Blevins, R. D. *Flow Induced Vibration - 2nd Ed* (Krieger Publishing Company, Malabar, Florida, 2001).
12. Borsoi, L. Flow-Induced Vibration of Nuclear Components : Future R & D Perspective Derived from the French Experience. *Transactions SMiRT* **16**, 1–12 (2001).
13. Bos, F. M. *Numerical simulations of flapping foil and wing aerodynamics* PhD thesis (TU Delft, 2010), 1–236. ISBN: 9789090251738.



14. Camussi, R., Guj, G. & Ragni, A. Wall pressure fluctuations induced by turbulent boundary layers over surface discontinuities. *JOURNAL OF SOUND AND VIBRATION* **294**, 177–204. [www.elsevier.com/locate/jsvi](http://www.elsevier.com/locate/jsvi) (2006).
15. Camussi, R., Felli, M., Pereira, F., Aloisio, G. & Di Marco, A. Statistical properties of wall pressure fluctuations over a forward-facing step. *Physics of Fluids* **20**. ISSN: 10706631 (2008).
16. Cardiff, P. *et al.* An open-source finite volume toolbox for solid mechanics and fluid-solid interaction simulations 2018. <https://arxiv.org/abs/1808.10736>.
17. Cardiff, P. *et al.* An open-source finite volume toolbox for solid mechanics and fluid-solid interaction simulations. <http://arxiv.org/abs/1808.10736> (2018).
18. Cardiff, P. *Development of the Finite Volume Method for Hip Joint Stress Analysis* PhD thesis (2012). <http://hdl.handle.net/10197/7919>.
19. Cardiff, P. Development of the Finite Volume Method for Hip Joint Stress Analysis by Philip Cardiff. *Thesis M*, 241 (2012).
20. Carlucci, L. N. Damping and Hydrodynamic Mass of a Cylinder in Simulated Two-Phase Flow. *Journal of Mechanical Design* **102**, 597. ISSN: 10500472. <http://mechanicaldesign.asmedigitalcollection.asme.org/article.aspx?articleid=1451249> (July 1980).
21. Causin, P., Gerbeau, J. F. & Nobile, F. Added-mass effect in the design of partitioned algorithms for fluid-structure problems. *Computer Methods in Applied Mechanics and Engineering* **194**, 4506–4527. ISSN: 00457825 (Oct. 2005).
22. Chen, S. S. *Flow-Induced Vibration of Circular Cylindrical Structures* tech. rep. (Argonne, Illinois, 1985).
23. Chen, S. S. & Wambsganss, M. W. Parallel-flow-induced vibration of fuel rods. *Nuclear Engineering and Design* **18**, 253–278 (1971).
24. Chen, S. S., Wambsganss, M. W. & Jendrzejczyk, J. A. Added Mass and Damping of a Vibrating Rod in Confined Viscous Fluids. *Journal of Applied Mechanics* **43**, 325. ISSN: 00218936. <http://appliedmechanics.asmedigitalcollection.asme.org/article.aspx?articleid=1402949> (June 1976).
25. Christon, M. A. *et al.* Large-eddy simulation, fuel rod vibration and grid-to-rod fretting in pressurized water reactors. *Journal of Computational Physics* **322**, 142–161. ISSN: 10902716. <http://dx.doi.org/10.1016/j.jcp.2016.06.042> (2016).

26. Cioncolini, A., Silva-Leon, J., Cooper, D., Quinn, M. K. & Iacovides, H. Axial-flow-induced vibration experiments on cantilevered rods for nuclear reactor applications. *Nuclear Engineering and Design* **338**, 102–118. ISSN: 00295493. <https://doi.org/10.1016/j.nucengdes.2018.08.010> (2018).
27. Clément, S. A. & Bardet, P. M. Surrogates for Single-Phase Conjugate Heat Transfer Validation Experiments at Light Water Reactor Prototypical Conditions. <https://doi.org/10.1080/00295450.2017.1327254> (Aug. 2017).
28. Clifford, I. *Block-Coupled Simulations Using OpenFOAM in 6th OpenFOAM Workshop* (2011). [http://www.personal.psu.edu/dab143/OFW6/Training/clifford\\_slides.pdf](http://www.personal.psu.edu/dab143/OFW6/Training/clifford_slides.pdf).
29. Conner, M. E., Baglietto, E. & Elmahdi, A. M. CFD methodology and validation for single-phase flow in PWR fuel assemblies. *Nuclear Engineering and Design* **240**, 2088–2095 (2010).
30. Daly, B. J. & Harlow, F. H. Transport Equations in Turbulence. *The Physics of Fluids* **13**, 2634. ISSN: 0031-9171. <https://aip.scitation.org/doi/abs/10.1063/1.1692845> (Aug. 2003).
31. Davidson, L. Fluid mechanics, turbulent flow and turbulence modeling (2015).
32. De Ridder, J., De Moerloose, L., Van Tichelen, K., Vierendeels, J. & Degroote, J. *Simulation of flow-induced vibrations in tube bundles using URANS* 293–310. ISBN: 9780081019801. <http://dx.doi.org/10.1016/B978-0-08-101980-1.00019-3> (Elsevier Ltd., 2018).
33. De Ridder, J., Degroote, J. & Doaré, O. Fluid-Elastic Instabilities of Clamped-Clamped Aligned and Inclined Cylinders in Turbulent Axial Flow, V004T04A001 (2015).
34. De Ridder, J., Degroote, J., Tichelen, K. V., Schuurmans, P. & Vierendeels, J. Predicting turbulence-induced vibration in axial annular flow by means of large-eddy simulations. *Journal of Fluids and Structures* **61**, 115–131. ISSN: 0889-9746 (Feb. 2016).
35. De Ridder, J., Degroote, J., Van Tichelen, K., Schuurmans, P. & Vierendeels, J. Modal characteristics of a flexible cylinder in turbulent axial flow from numerical simulations. *Journal of Fluids and Structures* **43**, 110–123. ISSN: 10958622. <http://dx.doi.org/10.1016/j.jfluidstructs.2013.09.001> (2013).
36. De Santis, D., Kottapalli, S. & Shams, A. Numerical simulations of rod assembly vibration induced by turbulent axial flows. *Nuclear Engineering and Design* **335**, 94–105. ISSN: 0029-5493 (Aug. 2018).

37. De Santis, D. & Shams, A. Numerical study of flow-induced vibration of fuel rods. *Nuclear Engineering and Design* **361**, ISSN: 00295493. <https://doi.org/10.1016/j.nucengdes.2020.110547> (May 2020).
38. De Santis, D. & Shams, A. Numerical modeling of flow induced vibration of nuclear fuel rods. *Nuclear Engineering and Design* **320**, 44–56. ISSN: 00295493. <https://linkinghub.elsevier.com/retrieve/pii/S002954931730242X> (Aug. 2017).
39. De Santis, D. & Shams, A. An advanced numerical framework for the simulation of flow induced vibration for nuclear applications. *Annals of Nuclear Energy* **130**, 218–231. ISSN: 18732100. <https://doi.org/10.1016/j.anucene.2019.02.049> (Aug. 2019).
40. Degroote, J., Bathe, K.-J. & Vierendeels, J. Performance of a new partitioned procedure versus a monolithic procedure in fluid-structure interaction. *Computers and Structures* **87**, 793–801. <http://www.FloHeaCom.UGent.be/> (2009).
41. Delafontaine, S. & Ricciardi, G. Fluctuating pressure calculation induced by axial flow trough mixing grid. *Nuclear Engineering and Design* **242**, 233–246. ISSN: 00295493 (2012).
42. Demirdžić, I. A fourth-order finite volume method for structural analysis. *Applied Mathematical Modelling* **40**, 3104–3114. ISSN: 0307904X. <http://dx.doi.org/10.1016/j.apm.2015.09.098> (Feb. 2016).
43. Demirdžić, I. & Muzaferija, S. Finite volume method for stress analysis in complex domains. *International Journal for Numerical Methods in Engineering* **37**, 3751–3766. ISSN: 10970207 (1994).
44. Den Hartog, J. *Mechanical vibrations* ISBN: 9780486131856 (Dover Publications, New York, 1985).
45. Divaret, L., Cadot, O., Moussou, P. & Doaré, O. Normal forces exerted upon a long cylinder oscillating in an axial flow. *Journal of Fluid Mechanics* **752**, 649–669. ISSN: 14697645 (2014).
46. Eisfeld, B., Rumsey, C. & Togiti, V. Verification and Validation of a Second-Moment-Closure Model. <https://doi.org/10.2514/1.J054718> **54**, 1524–1541. ISSN: 00011452. <https://arc.aiaa.org/doi/abs/10.2514/1.J054718> (Mar. 2016).
47. Fang, J. & Bolotnov, I. A. Bubble tracking analysis of PWR two-phase flow simulations based on the level set method. *Nuclear Engineering and Design* **323**, 68–77. ISSN: 00295493. <http://dx.doi.org/10.1016/j.nucengdes.2017.07.034> (2017).

48. *Finite Volume Differencing Schemes* Mar. 2022. [https://ses.library.usyd.edu.au/bitstream/handle/2123/376/adt-NU20010730.12021503\\_chapter\\_2.pdf?sequence=3&isAllowed=y](https://ses.library.usyd.edu.au/bitstream/handle/2123/376/adt-NU20010730.12021503_chapter_2.pdf?sequence=3&isAllowed=y).
49. *Finite Volume Method: A Crash introduction* May 2022. [http://www.wolfdynamics.com/wiki/fvm\\_crash\\_intro.pdf](http://www.wolfdynamics.com/wiki/fvm_crash_intro.pdf).
50. Frei, S., Holm, B., Richter, T., Wick, T. & Eds, H. Y. *Fluid-Structure Interaction: Modeling, Adaptive Discretizations and Solvers* 251–252. ISBN: 9783110495270 (2019).
51. *FSI tests - Featflow* June 2022. [http://www.mathematik.tu-dortmund.de/~featflow/en/benchmarks/cfdbenchmarking/fsi\\_benchmark/fsi\\_tests/fsi\\_fsi\\_tests.html](http://www.mathematik.tu-dortmund.de/~featflow/en/benchmarks/cfdbenchmarking/fsi_benchmark/fsi_tests/fsi_fsi_tests.html).
52. Gibson, M. M. & Launder, B. E. Ground effects on pressure fluctuations in the atmospheric boundary layer. *Journal of Fluid Mechanics* **86**, 491–511. ISSN: 1469-7645. <https://www.cambridge.org/core/journals/journal-of-fluid-mechanics/article/ground-effects-on-pressure-fluctuations-in-the-atmospheric-boundary-layer/D5FFE2AB889A67F31D2EDDD08D2EB006> (1978).
53. Govers, K. *et al.* BLG-1142 Characterization of Belgian Spent Fuel Assemblies (2019).
54. Greenshields, C. J. *OpenFOAM UserGuide* **July** (2019).
55. Hackett, R. M. *Hyperelasticity Primer* 2nd edition. eng. ISBN: 9783319732015 (Springer International Publishing, Cham, 2018).
56. Hewitt, S., Margetts, L., Revell, A., Pankaj, P. & Levrero-Florencio, F. OpenFPCI: A parallel fluid–structure interaction framework. *Computer Physics Communications*. ISSN: 0010-4655. <https://www.sciencedirect.com/science/article/pii/S0010465519301742?via%3Dihub#!> (June 2019).
57. Higuchi, H., van Langen, P., Sawada, H. & Tinney, C. Axial flow over a blunt circular cylinder with and without shear layer reattachment. *Journal of Fluids and Structures* **22**, 949–959. ISSN: 08899746. <https://linkinghub.elsevier.com/retrieve/pii/S0889974606000600> (Aug. 2006).
58. Higuchi, H., Sawada, H. & Kato, H. Sting-free measurements on a magnetically supported right circular cylinder aligned with the free stream. *Journal of Fluid Mechanics* **596**, 49–72. ISSN: 00221120 (2008).
59. Hoffmann, K. A. & Chiang, S. T. *Computational fluid dynamics*. 4. ed., 1. print. ISBN: 9780962373169 (Engineering Education System, Wichita Kan., 2000).
60. Hofstede, E. T. *Numerical Study of Fluid Structure Interaction in Nuclear Reactor Applications* PhD thesis (2015).

61. Holzapfel, G. A. *Nonlinear solid mechanics : a continuum approach for engineering eng.* ISBN: 047182304X (Wiley, Chichester, 2000).
62. Iacovides, H. *Lecture 2 Near wall turbulence* tech. rep. June (The University of Manchester, 2019).
63. IAEA. *Review of Fuel Failures in Water Cooled Reactors* ISBN: 92-0-102298-0. <https://www.iaea.org/publications/8259/review-of-fuel-failures-in-water-cooled-reactors> (INTERNATIONAL ATOMIC ENERGY AGENCY, Vienna, 2010).
64. International Atomic Energy Agency. Structural behaviour of fuel assemblies for water cooled reactors, 324 (2005).
65. Irons, B. M. & Tuck, R. C. A version of the Aitken accelerator for computer iteration. *International Journal for Numerical Methods in Engineering* **1**, 275–277. ISSN: 0029-5981. <http://doi.wiley.com/10.1002/nme.1620010306> (July 1969).
66. Jasak, H. & Weller, H. G. Application of the finite volume method and unstructured meshes to linear elasticity. *International Journal for Numerical Methods in Engineering* **48**, 267–287. ISSN: 00295981 (2000).
67. Jasak, H. & Tukovic, Z. Dynamic mesh handling in OpenFOAM applied to fluid-structure interaction simulations. *European Conference on Computational Fluid Dynamics*, 1–19 (2010).
68. Jasak, H. & Tuković, Ž. *Automatic Mesh Motion for the Unstructured Finite Volume Method* tech. rep. (2004).
69. Jasak, H. & Tuković, Ž. Automatic mesh motion for the unstructured Finite Volume Method. *Transactions of Famena* **30**, 1–20. ISSN: 13331124 (2006).
70. Jean-Marc, V., Pascal, D., Charles, H. & Benoit, L. *STRONG COUPLING ALGORITHM TO SOLVE FLUID-STRUCTURE-INTERACTION PROBLEMS WITH A STAGGERED APPROACH* tech. rep. ().
71. *k-omega Shear Stress Transport (SST)* Sept. 2022. <https://www.openfoam.com/documentation/guides/latest/doc/guide-turbulence-ras-k-omega-sst.html>.
72. Kadlec, J. & Ohlmer, E. On the reproducibility of the parallel-flow induced vibration of fuel pins. *Nuclear engineering and Design* **17**, 355–360 (1971).
73. Kaneko, S., Nakamura, T., Fumio, I. & Minoru, K. *Flow-Induced Vibrations Classifications and Lessons from Practical Experiences* (Elsevier Science, 2008).

74. Kim, K.-T. & Jang, Y.-K. *Flow-induced grid-to-rod fretting wear in PWR fuel assemblies* tech. rep. (International Atomic Energy Agency (IAEA), 2005), 247–255. [http://inis.iaea.org/search/search.aspx?orig\\_q=RN:37018073](http://inis.iaea.org/search/search.aspx?orig_q=RN:37018073).
75. KIM, K.-T. & SUH, J.-M. M. Impact of Nuclear Fuel Assembly Design on Grid-to-Rod Fretting Wear. *Journal of Nuclear Science and Technology* **46**, 149–157. ISSN: 0022-3131 (Feb. 2009).
76. Kollmannsberger, S. *et al.* Fixed-grid fluid-structure interaction in two dimensions based on a partitioned Lattice Boltzmann and p-FEM approach. *International Journal for Numerical Methods in Engineering* **79**, 817–845. ISSN: 00295981 (Aug. 2009).
77. Kottapalli, S., Shams, A., Zuijlen, A. H. & Pourquie, M. J. Numerical investigation of an advanced U-RANS based pressure fluctuation model to simulate non-linear vibrations of nuclear fuel rods due to turbulent parallel-flow. *Annals of Nuclear Energy* **128**, 115–126. ISSN: 18732100. <https://doi.org/10.1016/j.anucene.2019.01.001> (2019).
78. Küttler, U. & Wall, W. A. Fixed-point fluid-structure interaction solvers with dynamic relaxation. **43**, 61–72 (2008).
79. Lamarsh, J. R. *Introduction to nuclear engineering* 3rd ed. eng (ed Baratta, A. J.) ISBN: 0201824981 (Prentice Hall, Upper Saddle River, N.J, 2001).
80. Lane, A. D. *The measurement and prediction of vibration in CANDU-PHW fuel and channel assemblies* in *International Conference on Vibration in Nuclear Plant* (Keswick, 1978).
81. Launder, B. E., Reece, G. J. & Rodi, W. Progress in the development of a Reynolds-stress turbulence closure. *Journal of Fluid Mechanics* **68**, 537–566. ISSN: 14697645. <https://www.cambridge.org/core/journals/journal-of-fluid-mechanics/article/abs/progress-in-the-development-of-a-reynoldsstress-turbulence-closure/796DDAC14EF54A84A36100565D3420D5> (1975).
82. Lighthill, M. J. Note on the swimming of slender fish. <https://doi.org/10.1017/S0022112060001110> (1960).
83. Liu, Y. & Hinrichsen, O. CFD modeling of bubbling fluidized beds using OpenFOAM®: Model validation and comparison of TVD differencing schemes. *Computers and Chemical Engineering* **69**, 75–88. ISSN: 00981354. <http://dx.doi.org/10.1016/j.compchemeng.2014.07.002> (Oct. 2014).
84. Löhner, R. & Yang, C. Improved ALE mesh velocities for moving bodies. *Communications in Numerical Methods in Engineering* **12**, 599–608. ISSN: 10698299 (Oct. 1996).

85. Löhner, R. *Applied computational fluid dynamics techniques : an introduction based on finite element methods* 2nd ed. eng. ISBN: 9780470519073 (John Wiley, Chichester, 2008).
86. Meher, K. K. & Rao, A. R. Optimization of the number of spacers in a nuclear fuel bundle with respect to flow-induced vibration. *Nuclear Engineering and Design* **236**, 2348–2355 (2006).
87. Moukalled, F. *The Finite Volume Method in Computational Fluid Dynamics : An Advanced Introduction with OpenFOAM® and Matlab* 1st ed. 2015. eng (eds Mangani, L. & Darwish, M.) ISBN: 9783319168746 (Springer International Publishing, Cham, 2016).
88. Moukalled, F., Mangani, L. & Darwish, M. The Finite Volume Method in Computational Fluid Dynamics. *Fluid Mechanics and Its Applications* **113**. <http://link.springer.com/10.1007/978-3-319-16874-6> (2016).
89. Naudascher, E. & Rockwell, D. *Practical Experiences with Flow-Induced Vibrations* (Springer-Verlag, Berlin, 1980).
90. Naudascher, E. & Rockwell, D. *Flow-Induced Vibrations: An Engineering Guide* (Dover Publications, Inc., 2012).
91. *Neo-Hookean solid* June 2022. [https://en.wikipedia.org/wiki/Neo-Hookean\\_solid](https://en.wikipedia.org/wiki/Neo-Hookean_solid).
92. Nobile, F. Numerical approximation of fluid-structure interaction problems with application to haemodynamics. <https://infoscience.epfl.ch/record/32934> (2001).
93. Ohlmer, E., Rosso, S. & Schwemmler, R. Investigation of an analytical model for parallel flow induced vibrations. *Nuclear Engineering and Design* **22**, 272–289 (1972).
94. Okita, Y. & Iacovides, H. Comparisons of High-Reynolds-Number EVM and DSM Models in the Prediction of Heat and Fluid Flow of Turbine Blade Cooling Passages. *Journal of Turbomachinery* **125**, 585–597. ISSN: 0889-504X. <https://asmedigitalcollection.asme.org/turbomachinery/article/125/3/585/459356/Comparisons-of-High-Reynolds-Number-EVM-and-DSM> (July 2003).
95. *OpenFOAM: Manual Pages: boundaryFoam(1)* Apr. 2022. <https://www.openfoam.com/documentation/guides/latest/man/boundaryFoam.html>.
96. *OpenFOAM: User Guide: Limited linear divergence scheme* Apr. 2022. <https://www.openfoam.com/documentation/guides/latest/doc/guide-schemes-divergence-limited-linear.html>.

97. Paidoussis, M. P. Dynamics of cylindrical structures subjected to axial flow. *Journal of Sound and Vibration* **29**, 365–385. ISSN: 0022-460X. <https://www.sciencedirect.com/science/article/pii/S0022460X73802913> (Aug. 1973).
98. Paidoussis, M. P. in *Practical Experiences with Flow-Induced Vibrations* 1–82 (Springer-Verlag, Berlin, 1980).
99. Paidoussis, M. P. Real-life experiences with flow-induced vibration. *Journal of Fluids and Structures* **22**, 741–755 (2006).
100. Paidoussis, M. P. Cylinders in Axial Flow I. *Fluid-Structure Interactions*, 143–302 (Jan. 2016).
101. Paidoussis, M. P. Cylinders in Axial Flow II. *Fluid-Structure Interactions*, 303–367 (Jan. 2016).
102. Paidoussis, M. P., Grinevich, E., Adamovic, D. & Semler, C. Linear and nonlinear dynamics of cantilevered cylinders in axial flow. part 1: physical dynamics. *Journal of Fluids and Structures* **16**, 691–713. ISSN: 0889-9746. <https://www.sciencedirect.com/science/article/pii/S0889974602904470> (Aug. 2002).
103. Paidoussis, M. P. *The amplitude of fluid-induced vibration of cylinders in axial flow* tech. rep. March (Canada, 1965). <https://www.osti.gov/biblio/4657622%20https://www.osti.gov/servlets/purl/4657622>.
104. Paidoussis, M. P. Dynamics of flexible slender cylinders in axial flow Part 2. Experiments. *Journal of Fluid Mechanics* **26**, 737–751. ISSN: 14697645. <https://doi.org/10.1017/S0022112066001496> (1966).
105. Paidoussis, M. P. A review of flow-induced vibrations in reactors and reactor components. *Nuclear Engineering and Design* **74**, 31–60. ISSN: 0029-5493 (Jan. 1983).
106. Paidoussis, M. P. *Fluid-structure interactions : slender structures and axial flow. Volume 2* 2nd edition. eng. ISBN: 9780123973344 (Academic Press, Kidlington, Oxford, U.K. ; 2016).
107. Patankar, S. V. ( V. *Numerical heat transfer and fluid flow* eng. ISBN: 0891165223 (Hemisphere, New York, 1980).
108. Peng, S.-H., Davidson, L. & Holmberg, S. *The Two-Equation Turbulence  $k-\omega$  Model Applied to Recirculating Ventilation Flows* PhD thesis (Chalmers University of Technology, Goteborg, Feb. 1996).
109. Peric, M. *A finite volume method for the three-dimensional fluid flow in complex ducts* PhD thesis (Imperial College, London, 1985).



110. Pettigrew, M. J. *Flow-induced vibration of nuclear power station components* tech. rep. (Chalk River, Ontario, 1977). [https://inis.iaea.org/search/search.aspx?orig\\_q=RN:9360949](https://inis.iaea.org/search/search.aspx?orig_q=RN:9360949).
111. Pettigrew, M. J. *et al.* Fretting-Wear Damage due to Vibration in Nuclear and Process Equipment. *American Society of Mechanical Engineers, Pressure Vessels and Piping Division (Publication) PVP* **4**. ISSN: 0277027X (Oct. 2017).
112. *Pressurized water reactor* Aug. 2022. [https://en.wikipedia.org/wiki/Pressurized\\_water\\_reactor](https://en.wikipedia.org/wiki/Pressurized_water_reactor).
113. Rhie, C. M. & Chow, W. L. Numerical study of the turbulent flow past an airfoil with trailing edge separation. *AIAA Journal* **21**, 1525–1532. ISSN: 00011452 (1983).
114. Ricciardi, G., Bellizzi, S., Collard, B. & Cochelin, B. Modelling Pressurized Water Reactor cores in terms of porous media. *Journal of Fluids and Structures* **25**, 112–133. ISSN: 08899746 (2009).
115. Rinaldi, S. *Experiments on the dynamics of cantilevered pipes subjected to internal and/or external axial flow* PhD thesis (2009). ISBN: 9780494669198.
116. Rinaldi, S. & Paidoussis, M. P. Dynamics of a Free-Clamped Cylinder in Confined Axial Flow, 381–388 (2012).
117. Rinaldi, S. & Paidoussis, M. P. Theory and experiments on the dynamics of a free-clamped cylinder in confined axial air-flow. *Journal of Fluids and Structures* **28**, 167–179. ISSN: 08899746 (2012).
118. Rodriguez, S. *Applied Computational Fluid Dynamics and Turbulence Modeling* (Springer International Publishing, 2019).
119. Salachna, J. Flow-Induced Vibration Video. [https://figshare.com/articles/media/Flow-Induced\\_Vibration\\_Video\\_avi/19673931](https://figshare.com/articles/media/Flow-Induced_Vibration_Video_avi/19673931) (2022).
120. Salachna, J. Turbulent flow over the forward-facing step. [https://figshare.com/articles/media/Turbulent\\_flow\\_over\\_the\\_forward-facing\\_step\\_Reynolds\\_stress\\_transport\\_models\\_/19738108](https://figshare.com/articles/media/Turbulent_flow_over_the_forward-facing_step_Reynolds_stress_transport_models_/19738108) (2022).
121. Schäfer, M., Heck, M. & Yigit, S. An implicit partitioned method for the numerical simulation of fluid-structure interaction. *Lecture Notes in Computational Science and Engineering* **53**, 171–194. ISSN: 14397358 (2006).
122. Shayegh, A. *Block-coupled Finite Volume algorithms: A solids4Foam tutorial* in *Proceedings of CFD with OpenSource Software* (2020). <http://dx.doi.org/10.17196/OSCFD#YEAR2020>.

123. Shin, M. K., Lee, H. A., Lee, J. J., Song, K. N. & Park, G. J. Optimization of a nuclear fuel spacer grid spring using homology constraints. *Nuclear Engineering and Design* **238**, 2624–2634. ISSN: 0029-5493 (Oct. 2008).
124. Souli, M. & Benson, D. J. *Arbitrary Lagrangian- Eulerian and Fluid – Structure Interaction* ISBN: 9781848211315 (2010).
125. Speziale, C. G., Sarkar, S. & Gatski, T. B. Modelling the pressure-strain correlation of turbulence: an invariant dynamical systems approach. *Journal of Fluid Mechanics* **227**, 245–272. ISSN: 1469-7645. <https://www.cambridge.org/core/journals/journal-of-fluid-mechanics/article/modelling-the-pressurestrain-correlation-of-turbulence-an-invariant-dynamical-systems-approach/3F54EAE2F2998E34ED7CC44D7048B73E> (1991).
126. Taylor, G. I. Analysis of the swimming of long and narrow animals. *Proceedings of the Royal Society of London. Series A. Mathematical and Physical Sciences* **214**, 158–183. ISSN: 2053-9169. <http://www.royalsocietypublishing.org/doi/10.1098/rspa.1952.0159> (Aug. 1952).
127. Ter Hofstede, E., Kottapalli, S. & Shams, A. Numerical prediction of flow induced vibrations in nuclear reactor applications. <http://dx.doi.org/10.1016/j.nucengdes.2017.04.026> (2017).
128. Ter Hofstede, E., Kottapalli, S. & Shams, A. Numerical prediction of flow induced vibrations in nuclear reactor applications. *Nuclear Engineering and Design* **319**, 81–90. ISSN: 00295493 (Aug. 2017).
129. Tuković, Ž. & Jasak, H. *FVM for Fluid-Structure Interaction with Large Structural Displacements* Aug. 2022. [http://www.tfd.chalmers.se/~hani/kurser/OS\\_CFD\\_2009/FSIslides.pdf](http://www.tfd.chalmers.se/~hani/kurser/OS_CFD_2009/FSIslides.pdf).
130. Tuković, Ž., Jasak, H., Karač, A., Cardiff, P. & Ivanković, A. Openfoam finite volume solver for fluid-solid interaction. *Transactions of Famena* **42**, 1–31. ISSN: 18491391 (2018).
131. Tuković, Ž., Jasak, H., Karač, A., Cardiff, P. & Ivanković, A. Openfoam finite volume solver for fluid-solid interaction. *Transactions of Famena* **42**, 1–31. ISSN: 18491391 (Oct. 2018).
132. Turek, S. & Hron, J. Proposal for numerical benchmarking of fluid-structure interaction between an elastic object and laminar incompressible flow. *Lecture Notes in Computational Science and Engineering* **53**, 371–385. ISSN: 14397358 (2006).
133. Ugural, A. C., Fenster, S. K. & Saul Ph. D, K. F. *Advanced Mechanics of Materials and Applied Elasticity* ISBN: 9780137079209 (Pearson Education, 2005).

134. Van Brutzel, L., Dingreville, R. & Bartel, T. J. Chapter 2. Nuclear fuel deformation phenomena. *NEA/NSC/R(2015)* (2015).
135. Versteeg, H. K. ( K. & Malalasekera, W. ( *An introduction to computational fluid dynamics : the finite volume method* 2nd ed. ISBN: 0131274988 (Prentice Hall, Harlow, 2007).
136. Wambsganss, M. W. & Chen, S. S. *Tentative design guide for calculating the vibration response of flexible cylindrical elements in axial flow* tech. rep. (Argonne, Illinois, 1971).
137. Wang, M. *et al.* CFD simulation on the flow characteristics in the PWR lower plenum with different internal structures. *Nuclear Engineering and Design* **364**. ISSN: 00295493. <https://doi.org/10.1016/j.nucengdes.2020.110705> (Aug. 2020).
138. *What is y+ (yplus)? - Using SimScale / Fluid Flow / CFD - SimScale CAE Forum* Feb. 2022. <https://www.simscale.com/forum/t/what-is-y-yplus/82394>.
139. White, F. M. *Fluid mechanics* 862. ISBN: 9780073529349. <https://www.studocu.com/en/document/lebanese-international-university/fluid-mechanics/book-solutions/fluid-mechanics-frank-m-white-7th-edition/1256777/view> (McGraw Hill, 2011).
140. Yates, M. *Finite-Volume Method To Fluid-Structure Interaction Analysis* PhD thesis (The University of Manchester, 2011).
141. Zhang, J. *et al.* CFD investigation of the cold wall effect on CHF in a 5 x 5 rod bundle for PWRs. *Nuclear Engineering and Design* **387**, 111589. ISSN: 00295493. <https://doi.org/10.1016/j.nucengdes.2021.111589> (Feb. 2022).

# Appendix A

## Discretization of the Upwind Scheme

### A.1 Discretization

The discretization equation reads as:

$$a_P = a_W \phi_W + a_E \phi_E \quad (\text{A.1})$$

where,

$$a_E = D_e + \llbracket -F_e, 0 \rrbracket \quad (\text{A.2a})$$

$$a_W = D_w + \llbracket F_w, 0 \rrbracket \quad (\text{A.2b})$$

$$a_P = D_e + \llbracket F_e, 0 \rrbracket + D_w + \llbracket -F_w, 0 \rrbracket = a_E + a_W + (F_e - F_w) \quad (\text{A.2c})$$

This is presented compactly using the form of notation that covers both flow directions, the operator  $\llbracket \cdot \rrbracket$  is introduced to return the argument with the largest value [107]. The mass fluxes at the east and west faces will be:

$$F_e \phi_e = \phi_P \llbracket F_e, 0 \rrbracket - \phi_E \llbracket -F_e, 0 \rrbracket \quad (\text{A.3a})$$

$$F_w \phi_w = \phi_P \llbracket F_w, 0 \rrbracket - \phi_W \llbracket -F_w, 0 \rrbracket \quad (\text{A.3b})$$

In practice the last term in the equation A.2c should be zero to satisfy the continuity equation 6.6.

# Appendix B

## Discretization of the SOU Scheme

### B.1 Discretization

Using the SOU profile, Figure 6.2, the discretized equation is obtained as:

$$a_P\phi_P + a_E\phi_E + a_W\phi_W + a_{EE}\phi_{EE} + a_{WW}\phi_{WW} = 0 \quad (\text{B.1})$$

where,

$$a_E = -D_e - \frac{3}{2}[-F_e, 0] - \frac{1}{2}[F_w, 0] \quad (\text{B.2a})$$

$$a_{EE} = \frac{1}{2}[-F_e, 0] \quad (\text{B.2b})$$

$$a_W = -D_w - \frac{3}{2}[-F_w, 0] - \frac{1}{2}[F_e, 0] \quad (\text{B.2c})$$

$$a_{WW} = \frac{1}{2}[-F_w, 0] \quad (\text{B.2d})$$

$$a_P = a_E + a_W\phi_W + a_{EE} + a_{WW} + (F_e - F_w) \quad (\text{B.2e})$$

# Appendix C

## Discretization of the QUICK Scheme

### C.1 Discretization

The discretized equation is found to be:

$$a_P\phi_P + a_E\phi_E + a_W\phi_W + a_{EE}\phi_{EE} + a_{WW}\phi_{WW} = 0 \quad (\text{C.1})$$

where,

$$a_E = -D_e - \frac{3}{4}[-F_e, 0] + \frac{3}{8}[F_e, 0] - \frac{1}{8}[F_w, 0] \quad (\text{C.2a})$$

$$a_{EE} = \frac{1}{8}[-F_e, 0] \quad (\text{C.2b})$$

$$a_W = -D_w - \frac{3}{4}[-F_w, 0] + \frac{3}{8}[F_w, 0] - \frac{1}{8}[F_e, 0] \quad (\text{C.2c})$$

$$a_{WW} = \frac{1}{8}[-F_w, 0] \quad (\text{C.2d})$$

$$a_P = a_E + a_W\phi_W + a_{EE} + a_{WW} + (F_e - F_w) \quad (\text{C.2e})$$

# Appendix D

## Probability Density Function

### D.1 Probability Density Function of $k-\omega$ SST and $k-\varepsilon$ model

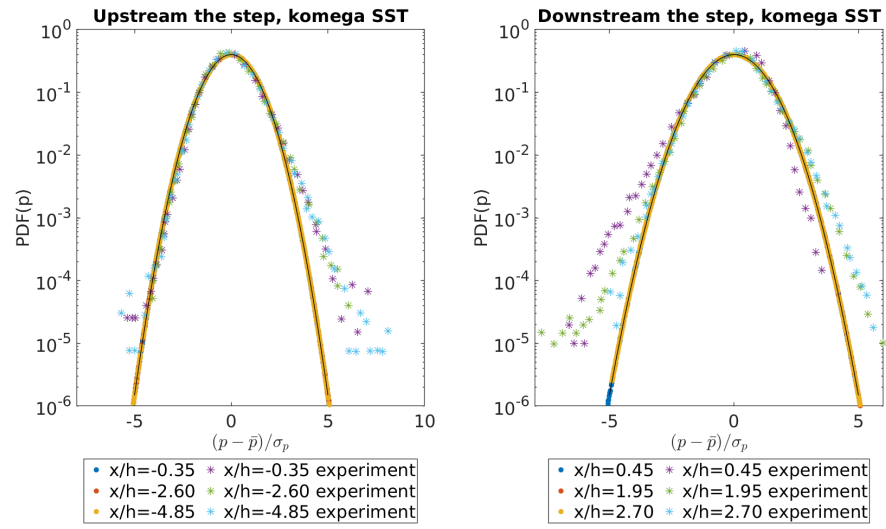


Figure D.1. PDF of the normalized wall pressure fluctuations,  $k-\omega$  SST scheme. Indications are the same as in the Figure 8.15.

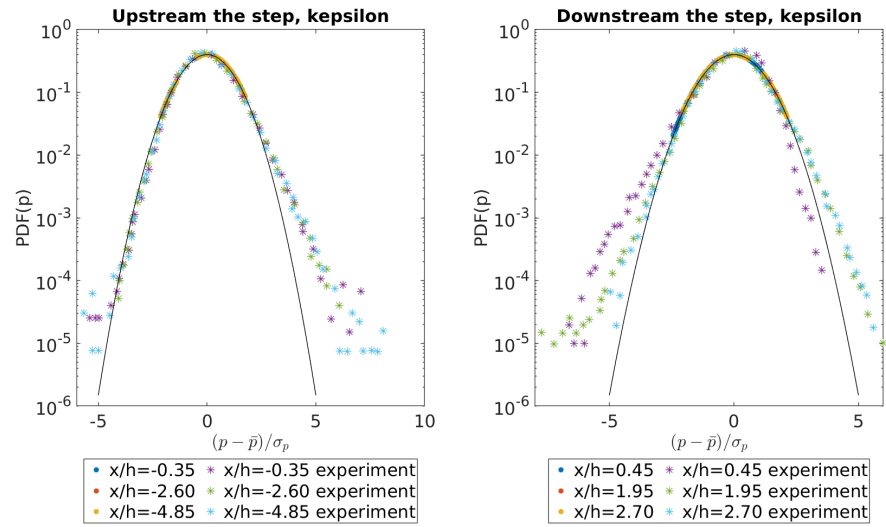


Figure D.2. PDF of the normalized wall pressure fluctuations,  $k-\varepsilon$  scheme. Indications are the same as in the Figure 8.15.

# Appendix E

## List of Publications

### Journal publications:

- **Salachna, J.**, Cioncolini, A. & Iacovides, H. Benchmark Simulation of the Flow-Induced Vibrations for Nuclear Applications. *SSRN Electronic Journal*. <https://ssrn.com/abstract=4102497> (May 2022), Status: Article accepted for publication in *Annals of Nuclear Energy* (Aug 2022)

### International conferences & seminars:

- **Salachna, J.**, Cioncolini, A. & Iacovides, H. Numerical prediction of Axial-Flow-Induced Vibrations in nuclear fuel rod. *12<sup>th</sup> International Conference on Flow-Induced Vibration*, 5-8 Jul 2022, Paris-Saclay, France
- **Salachna, J.**, Cioncolini, A. & Iacovides, H. Benchmark Simulation of the Flow-Induced Vibrations for Nuclear Applications. *17<sup>th</sup> OpenFOAM Workshop*, 11-14 Jul 2022, Cambridge, United Kingdom
- **Salachna, J.** Benchmark Simulation of the Flow-Induced Vibrations for Nuclear Applications. *MACE Aerospace and Thermofluids Seminar*, 23 Feb 2022, University of Manchester, United Kingdom
- **Salachna, J.** Flow-induced vibration in nuclear fuel rods. *MACE Aerospace and Thermofluids Seminar*, 25 Mar 2021, University of Manchester, United Kingdom

### Repositories with simulation settings:

- **Salachna, J.** Laminar FSI Analysis: Validation of the FSI methodology. figshare. Software. <https://doi.org/10.6084/m9.figshare.21191203.v1> (2022)
- **Salachna, J.** Rigid body: Analysis of the turbulence models. figshare. Software. <https://doi.org/10.6084/m9.figshare.21222110.v2> (2022)
- **Salachna, J.** Cantilever beam in vacuum. figshare. Software. <https://doi.org/10.6084/m9.figshare.21225344.v1> (2022)
- **Salachna, J.** Two-way FSI simulations. figshare. Software. <https://doi.org/10.6084/m9.figshare.21235506.v1> (2022)